NORTHWESTERN UNIVERSITY

A Study of Charmed Particle Production in Hadronic Collisions

A DISSERTATION

SUBMITTED TO THE GRADUATE SCHOOL
IN PARTIAL FULFILLMENT OF THE REQUIREMENTS

for the degree

DOCTOR OF PHILOSOPHY

Field of Physics

By

Lucien Marcus Cremaldi

EVANSTON, ILLINOIS

June 1983

ABSTRACT

A Study of Charmed Particle Production in Hadronic Collisions

Lucien Marcus Cremaldi

We have searched for events in 200 GeV/c pion-Beryllium collisions, at Fermi National Accelerator Laboratory, which contain a muon and electron of opposite sign. Such events cannot come from the decay of any known particle, and are attributed to the semileptonic decays of a pair of charmed mesons. A moderate acceptance muon trigger arm was implemented to key on the semileptonic decay of one of the charmed pair and the coincident electron was identified in a lead-liquid argon electromagnetic shower calorimeter. A total of 351±105 events were observed. Assuming the signal derives from charmed meson pairs, and using a central production model for their creation, we estimate the total charmed production cross section for pions incident on Beryllium at $\sqrt{s}=19.4$ GeV to be 14±4 μb/nucleon.

ACKNOWLEDGMENTS

This doctoral thesis was made possible by the efforts of many people. I would like to thank all involved.

Special gratitude goes out to my thesis advisor, Jerome Rosen, and Dave Buchholz, for guiding me through the ordeal to the end. I thank Bob Schluter, and Don Miller for their involvement in my career. Many other people at Northwestern University deserve credit; Joe Hahn in the machine shop, who built so much of the equipment, Bob Tilden in our electronics shop, and Jean Shedd in the front office, who promptly took care of my graduate student business while I was away from the university.

I thank all my collaborators from Carnegie-Mellon University, University of Notre Dame, Rutgers University, Fermilab, and Peoples Republic of China. Ron Lipton, Randy Ruchti, Jim Russ, Dick Edelstein, Loretta Dauwe, Art Kreymer, Mao Huishun, and Dave Johnson deserve much credit for their numerous contributions to this experimental effort.

Next I owe deepest gratitude to my friends and contemporaries, who made the experiment work until completion; Willis Sakumoto, Steve Sontz, Steve Delchamps, Chris Winter, Mike McQuade, George Ginther, Lenny Spiegel, and Rick Pemper. Each must know the credit due to him is enormous.

My heart goes out to Elaine, Anna, and Joseph who encouraged and supported me through the days of hard work. They know best the ways of a scientist.

Finally I dedicate this thesis to my parents, who never once discouraged me from satisfying my curiosities, and patiently waited so long for the completion of my college days. Thank you Mom and Dad.

TABLE OF CONTENTS

Chapter page

1. Introduction 1
   - A. Introduction
   - B. Charmed Particles and the Weak Interaction
   - C. Hadronic Charm Production
   - D. Prompt Muon Trigger
2. Experimental Apparatus 31
   - A. Beam
   - B. Trigger
   - C. Muon Trigger Arm
   - D. Forward Spectrometer Arm
   - E. Data Aquisition
3. Data Analysis 61
   - A. Muon Trigger Analysis
   - B. Forward Spectrometer
   - C. Electromagnetic Shower and Electron Identification
   - D. Forward Muon Identification
   - E. Muon-Lepton Charge Correlations

4. Results 103

A. Results of the Dimuon Analysis

B. Results of the Muon-Electron Analysis

C. Discussion of Errors

D. Conclusions

References 116

Appendix 1 120

Tables 124

Figures 149

LIST OF TABLES

	page
Table 1.	124
Table 2.	125
Table 3.	126
Table 4.	127
Table 5.	129
Table 6.	130
Table 7.	131
Table 8.	132
Table 9.	133
Table 10.	134
Table 11.	135
Table 12.	136
Table 13.	137
Table 14.	138
Table 15.	140

Table 16. 141
Table 17. 142
Table 18. 143
Table 19. 144
Table 20. 145
Table 21. 146
Table 22. 147
Table 23. 148

LIST OF ILLUSTRATIONS

	page
Figure 1.	149
Figure 2.	150
Figure 3.	151
Figure 4.	152
Figure 5.	153
Figure 6.	154
Figure 7.	155
Figure 8.	156
Figure 9.	157
Figure 10.	158
Figure 11.	159
Figure 12.	160
Figure 13.	161
Figure 14.	162
Figure 15.	163
Figure 16.	164
Figure 17.	165
Figure 18.	166
Figure 19.	167
Figure 20.	168

Figure 21. 169

Figure 22. 170

Figure 24. 172

Figure 25. 173

Figure 26. 174

Figure 27. 175

Figure 28. 176

Figure 29. 177

Figure 30. 178

Figure 31. 179

Figure 32. 180

Figure 33. 181

Figure 34. 183

Figure 35. 184

Figure 36. 185

Figure 37. 186

Figure 38. 187

Figure 39. 188

Figure 40. 189

CHAPTER 1

Introduction

A. Introduction

Since the initial observation of the J/ψ [1,2] at BNL and SPEAR in November 1974, a considerable effort has been expended in searching for charmed particles. This surge was initially motivated by a desire to establish their existence, but after the observation of naked charm states in electron-positron annihilations [3] ,neutrino interactions [4,5] and photoproduction experiments [6], a major emphasis has been placed upon the study of charmed particle production in hadronic interactions.

Hadronic interactions have provided a lucrative theatre in which to to study new particle states in the past, mainly due to the variety of particles produced with typically large cross sections. Recent charmed particle searches in hadronic beams have seemed to refute this line of reasoning. Due to small hadronic production cross sections, relatively small branching ratios for each charmed particle decay mode, and complicated event topologies; questions about the nature of charmed particle production in hadronic interactions are left unanswered to a large degree.

The understanding of hadronic charm production is important for a number of reasons. (1) The charmed quark is the first generation of heavy quark. Expectations are high that perturbative QCD calculations will be valid and able to explain production mechanisms and cross sections. The verification of this premise will have great bearing on the theories of hadronic interactions. (2) All charmed particle states produced in electron-positron annihilations and predicted by SU(4) symmetry should be observable in hadronic interactions; do any surprises await? (3) Charmed particle decays are expected to provide a background for for heavy particle searches involving a lepton trigger. An understanding of the character of charm production is needed in order to reliably evaluate this background. (4) Finally, with the foreknowledge that hadronic charmed production cross sections are tens of microbarns, finding a reliable way of keying on these particles in an overwhelming low mass background of conventional particle states is paramount to the success of future particle searches in hadronic beams.

Experiment 515 was performed at Fermi National Accelerator Laboratory during the 1980-81 running periods. We observed hadronic interactions of pions incident on a beryllium target at an incident pion momentum of 200 GeV/c. The experiment was designed to study the hadro-production of charmed particles, both in absolute rates and kinematic distributions. The apparatus consisted of a double arm spectrometer; a dedicated trigger arm of moderate acceptance, and a large acceptance, open geometry forward spectrometer arm for reconstructing multi-hadron states. The plan and elevation views of the spectrometer are shown in Figure 1.

The reaction under study is shown below:

$$\pi^- + \mathrm{Be} \dashrightarrow \bar{C}_1 + C_2 + X$$

$$\dashrightarrow \mu^+, e^+, K\pi, \ldots.$$

$$\dashrightarrow \mu^-$$

C_1 and C_2 are a pair of charmed particles, associatively produced, and X represents any accompanying particle state. Charmed particles are produced hadronically at a partial rate of approximately one per one thousand interactions. In order to enhance the fraction of recorded events containing charm with respect to normal interaction levels, a "prompt muon trigger" was implemented. In the scheme, data was only logged for events in which a interaction in the target occurred in coincidence with a muon being detected in a trigger telescope defining the muon trigger arm; thus the name "prompt muon trigger". Keying on charm particle decays in this manner exploits the associated production of charmed particles and their relatively large partial decay rates into a state which includes a muon (depicted above). Upon triggering the apparatus on the semileptonic decay of charmed particle C_1, the associated charmed state, C_2, is reconstructed in the forward spectrometer arm.

The associated charmed state, C_2, is expected to be populated by semi-leptonic decays of the charmed particle, producing muons and electrons; and nontrivial non-leptonic decays into systems of kaons and pions. Electrons or muons emerging from semileptonic decays of charmed particles, and detected in the forward spectrometer arm, will have an opposite sign charge correlation with the triggering muon. This allows a direct measurement of the charmed particle production rate by observing events in which an electron is detected in coincidence with a triggering muon of opposite sign. The charmed particle production cross section can then be inferred with a knowledge of the semileptonic branching ratios. In addition the production rate for opposite sign muon production can be measured. Although the rate is dominated by sources of electromagnetically produced dimuons, it can provide a useful control sample; comparing the results with previous measurements.

The analysis contained in this thesis involves a search for the above mentioned dilepton correlations. In the following sections of the first chapter the existing theory of charmed particles is reviewed and more details about the background to the trigger and detector response is presented.

B. Charmed Particles and the Weak Interaction

The charm concept was originally introduced [7,8], suggesting an aesthetic lepton-hadron parallelism between the strong and weak interactions. It attained a real operational significance in 1970 when Glashow, Iliopoulos, and Maiani [9] showed its usefulness in alleviating the problems with strangeness-changing neutral currents. The following is an overview of how the charmed quark incorporated itself in a natural way into a unification of quarks and leptons and will lead to a first order description of charmed particle states production, and decay mechanisms.

Cabibbo Theory and the GIM Mechanism

In Cabibbo theory [10] the hadronic weak interaction is shared between strangeness-conserving and strangeness-nonconserving transitions. It was observed that the hadronic strangeness-conserving weak decay rates (neutron beta decay) were slightly weaker than purely leptonic decays (muon beta decay), and that strangeness-changing hadronic weak interactions (lambda beta decay) were weaker still. Experimental evidence also pointed to a V-A spacetime structure to all charged current amplitudes. In order that a universal coupling be introduced for all weak interactions Cabibbo postulated that the amplitudes for the fundamental processes should take the following form:

lepton ---> neutrino : G
d-quark ---> u-quark : $G \cos\theta_c$
s-quark ---> u-quark : $G \sin\theta_c$

where θ_c, the Cabibbo angle ($\sin\theta_c = .23$), and G is the universal weak coupling constant. The idea was instrumented by forming a Cabibbo rotated d-quark,

$$d_c = d \cos\theta_c + s \sin\theta_c$$

and expressing the weak hadronic charged current as

$$J_{\text{weak}}(+,\text{had}) = \bar{u}\, \gamma_\sigma (1-\gamma_5)\, d_c$$
$$= \bar{u}\, d \cos\theta_c + \bar{u}\, s \sin\theta_c \;,$$

where the V-A structure is suppressed in the second term. The strength of the strangeness-conserving and strangess-nonconserving amplitudes were now governed by the sine and cosine of the Cabibbo angle, with the strangeness changing amplitude highly suppressed.

For completeness the purely leptonic charged current and electromagnetic current are recorded.

$$J_{\text{weak}}(+,\text{lep}) = \bar{\nu}\,\gamma_\sigma(1-\gamma_5)\;e + \bar{\nu}\,\gamma_\sigma(1-\gamma_5)\;\mu$$

$$J_{\text{em}}(0) = -\bar{e}\,\gamma_\sigma\,e \;-\; \bar{\mu}\,\gamma_\sigma\,\mu$$

Soon after, Bjorken and Glashow [7] proposed that a lepton-hadron symmetry could be patched into the Cabibbo theory if a fourth quark (charmed) existed and coupled to a Cabibbo rotated strange quark,

$$s_c = s\cos\theta_c - d\sin\theta_c$$

In SU(2) x U(1) gauge theories of weak and electromagnetic interactions quarks and leptons are placed into left-handed isospin doublets,

$$\psi_i = \begin{matrix} e \\ \nu_e \end{matrix}\;,\;\begin{matrix} \mu \\ \nu_\mu \end{matrix}\;,\;\begin{matrix} u \\ d_c \end{matrix}\;,\;\begin{matrix} c \\ s_c \\ ? \end{matrix}$$

Since no evidence existed for the existence of the last doublet, charm and the Cabibbo rotated s-quark, it is indicated as still being questionable. The expression for the charged currents is given by,

$$J_{\text{weak}}(+,\text{had}) = \sum_i \bar{\psi}_i \tau^+ \gamma_\sigma(1-\gamma_5)\, \psi_i$$

and necessary in weak isospin theories, a neutral current;

$$J_{\text{weak}}(0,\text{had}) = \sum_i \bar{\psi}_i \tau^0 \gamma_\sigma(1-\gamma_5)\, \psi_i \qquad .$$

If the Cabibbo rotated quarks are inserted into the above expressions for the charged and neutral currents the following equations are obtained:

$$J_{\text{weak}}(+,\text{lep}) = \bar{\nu}_e e + \bar{\nu}_\mu \mu$$

$$J_{\text{weak}}(0,\text{lep}) = \bar{\nu}_e \nu_e + \bar{\upsilon}_\mu \upsilon_\mu - \bar{e}\, e - \bar{\mu}\mu$$

$$J_{\text{weak}}(+,\text{had}) = (\bar{u}d+\bar{c}s)\cos^2\theta_c + (\bar{u}s-\bar{c}d)\sin^2\theta_c$$

$$\begin{aligned} J_{\text{weak}}(0,\text{had}) = {} & \bar{u}u - \bar{d}d\cos^2\theta_c - \bar{s}s\sin^2\theta_c \\ & - (\bar{s}d+\bar{d}c)\, s\cancel{i}n\theta_c \cos\theta_c \\ & + \bar{c}c - \bar{s}s\cos^2\theta_c - \bar{d}d\sin^2\theta_c \\ & + (\bar{s}d+\bar{d}c)\, s\cancel{i}n\theta_c \cos\theta_c \qquad ? \end{aligned}$$

where the hadronic neutral current has both strangeness changing and strangeness-conserving pieces. There was strong evidence that the strangeness-changing decays involving the weak hadronic neutral current were highly suppressed;

$$\Gamma(K^0 \rightarrow \mu\mu) \ / \ \Gamma(K^+ \rightarrow \mu\nu) << 10^{-7} \ .$$

Glashow, Iliopoulos, and Maiani, GIM, noticed that by introducing a doublet containing the new quark (charm) and the Cabibbo rotated s-quark, proposed earlier, the strangeness-changing portion of the weak neutral currents could be cancelled in first order. GIM also estimated a 1-3 GeV mass range for the new quark by considering the limit on $K_1 \rightarrow \mu\mu$. The cancellation of the weak neutral current in the context of an SU(2) weak isospin model became known as the GIM mechanism. The cancellation is indicated in the above expression for $J_{weak}(0,\text{had})$. Strangeness-conserving neutral currents were observed in 1973 [11] adding support to such isospin current constructions.

In the conventional model of Weinberg and Salam [12,13], based upon a non-abelian gauge theory and weak isospin doublets of quarks and leptons, the weak and electromagnetic forces between the charged and neutral currents are mediated by a set of intermediate vector bosons; see Figure 2. The hadronic selection rules contained in the charm changing part of the charged current are given below:

1. dQ = dC =dS (Cabibbo favored)
2. dQ = dC, dS=0 (Cabibbo suppressed)

The discovery of the charmed quarks [1,2] in November of 1974 completed the above picture of weak interactions and also gave rise to a host of experimental searches for the rich spectrum of charmed particle states predicted by strong interaction symmetries. At present a fifth b-quark [14] and a massive lepton [15] have been seen with predictions for more generations.

Charmed Particle Spectrum

Charm is a conserved quantum number of the strong interaction. The preexisting spectrum of mesons and baryons were well explained by an SU(3) flavor symmetry, including the three existing quark flavors; u (up), d (down), and s (strange). It was a natural consequence of this success to extend the model to include the charmed quark. Below is a list of quarks and their quantum numbers as given by SU(4) flavor symmetry.

quark	Q	I3	C	Y	S	B
u	+2/3	+1/2	0	1/3	0	1/3
d	-1/3	-1/2	0	1/3	0	1/3
s	-1/3	0	0	-2/3	-1	1/3
c	+2/3	0	1	-2/3	0	1/3

The list includes the four quark flavors with quantum number assignments for charge(Q), isospin(I3), charm(C), hypercharge(Y), strangeness(S), and baryon number(B). By combining quark and anti-quark under SU(4) we expect to find a singlet plus a 15-plet of states of pseudoscalar and vector mesons. The vector meson 16-plet appears in a matrix form as,

$$\begin{array}{ccccc}
 & u & d & s & c \\
\bar{u} & (\omega+\rho^{0})/2 & \rho^{-} & K^{*-} & D^{*0} \\
\bar{d} & \rho^{+} & (\omega-\rho^{0})/2 & \bar{K}^{*0} & D^{*+} \\
\bar{s} & K^{*+} & K^{*0} & \phi & F^{*+} \\
\bar{c} & \bar{D}^{*0} & D^{*-} & F^{*-} & \psi
\end{array}$$

The expected charmed pseudoscalars include the $D^{0}(c\bar{u})$, $D^{+}(c\bar{d})$, $F^{+}(c\bar{s})$, and $\eta^{c}(c\bar{c})$. Many of the vector and pseudoscalar states have been observed and studied [16]. A spectrum of charmed baryons is expected but their identification is proceeding at a much slower pace.

The massiveness of the charmed states and conservation of the charmed quantum number in strong interactions has a 3-fold consequence: (1) the lowest lying mesons can only decay weakly into lighter hadrons and leptons, (2) weak decay amplitudes mean narrow widths for the states, and (3) the massive charmed states have the potential to decay into many channels, reducing the probability for observing charm states through simple decays.

Charmed Particle Decays

If the standard SU(2)xU(1) theory of weak and electromagnetic forces is correct, all features of the weak decay of hadrons can be attributed to the weak interaction, the strong interaction, and the bound state nature of the hadrons. This decay of charmed particles has been envisaged [17] to take place through a spectator-nonspectator model of quarks in the hadron. A charmed particle is made up of a heavy quark (charmed) and light spectator quarks (u,d,s). Due to the relatively large mass of the charmed quark, strong interactions (gluon exchange) between the heavy and light quarks enter perturbatively. The charmed particle can then decay weakly in one of two modes described below.

In the first mode (Figure 3) the charmed quark and light quarks both participate in the decay. The $D^o(c\bar{u})$, Fig. 3a, can decay through the t-channel exchange of a W-boson, the resulting quarks recombining into a hadron final state. In the case of the $D^+(c\bar{d})$ and $F^+(c\bar{s})$, Fig. 3b-c, the heavy and light quarks annihilate into leptons or hadrons (a quark current is shown in the figure, but a lepton current is also allowed). Because the decaying mesons are spinless and because of the V-A structure of the weak interaction, these annihilation graphs are suppressed by two powers in the mass of the final state quark or lepton. The rate for pseudoscalar (D^+, F^+) decays into leptons is given by,

$$\Gamma(p \dashrightarrow l\nu) = (24\ \pi^2 F_p^2 M_l^2 / \ M_c^4)\ \ (G_f^2 M_c^5 / 192\ \pi^3)$$

$$= (.01)\ \Gamma_{sl}$$

where F_p is the pseudoscalar decay constant, M_c is the charmed quark mass, and M_l is the lepton mass. The first term in brackets has a nominal value of 1% and the second term will be shown to be a typical semi-leptonic decay rate. The purely leptonic rates are said to be "helicity suppressed".

In the second mode of decay, Figure 4 , the charmed quark and light quarks remain independent. The decay is triggered by the charmed quark transferring a W-boson to an external lepton or quark pair while making a transition to an s-quark; for example. The quarks then hadronize with unit probability. Ignoring phase space corrections, and light quark and lepton mass differences; the rate for these graphs is just the rate for muon beta decay.

$$\Gamma(\mu \dashrightarrow e\nu\nu) = G^2 M^5 / 192\,\pi^3 = \Gamma_{sl}$$

By placing the charmed quark mass in the formula for M we have an expression for the rates of charmed particles decaying into hadrons or leptons. We can estimate the semileptonic branching fraction by noting that the there are two lepton graphs and three colored graphs for hadrons.

$$1/2 \text{ rate}(c \dashrightarrow l\nu x) = 1/3 \text{ rate}(c \dashrightarrow x) = \Gamma_{sl}$$

The total rate is then given by

$$\Gamma(c \rightarrow X\ ) = (2 \text{ leptons} + 3 \text{ colors})\ \Gamma_{sl} \cdot \rho$$

$$= (\ 5\ )\ \Gamma_{sl} (\ 1/2\ ) = 1.5 \times 10^{+12} \text{sec}^{-1}$$

The 1/2 multiplier is a phase space reduction factor, ρ, due to the strange quark mass. The semi-leptonic branching fraction is 20% in this first order approximation.

The estimate can be improved by making strong interaction corrections (gluons to leading order). The semi-leptonic rate with QCD corrections [18,19] is given by,

$$\Gamma^{QCD}_{sl}(c \rightarrow l\nu X) = (1 - \alpha_s/2)\ \Gamma_{sl} \simeq 2/3\ \Gamma_{sl}$$

and similar corrections to the non-leptonic rate [20].

$$\Gamma^{QCD}_{nl}(c \rightarrow X) = (\ f_+ + f_-\ )\ \Gamma_{sl} \simeq 5\ \Gamma_{sl}$$

The quantities in brackets (f_+, f_-) are the gluon corrections to the hadronic weak current. The semi-leptonic branching fraction including QCD corrections is then,

$$BF(c \dashrightarrow l\nu x) = 2/3\ /\ (\ 2/3 + 2/3 + 5\ ) = .11\quad ,$$

The QCD corrections have reduced the semileptonic branching fraction by approximately a factor of 2.

The light quark spectator model also predicts that all the lowest lying charmed states should have equal lifetimes. This is a simple consequence of the nonparticipation of the light quarks in the decay process; thus the charmed quark decays in an identical manner for all charmed hadrons (ignoring mass differences). It also follows from isospin considerations that the semi-leptonic rates for all charmed particle decays are equal up to phase space corrections [21]. This allows a direct comparison between semi-leptonic branching fractions and lifetimes.

Experimentally the lifetimes of the $D^o(c\bar{u})$ and $D^+(c\bar{d})$ are measured to significantly differ [22]; the approximate ranges given below:

$$\tau\ (D^+) = (1.-16.) \times 10^{-13}\text{sec.}$$

$$\tau\ (D^o) = (1.-\ 5.) \times 10^{-13}\text{sec.}$$

In addition the semileptonic branching ratios are measured to differ,

$$BR(D^o \dashrightarrow l\nu X) = (5.5 \pm 3.7)\%\ [23]$$
$$= (<4.\ )\%\ [24]$$

$$BR(D^+ \dashrightarrow l\nu X) = (16.8 \pm 6.4)\%\ [23]$$
$$= (22.0\ {+4.4}\ {-2.2})\%\ [24]$$

These results are internally consistent with the expectation that the ratio of lifetimes varies as the ratio of branching ratios but are inconsistent with the light quark spectator model prediction of equal lifetimes for charmed particle states. Theoretical remedies for enhancing the lifetime ratio of D^+ to D^o include:

circumventing the helicity suppression graphs of Figure 3 by including gluons in the initial state wave function [25] or in the final state [26]. The methods increase the non-leptonic decay modes of the D^o while the relieved decay modes of the D^+ remain Cabibbo suppressed. In another theoretical scheme of "sextet dominance" [27] final state interference between D^+ nonleptonic decays, Figure 3b, reduce their decay width relative to the unaffected D^o width, Fig. 3a.

C. Hadronic Charm Production

As yet, there is no firm theory of hadronic charmed particle production. The major effort to explain production mechanisms has been within the context of perturbative QCD and hard scattering models [28].

Hard Scattering

The hadronic charmed production cross section at center of momentum $\sqrt{s}$, for colliding hadrons A and B is expressed as,

$$\sigma_{cc}(s) = \sum_{1,2} \int dx_1 dx_2\, F_1^A(x_1,Q)\, F_2^B(x_2,Q)\, \frac{d\sigma_{1,2}(s')}{x_1\, x_2}$$

$$x_1, x_2 \quad \text{such that} \quad M_{cc} < s' < s$$

The subscripts 1 and 2 refer to constituents (quarks or gluons) contained in hadrons A and B. All subprocesses contributing to the scattering are summed over. The functions $F(x,Q^2)$ are probability densities for finding constituent 1(2) with the fractional longitudinal momentum $x_{1(2)}$ in the parent hadron when probed at a four momentum transfer of Q^2. The square of the QCD matrix element for the relevant subprocesses is given by $d\sigma_{1,2}$, at subprocess center of mass energy $\sqrt{s'}$. The accuracy of the calculations is bounded by; (1) a proper knowledge of the probability density functions (structure functions) for valence quarks, sea quarks, and gluons in the colliding hadrons, (2) the choice of the integration limits, (3) choice of the strong coupling constant, and (4) uncertainties in double counting certain contributions. These limitations are discussed by [29].

Depicted in Figure 5a&b are the graphs representing the fundamental quark-quark (q-q), and quark-gluon (q-g) interaction mechanisms that are believed to contribute to the hadronic production of charmed particles in leading order.

In the "quark annihilation" graph, Figure 5a, the quark and anti-quark pair from the colliding hadrons annihilate into a gluon producing a charmed quark pair. The charmed quarks are then believed to hadronize into an associated charmed particle pair. The second graph, Figure 5b, is of the "gluon fusion" type. A gluon from each colliding hadron "fuse" to form the charmed quark pair which then hadronize as before. These diagrams share the common attributes that the parton distributions fall off quite rapidly in the initial hadrons with longitudinal momentum fraction x, and the differential cross sections for the fundamental parton interactions decreases roughly as the inverse of the parton-parton center of mass energy, s', [30]. As a consequence charmed particle production will peak near the charmed quark production threshold, and be highly sensitive to its value.

The quark annihilation and gluon fusion diagrams contribute to the central production of charmed particles, small x, and calculation of cross sections can be made to vary in the 1-20 microbarn range by adjusting integration parameters. An experimentally favored charmed production cross section of 10-20 microbarns in hadron collisions [31] at FNAL/SPS energies ($\sqrt{s}$ 27.5 GeV) is accommodated by the calculation of Carlson and Suaya [32], but most calculations fall short of the range by an order of magnitude.

Reports from the ISR [31] indicate that the charmed production cross section might be as large as several hundred microbarns at these center of mass energies; and more profoundly, the charmed particle longitudinal momentum distribution extends to high values of X_F, contradicting then existing QCD calculations. This cross section enhancement and diffractive-like production can be understood within perturbative QCD calculations by including the "flavor excitation" graph in Figure 5c.

A light quark or gluon from one hadron interacts with a charmed quark from the sea of the other hadron producing a charmed particle final state. The graphs were initially viewed as having little contribution due to the small charmed sea component of the hadron. Combridge showed [33] that this was not the case and the contribution from the "flavor excitation" graphs depended critically on the value of Q_{min} at which the charm sea begins to contribute to the hard scattering process. Brodsky et.al. [34] and Barger et.al. [35] have devised mechanisms by which the charmed sea distributions obtain a "hard" X_F dependence reproducing the reported diffractive-like behavior of the ISR data. In short, the somewhat more controversial "flavor excitation" graphs can contribute to the total charmed particle cross section at both FNAL/SPS and ISR energies and understanding the admixture of the three processes (contributing in both overall cross sections and kinematic distributions) awaits exerimental input.

Experimental Evidence

Experimental evidence for charm production at FNAL/SPS energies comes from two types of experiments. In the "beam dump" technique a hadron beam is directed into a totally absorbing target and the emerging muon or neutrino yield is measured. The prompt component (leptons from charmed quark decays and electromagnetic sources) were extracted either by taking yields as a function of absorber/target density and extrapolating to to infinite density and/or modeling the lepton contribution from background hadron decays and electromagnetic sources ,and subtracting. Bodek et al. [37], using the density extrapolation technique to extract a direct muon signal from an expandable beam dump, report a charmed particle production cross section of 24.6(±2.1,±3.3) microbarns/nucleon in 350 Gev/c proton-Fe interactions. The first error is statistical and the second is systematic. In 278 Gev/c pion-Fe interactions they report a D-meson production cross section of 9.1(±1.0,±2.3) and for $\bar{D}$-meson production a cross section of 10.6(±0.7,±2.8) microbarns/nucleon. The proton data indicates equal numbers of direct muons of each sign, but in the pion data an approximate 2:1 asymmetry is observed; favoring negative signed muons.

Searches for signals in invariant mass distributions have yielded scant results. Fitch et al.[38] have searched for $D^{*+}(D^{*-})$ by triggering on a K-π system in coincidence with a slow pion. The trigger takes advantage of the small mass difference between D^* and D meson, and the large branching ratio of $D^* \rightarrow$ D-Pi (.64+-.11). They report a cross section for charged D^* production by 200 Gev/c pions on beryllium to be 4.2±1.4 microbarns/nucleon. The ACCMOR collaboration [39] ,operating at the CERN SPS, have searched for associated production of charmed hadrons with a prompt electron trigger in 175 Gev/c pion-Be interactions. They report a charged D^* production cross section of 17.(±3.,±10.) microbarns/nucleon and assuming an equal D/D^* production ratio the extrapolated $D-\bar{D}$ production cross section is given as 34(±8,±24) microbarns/nucleon. Both experiments rely on the small D^*-D mass difference to observe small enhancements in $K-\pi$ mass plots from which the cross section levels are set.

At ISR energies ($\sqrt{s}$ =60 GeV) the charmed production cross section has been reported to be an order of magnitude higher [31]. Significant D-meson and charmed Lambda signals are observed, with charmed lambda production favoring a diffractive mechanism, and D-meson production favoring a central model.

D. Prompt Muon Trigger

The execution of a prompt muon trigger in a spectrometer format takes advantage of the special properties of charmed particle production and decay, previously discussed: (1) an associated production mechanism, (2) a relatively high semileptonic branching ratio (10%), (3) short lifetimes that constrain decays to within a few millimeters in the lab, and (4) a transverse momentum spectrum characteristic a massive particle decay. A potentially powerful triggering technique can be developed by keying on the muon emerging from the semileptonic decay of the first charmed particle and subsequentially analyzing the decay products of the second. Table 1 lists the dominant sources of muons from charmed particle decays. Note that the short lifetimes insure that the charmed particles will decay within a few hundred microns of their creation, thus the description "prompt or direct".

Background Sources

The limiting factor in such a trigger is the large muon background from weak decays of hadrons and electromagnetic dimuon production. These background sources are listed in Table 2 and Table 3.

Since the mean decay lengths for pions and kaons are tens of meters they may be intercepted in flight by a dense absorber as they exit the target. Pion and kaon decays are referred to as "non-prompt sources" due to their long lifetimes. Semileptonic decays of hyperons are waived as a source of trigger background due to their small production cross sections and small branching fractions into muons($\sim 10^{-3}$); yielding a negligible overall rate.

Electromagnetic dimuons are produced at a prompt rate, thus competing directly with charm particle decays at the trigger level. The dominant sources of dimuons are from (1) low mass continuum production (Bethe-Heitler pairs), and the broad ρ-ω resonance decays. Muons from these sources are produced with low values of transverse momentum (P_t), and can be effectively rejected by imposing a P_t cutoff at the trigger level. Figure 6 and Figure 7 show the expected momentum and transverse momentum distributions of muons from the prompt and non-prompt sources.

The "prompt muon trigger" was implemented by introducing a dedicated trigger arm into an open geometry forward spectrometer, Figure 1. The trigger arm geometry is fixed so as not to constrict the forward detector acceptance to a high degree; primarily a matter of selecting the kinematic region of interest to the trigger (P_t >.4GeV), convenience, and the rate capabilities of the spectrometer. The trigger was initiated by a counter telescope, imbedded in a thick hadron absorber. The initial absorber was placed as near the target as possible, suppressing non-prompt decays in flight. The a[illegible] free flight path afforded to a hadron in the E515 geometry was about 10 cm. The decay probability for pions can be estimated as follows.

$$P_{decay} = \frac{\langle \text{decay length} \rangle}{\gamma c \tau} = \frac{.2 \text{ meters}}{57. \text{x } 7.8 \text{ meters}}$$

$$= 5. \text{x } 10^{-4}$$

Here the average decay length is the free flight path plus one absorption length of the absorbing material (10 cm for W). The calculation assumes pions with a mean energy of 10 Gev in the laboratory. An additional suppression, not included in the calculation, derives from the energy degradation of the secondary muon resulting from decay kinematics, or energy loss in the absorber.

Trigger Acceptance

The integrated acceptance for triggering on a prompt muon from charmed particle decay (central production model) calculated for the E515 geometry is about 7%. The charmed particle production models are discussed in Chapter 3. This can be compared with the modeled [42] acceptance for muons, from pion and kaon decays, at a level of 1%, and muons from dimuon sources [41] at a level of 1.5 %. A crude estimate of the ratio of trigger muons from charm production to muons from nonprompt background can now be made.

$$\frac{\mathrm{trig}_{c\bar{c}}}{\mathrm{trig}_{\pi\to\mu}} = \frac{\sigma_{c\bar{c}} \times \mathrm{BR}_{\mu} \times \mathrm{ACC}_{\mu}}{\sigma_{abs} \times \langle\mathrm{multiplicity}\rangle \times P_{d} \times \mathrm{ACC}_{\pi\to\mu\nu})}$$

$$= \frac{(20\ \mu b) \times (.1) \times (.07)}{(21\ mb) \times (7) \times (.0005) \times (.01)} \simeq .2$$

This shows the excellent potential for non-prompt background rejection.

Mentioned above, the main line of action for rejecting triggers from electromagnetic sources was the low transverse momentum cutoff introduced by the muon spectrometer arm. Figure 8a-b shows the momentum and P_t acceptance for the trigger arm. Convoluting the P_t acceptance with the dimuon transverse momentum spectrum in Figure 7 results in the low integrated acceptance for muon triggers from electromagnetic sources. In a similar calculation to that above, the charmed particle to electromagnetic trigger ratio is given by:

$$\frac{trig_{cc}}{trig_{\mu\mu}} = \frac{\sigma_{cc} \quad BR_{\mu} \quad ACC_{\mu}}{\sigma_{\mu\mu} \qquad ACC_{\mu}} = \frac{20\mu b \quad .1 \quad .07}{2.2\mu b \quad .015} \simeq 4.$$

The ratio of triggers from non-prompt sources to charm sources to electromagnetic sources is then about 100:20:5. These estimates don't include accidental triggers involved with muon halo, hadronic showers ranging through the absorber, delta rays, and other sources. Efforts were made both in experimental design and off line analysis to keep sources of accidental triggers at a minimum.

Figure 8c shows the Feynman X ($X_F=P^{cm}/P^{cm}_{max}$) acceptance of the trigger arm for direct muons; and the X_F acceptance of the forward spectrometer and shower detector for electrons. The trigger arm is situated about 90 degrees in the center of mass, accepting muons in a range of $X_F=\pm.1$, and is most sensitive to the central production ($X_F=0.$) of charmed particles. The spectrometer acceptance for forward electrons is high, and approximately independent of X_F. The associated production of charmed particle pairs by hadronic collisions, in terms of dynamics and species, is still an open question. Triggering on a muon from a centrally produced charmed particle will no doubt bias the spectrum of associated observed electrons; in particular, if the mean rapidity gap between charmed particles pairs is small.

The search for an opposite sign muon-electron coincidence between the muon trigger and forward electron will be sensitive to this issue, and may shed some light on the subject.

CHAPTER 2

Experimental Apparatus

A. Beam

Beamline

Experiment 515 was performed in the M1 West beamline at the Meson Detector Building, Fermi National Accelerator Laboratory. The beamline was designed to transport 200 GeV negative pions to the experimental area at an intensity of approximately 10^7 pions per accelerator cycle. The secondary pion beam was derived by directing a fraction of the primary proton beam ($3x10^{12}$ protons at 400 GeV) onto the Meson Laboratory central target. The resulting negative secondaries (3.6 mrdn. production angle) were magnetically selected, momentum focused, and transported to the experimental area, about 500 meters away. The beam content near production target was an admixture of about 95.7% negative pions, 3.5% negative kaons, and .8% anti-protons [43]. Accompanying the beam to the experimental area was a considerable muon halo, either produced directly at the target or from in-flight decays. A determination of the beam momentum with the spectrometer dipole gave an average momentum of 207.6 GeV with an r.m.s. spread of 1.5 percent.

Standard beamline elements, including dipole and quadrupole magnets, collimators, intensity and profile monitors were used in the beam transport and monitoring. The components are listed in Table 4 for reference. The power supplies regulating these beamline elements were controlled through a beamline control console [44] located in the experimental area. SEM intensity readings (secondary emission monitors), available at points along the beamline, were helpful in reducing transport losses. Profile monitors located along the beamline allowed direct observation of the horizontal and vertical beam profiles on TV scanners located in the experimental area.

In normal running situations about $5.\times 10^6$ beam particles were directed onto the experimental target per one second spill. The beam rates were closely monitored by an overlapping pair of scintillation counters, B1 and B2, placed in front of the experimental target. (The coincidence of B1•B2 was scaled during the run for determining total integrated beam flux on target). These counters were equipped with phototube bases [45] capable of handling average rates of 10^7/sec.

For shower detector calibration purposes the beamline was tuned to transport a predominantly low momentum electron beam to the experiment area. The tunes were accomplished by scaling the magnet power supply setting for the 200 GeV beamline tune to the reduced momentum values. The momentum tunes ranged from 10-30 GeV with beam rates of approximately 10^5 particles/sec.

Time Structure

Primary beam was delivered for a one second interval, every ten seconds, onto the meson central target. The resulting secondary pion beam was available for about half of the one second spill due to 60 Hz and other macro-structure introduced during injection and extraction of the primary proton beam. The beam spill showed an erratic behavior at the beginning and end of each cycle. In order to avoid logging data during these periods a "beam gate" was formed, singling out the stable part of the spill structure. This gate was folded into the trigger logic, requiring that it be "on" in order to record data.

Superimposed on this macro-structure was the characteristic 18.5 ns r.f. (bucket) structure introduced in the proton acceleration process. Beam particles arrived at the experimental area in 2 ns buckets separated by 18.5 ns intervals. This time structure was exploited in timing the trigger electronics, by assuring that all triggers originated from a single r.f. bucket.

A naive calculation gives the probable bucket occupancy: Over the 1/2 second of useful spill about $5.\mathrm{x}10^{7}$ buckets existed. At average intensities of $5.\mathrm{x}10^{6}$ pions/spill, the mean bucket occupancy was .2 pions/bucket. Appealing to Poisson statistics, the probability for no occupancy $p_o=e^{-.2}=.82$, the probability for single occupancy is $p_1=.2\mathrm{x}e^{-.2}=.16$, and the probability for double occupancy is $p_2=1/2\mathrm{x}.2^2\mathrm{x}e^{-.2}=.02$, and etc. The beam counters recorded hits whenever minimum ionizing threshold was met, with no distinction to occupation number. The actual number of pions on target should be scaled up by approximately the factor (call it α),

$$\alpha = (p_1+2\cdot p_2+\cdots)/(p_1+p_2+\cdots)\simeq 1.1 \quad .$$

The Poisson approximation tends to underestimate the multiple occupancy problem due to the unrealistic tails of the distribution. An experimental estimation of the multiple bucket occupancy was made during the run by scaling the quantity $B_1 \cdot B_2$(delayed), where B_2 was delayed by 1 r.f. bucket. If particles occupy buckets independently, the ratio

$$\frac{B_1 \cdot B_2(\text{delayed})}{B_1 \cdot B_2} = \alpha_{exp} \approx .2$$

is a better estimate of the fraction of buckets with multiple occupancy. The scale factor α is about 1.2 through this determination. The imprecise knowledge of this quantity will lead to a systematic error of 10-20% when calculating cross sections.

Strong Focusing and the Target

All data in the experiment was taken with a beryllium target. It measured 2 mm vertically, 10 cm horizontally, and 3 cm in depth. The small vertical size was chosen in order to place the target at a minimum distance from a hadron absorber; fulfilling the trigger philosophy. A schematic of the beamline upstream of the target is shown in Figure 9. The major strong focusing of the pion beam was accomplished by a pair of large aperture quadrupoles connected in tandem about 15 meters in front of the target. They allowed a verticle beam focus of less than 1/2 mm rms deviation. (The size of the beam at the target can be described as a ellipse of minor axis (vertical) 1/2 mm and major axis (horizontal) 2 cm.). A final vertically pitching dipole was used to center the beam on the beryllium target with the aid of the overlapping beam counters B1 and B2. The beam counter coincidence rates were continually monitored, insuring careful focusing of the beam onto the thin vertical target.

The horizontal position of the beam at the target was determined by a set of three small multiwire proportional chambers (BMX0, BMX1, and BMX2 in Figure 9). One millimeter anode wire spacing and their placement along the beamline allowed the horizontal beam position at the target plane to be resolved within 1/2 mm. Table 5 lists additional information on the beam chambers.

Halo muons, interactions occurring upstream of the target, and energetic photons accompanying the beam could potentially pose problems to the highly selective muon trigger. A veto wall of counters (A1-A9 Figure 9) shadowed the muon trigger arm and target region, rejecting triggers from muon halo. In a similar action, energetic photons were converted in a 20 radiation length Pb radiator surrounding the beam pipe near the final vernier dipole (Figure 9). Any showers detected by veto counters near the target rejected the trigger. Finally, a helium filled polyethylene bag (5 mil walls) was placed in available space along the open beam to reduce upstream interactions.

B. Trigger

The experimental trigger consisted of a signal from a beam particle in counters B1 and B2, detected in coincidence with a secondary penetrating the full extent of the muon trigger telescope (M0, M1, M2, M3; see Figure 1). It was vetoed on a coincident signal in any of the veto counters, A1-A9 (see Figure 9). The trigger can be expressed as follows,

$$\mathrm{TRIG} = \mathrm{B1}\cdot\mathrm{B2}\cdot\mathrm{M0}\cdot\mathrm{M1X}\cdot\mathrm{M1Y}\cdot(\mathrm{M2}\cdot\mathrm{M3})_X\cdot\bar{A}$$

B1 and B2 are the beam counters; M0 are the trigger counters embedded in the steel absorber near the target; M1X and M1Y are horizontal and vertical elements of the M1=hodoscope; M2 and M3 are the trigger counters downstream of the magnet; and A are the veto counters shadowing the trigger telescope. Table 6 lists elements in the trigger telescope; their positions, and sizes. Two other types of triggers were simultaneously recorded: beam triggers ($\mathrm{B1}\cdot\mathrm{B2}\cdot10^{-7}$) for alignment purposes and diagnostic test triggers (issued between beam spills) for monitoring the response of various detector devices.

Logic

The trigger logic diagram for the 26 cell M1 hodoscope is shown in Figure 10. The trigger demanded a time coincidence from at least one x-y pair on the east side or at least one x-y pair on the west. The widths of the logic pulses produced by each counter were adjusted to 10 ns, as were the output of all logic gates. The $(M2 \cdot M3)_x$ coincidence enforced a preselected trigger pattern between counters of the M2 and M3 hodoscopes. The logic diagram for the M2-M3 trigger matrix is shown in Figure 11, and the matrix pattern is clearly displayed in Figure 12.

The trigger was developed within 250 ns of the time of an interaction occuring in the target. This value was limited by particle transit distances, counter delays, and logic gate delays in the trigger formation. The discriminated outputs from each element in the trigger telescope were stored in CAMAC Model 2341 coincidence registers (latches) on each trigger, and were logged in the data record for that event.

A schematic of the full E515 trigger is shown in Figure 13. Most logic elements in the trigger were formed with Lecroy fast NIM electronics. This harware trigger then initiated the latching of data for that event in the various spectrometer devices, and also signaled for the start of a computer read cycle.

C. Muon Trigger Arm

The muon trigger arm (Figure 1) was dedicated to making a fast trigger decision based upon the production and penetration of a secondary muon through the system. Suppression of non-prompt muons at the trigger level from pion and kaon decays was accomplished by the placement of a tungsten-iron hadron filter as near the target as possible; absorbing hadrons before decay. This W-Fe absorber, the magnetized return yoke of the spectrometer magnet, and an additional hadron absorber in the rear, encased the muon trigger telescope, shielding it from hadron penetration. The telescope was tilted up at a vertical lab angle of 40 milliradians and subtended an angular range of approximately +40 to +130 mrdn., vertically, and ±125 mrdn., horizontally. The trigger particle received an approximate .75 GeV transverse momentum kick in the polarized iron yoke of the forward spectrometer magnet. By measuring the deflection angle of the particle in the magnetic field, a charge and momentum determination was made.

Hadron Filter and Trigger Counters

In order to minimize the free flight path for hadrons that emerged from the target, a tungsten and iron filter was placed immediately behind the target (Figure 14). The lower edge of the absorber defined a 40 mrd vertical plane. The top of the target was 1 mm below the first tungsten absorber block. This section of absorber extended 1 meter in depth and consisted of machined blocks of tungsten and steel. Tungsten blocks comprised the first 15.24 cm of absorber, with steel making up the remainder.

Two trigger counters, M0 and M00, were imbedded in the W-Fe filter, requiring particles to enter the absorber in the first 20 cm of flight. The counters were .476 cm (3/16 inch) thick plastic scintillator with light guides connected to Amperex 56AVP photomultiplier tubes. The output signals were discriminated at minimum ionizing levels.

At the end of the W-Fe filter a 26 cell scintillation counter hodoscope (M1) gave the horizontal and vertical position of the trigger particles at that depth. A schematic of the hodoscope is shown in Figure 15. The elements were .32 cm (1/8 inch) thick plastic scintillator, overlapped by 1/3 their width, producing an effective 1 cm cell size. By combining the hodoscope coordinate with the interaction vertex position at the target a track segment could be defined for particles entering the magnet. The approximate 10 mrdn. angular resolution of the hodoscope was compatible with the multiple scattering error incurred in the 1 meter of absorber between the target and M1 hodoscope.

The polarized iron return yoke of the spectrometer dipole was the next section of absorber encountered in the trigger arm. In the 1.2 meters of steel particles received a .75 GeV transverse momentum kick, sweeping out low momentum muons. The four element trigger hodoscope (M2) defined the angular acceptance at the magnet yoke exit. The paddles were made of .32 cm (1/8 inch) thick plastic scintillator with light guides coupled to 56AVP photomultiplier tubes. The paddles measured 35.6 cm (14 inches) in width and 40.6 cm (16 inches) in height. The light guides connecting the counters and tubes were elongated, keeping the 56AVP photomultipliers away from the magnet fringe fields.

A final 40.6 cm (16 inches) of absorber shielded the last muon trigger hodoscope (M3). The filter suppressed triggers from delta rays and hadrons encroaching from the forward spectrometer arm. The six counters of the M3 hodoscope were constructed of .32 cm (1/8 inch) plastic scintillator with light guides connected to 56AVP photomultiplier tubes. The paddle sizes measured 35.6 cm (14 inches) horizontally, and 50.8 cm (20 inches) vertically. The phototube output signals were discriminated at minimum ionizing levels.

Proportional Wire Chambers

The multiwire proportional chambers instrumenting the muon trigger arm were built by Northwestern University. (The details of construction and operation of multiwire proportional chambers is discussed extensively elsewhere [46].) The set consisted of three chambers measuring horizontal coordinates, three chambers measuring vertical coordinate, and two chambers measuring coordinates in a rotated coordinate frame (± 30 degrees to vertical). Their positions are given in Figure 1 and in Tables 7. They were positioned between the magnet yoke exit, and rear muon hodoscope, spanning a 2 meter longitudinal interval along the beam axis. With a 6 mm effective anode wire spacing, the resulting angular tracking resolution was approximately 10 mrdn.; compatible with multiple scattering errors incurred in traversing the hadron absorber. The MWPC tracking insured a clean trigger and also allowed a charge and momentum determination of the triggering particle.

The chambers were of steel-frame construction, with each chamber frame housing a signal plane of anode wires (1 mil Au-W), between two wire cathode planes (3 mil Au-W). The anode wire spacing was 3 mm, with adjacent anode wires electronically connected to give an effective 6 mm cell size. The chambers operated on a gas mixture of 70% argon and 30% isobutane, at cathode potentials of -3. to -3.5 kV.

A schematic of the MWPC read out electronics is shown in Figure 16. Each amplifier channel consisted of an amplifier/discriminator, delay circuit, and latch device. There were 16 wire channels per amplifier card, and a total of 119 cards in the system. The amplifier cards were located on a chamber backplane and directly connected to the MWPC sense wires. Analog signals induced on the sense wires after the passage of a charged particle were amplified and discriminated to TTL logic levels. The signal (indicating a wire hit) was delayed by a 450 ns passive delay circuit, giving time for the trigger to develope. If the trigger was satisfied, (1) all wire latches were first cleared ("off"), (2) gate signals were issued to all latches, and (3) if the gate signal arrived in timed coincidence with the discriminated wire pulse, the latch was set "on". If any of the 16 wire latches on a card were set, a MOR (Memory OR) line, dedicated to that card, was set in an "on" condition.

Groups of amplifier cards were serviced by a scanner card, an encoder/driver card, and receiver card; also located on the MWPC backplanes. Five backplanes (21-24 amplifier cards each) were linked to a CAMAC interface/memory model via a 300 ns twisted pair data transmission line (system bus). Upon receiving an event trigger, the CAMAC interface module drove the following sequence of events: (1) the first backplane on the system bus was signaled to begin a clocked scan of it's MOR lines, (2) if a MOR was "on" (indicating at least one wire "hit"); the 16 wire channels, a binary encoded card number, and a binary encoded backplane number were strobed onto the system bus. (3) the interface module encoded a 16-bit word for each hit in that card and stored it in a 1K CAMAC buffer memory, (4) scanning of MOR lines continued with steps (2) and (3) repeating for all cards on the backplane; when finished an "end" of of scan was issued to the interface module, (6) the interface initiated the scan of the next backplane, and etc. All wire hits were thus stored in the CAMAC buffer memory as 16-bit words from which the wire position could be decoded in analysis. Typically 10 wire hits were recorded per event.

D. Forward Arm Spectrometer

The hadron state produced in association with a muon trigger was reconstructed in the forward arm of the spectrometer. The forward detector arm subtended horizontal angle of ±200 mrdn. and a verticle angle of -80 mrdn. to +40 mrdn. Charged particles were tracked with a system of proportional wire and drift chambers. A 46 cell Cerenkov counter discriminated pions from kaons in the momentum range 6.5 GeV to 22 GeV. Electrons and neutral pions were identified in a lead/liquid argon electromagnetic shower detector. A scintillator and proportional tube hodoscope array positioned at the rear of a hadron dump was used to identify muons penetrating the dump.

Proportional and Drift chambers

Twelve planes of proportional chambers and two drift chamber planes were used to track charged particles in the forward spectrometer arm. Their positions are given in Figure 1 and Tables 8-9.

An X-Y pair mounted at the magnet entrance gave position information on particles entering the analyzing magnet. The hit density in this pair was normally high, rendering them ineffective in tracking. They were used to resolve vertex ambiquities in a later stage of the analysis.

The remaining set of chambers were positioned between the magnet exit and Cerenkov counter. There were four horizontal planes, three vertical planes, three rotated planes of proportional chambers, and two horizontal drift planes. They were used to find the trajectory of charged particles exiting the spectrometer analyzing magnet. From the tracking information and the interaction position the momentum for each tracked particle in the event was determined. These tracks could be extrapolated into the Cerenkov counter, shower detector, and rear muon hodoscope for particle identification during analysis. The angular resolution of the MWPC system was determined to be .350 mrdn. giving a fractional error, dp/p, of 1%-2% in particle momenta determination.

The proportional wire chambers were constructed by Carnegie-Mellon University. The chambers mounted to the spectrometer magnet had active areas of 1.2 x .4 square meters covering the magnet aperture. The anode wire spacing in the magnet chambers was 1 mm for the upstream x,y set, 1 mm for the downstream y plane, and 2 mm for the remaining x,u pair. The chambers had foil cathodes and operated on a magic gas mixture of 80% argon, 19%

isobutane, 1% freon, and trace of methanol. The 1 mm magnet chambers ran at a cathode potential of -5 kv and the 2 mm magnet chambers operated at a lower potential of -3 Kv.

The remaining set of large MWPC's had active areas of 2.5 x 1. square meters covering the full spectrometer angular acceptance at the magnet exit. The chambers were constructed with wire cathode planes and had 2 mm anode wire spacing. The chambers operated on a gax mixture of argon-CO_2 (9:1) at a cathode potential of -3 to -4 kilovolts.

The chamber read out system consisted of a front end amplifier to convert the analog wire signal to a discriminated logic pulse, a delay element to stretch the data while a trigger decision was made, and a latch to store the data until the computer read out cycle. In order to handle single wire rates of up to 4 MHz a high rate PWC read out system, based on the ECL-II (emitter coupled logic) family of logic, was developed. A detailed discussion of the read out system is found elsewhere [47].

The central region of all forward arm MWPC's, including the beam chambers, was read out by a "hadron fast amp" system. This was the region in which non-interacting beam passed and in general intercepted the highest particle fluxes. Thus it was important that the read out system had high rate capabilities. Data was latched in a crate system at the end of an active delay line away from the chambers. Since no dead time is produced in the delay element, all dead time is incurred in the front amplifier-discriminator and cable line driver. Single wire rates of up to 4 MHz could be reliably latched.

The chamber wings were read out by the "hadron slow amp" system. The delay element consisted of two parallel one- shots. Alternate pulses are fed through the one-shots and data is lost only if a third pulse occurs at the input within the one shot delay time. The data latching occurred directly on the wire read out card. A single wire latching rate of up to 1 Mhz could be achieved.

As in the case of the muon trigger arm MWPC's, the wire hits in the spectrometer arm tracking system were recorded as 16-bit words (wire number, card number, and chamber number) in two 1K CAMAC buffer memories. These data transfers were initiated on an event trigger and were mediated by controllers and CAMAC interface modules dedicated to that service. Typically 100-200 hits registered in the forward spectrometer system per event.

The two drift chamber planes were constructed at University of Notre Dame. They were positioned at the rear of the tracking system and measured coordinates in the horizontal dimension. Although drift chambers are hampered by inefficiencies at high rates, the intention was to use their superior position resolution in refining momentum calculations.

Each chamber contained 96 drift cells, of 2 cm horizontal dimension, with an anode wire in the center. They operated on an argon-ethane gas mixture (1:1) and had a full scale drift time of about 200 ns. The position resolution of each plane was determined to be on the order of 300 microns.

Drift chamber time information was processed by a Lecroy drift chamber encoding system. The analog wire signals were discriminated and transformed to ECL logic pulses. These were transmitted on a system bus to a Model 2770A TDC (time to digital converter) as a "start" condition. A common "stop" for all channels was provided by the event trigger, delayed by a time interval largely dependent on the full scale drift time of the cells. The position address (drift cell number) and time interval between "start" and "stop" pulses were digitized and stored for each drift chamber hit.

Magnetic Field

A 40D48 spectrometer dipole magnet provided the magnetic field for charged particle momentum analysis. The vertical aperture size was 15 inches and the horizontal aperture size 40 inches. The magnet had a depth of 48 inches with an effective field length of 1.2 meters. At a normal running current of 2400 amps the central field value was 18.75 kg. A helium filled bag with 10 mil polyethylene walls was placed into the magnet aperture in order to reduce secondary interactions.

Cerenkov Detector

The Cerenkov detector (Figure 17) was constructed by the University of Notre Dame. It used nitrogen gas at a pressure of one atmosphere as the Cerenkov radiator, and operated in a conventional threshold mode. A charged particle traversed about 4.6 meters of gas before exiting, producing on average 8 detected photons. Cylindrical mirrors focused the light into 46 (RCA 4522) photomultiplier tubes placed above and below the beam axis.

The light output from each tube was amplified by a factor of ten and transmitted along low-loss coaxial cable to Lecroy Model 2249A CAMAC ADC's (analog to digital converters). The ADC's operated in the charge sensing mode and integrated during a selected gate interval of 100 ns.

Lead - Liquid Argon Electromagnetic Calorimeter

The electromagnetic shower detector was constructed by Northwestern University. It consisted of a 28 layer ionization cell stack (anode strips + cathode planes), finely sectorized in the X and Y lateral dimensions; all immersed in a liquid argon filled stainless steel dewar (Figure 18). An electromagnetic shower initiated by the dense radiator (Pb), generated a residual charge in the liquid argon, of which a fraction was collected by the anode strips and amplified. The amplified signal was proportional (within sampling statistics) to the primary particle energy; and by measuring the lateral shower spread over a few anode strips, a centroid analysis gave the position of the primary to a few mm accuracy. These ideas are extensively described in references [48,49]

One cell of the LAC is displayed in Figure 19. It cell consisted of an a 3/16 inch lead cathode sheet, followed by a 1/16 inch copper-clad G-10 horizontal read out board, followed by a 1/16 inch copper-clad G-10 cathode board, and finally a 1/16 inch copper-clad G-10 vertical read out board. The cathode and anode boards were separated by 2 mm nylon spacers. The copper-clad G-10 boards measured 48 x 48 square inches. A total of 96 read out strips of 1/2 inch width were chemically etched onto each anode board (used vertically or horizontally). The anode strips were connected to charge sensing amplifiers located on top of the cryostat by strip lines. Two boards were placed abreast to form a 96 x 48 square inch plane (Figure 20). The lead cathodes were not continuous sheets but were 13 x 48 square inch sheets pinned together at the edges to form a 96 x 48 square inch cathode plane.

The 28 cells of the detector comprised 26.2 radiation lengths of material (23.2 Pb, 1.6 LA, .8 G-10), and 1.26 interaction lengths (.73 Pb, .23 LA, .30 G-10). The detector was longitudinally divided into a front and back half, each with 14 layers. The 14 anode strips longitudinally contiguous were analog summed to form 384 X read out and 384 Y read out channels.

A 4 1/2 inch diameter hole was placed in the detector center, to allow the passage of non-interacting beam. The hole was voided of liquid by a helium filled plastic cylinder kept under pressure. The argon was liquified and kept in that state by a LN_2 refrigeration system. The detector was placed in a foam insulated stainless steel box and held at a slight overpressure to minimize the back diffusion of impurity gas (O_2,,etc.). A cathode potential of -2.1 kV was placed on the front and back halves independently.

The 786 detector electronic channels were processed by a high rate amplifier and digitizer system developed at Fermilab [50]. A schematic is shown in Figure 21. The charge collected from each channel of the liquid argon calorimeter was integrated by a charge sensitive amplifier. The output was sampled at two points in time by a sample/hold capacitor system. The first sampling occurred right after the trigger and the second sampling occurred at the full pulse rise time of 300 nanoseconds. The difference in the samplings was proportional to the charge collected by that channel during the event. Channels that yielded charges above a selected threshold were digitized.

Each group of amplifier cards was tended by a scanner module. The scanner determined which channels had charged to values above the set threshold. When a signal over threshold was found, the analog difference was sent to a master control unit. The master controller digitized the analog difference and sent it and the channel address information to a 1K CAMAC buffer memory. The east and west channels on the LAC were digitized in parallel, each with it's own 1K CAMAC buffer memory.

Rear Muon Hodoscope and Dump

The remaining elements in the forward spectrometer were a final hadron absorber, a proportional tube hodoscope

(M4), and scintillation paddle array (M5) for measuring the positions of muons penetrating the dump, Figure 22. The steel filter measured 2.5 meters in depth and had a 20 x 20 square centimeter beam hole in the center for a noninteracting beam exit.

The two 64 channel proportional tube arrays (M4) were positioned to the left and right of the beam exit port. The tube counters consisted of a 3/4 inch (o.d.) aluminum tubes with a 1.2 mil Au-W wire strung down the center. Adjacent tubes were overlapped giving the hodoscope effective 1/2 inch resolution. The proportional tubes operated on a 7:3 argon-isobutane gas mixture at a anode potential of +3 kV with respect to the grounded tube cathodes. The anode wires were capacitively read out into Lecroy DC201 amplifier/discriminator hybrids. The discriminated outputs were driven to a dedicated CAMAC latching system built by Northwestern University for the purpose. The tube latches were set by a system trigger, and held until the computer read out cycle.

Positioned immediately in the rear of the proportional tube hodoscope was an 18 paddle scintillation hodoscope for measuring horizontal positions of penetrating particles. The individual paddles were 1 cm thick lucite paddles doped with scintillator; they measured 14.5 cm in width and 1.4 meters in length. The light output from each paddle was viewed by a 56DVP photomultiplier tube and discriminated at minimum ionizing levels. The 18 outputs of the hodoscope were stored in CAMAC coincidence latches on each trigger, awaiting read out.

E. Data Aquisition

The experimental data for the major part of the analysis was taken in the spring of 1981. Approximately two million muon triggers were logged, 30000 interaction triggers, and an additional number of diagnostic test triggers. The data was logged with a PDP11/45 computer and peripherals via CAMAC interfacing. The software package used for the data aquisition was an a version of RTMULTI, [51] developed at Fermilab. The data was written at high density (6250 bpi) to magnetic tape for later analysis.

Read Out

The data from all devices logged into the event record was transferred from the individual hardware devices and stored in some form of CAMAC memory device. These transfers were previously described. (In addition, some quantities were scaled on a "per spill" basis for diagnostic and beam flux normalization purposes. These scalar sums are listed in Table 10.) The data, now in the form of 16-bit words, was written to magnetic tape under PDP11/45 software control. A schematic of the computer read out system is shown in Figure 23 and described below.

All experimental triggers were first issued to a

Master Gate Unit. The MGU synchronized the read out sequence with the beam gate "on" and beam gate "off" signals from the accelerator timing unit. It issued an immediate fast deadtime block of one microsecond into the trigger in order to allow time for the computer to implement it's own deadtime control. A subsequent slow dead time could be issued if for any reason the computer deadtime needed to be augmented. In addition a read out abort could be issued at this time.

The MGU then signaled the bison interrupt box to issue a computer interrupt. The computer halted any analysis to begin the data read out cycle. Type a-interrupts were issued during beam spills for experimental triggers and type b-interrupts were issued between spills for diagnostic test data. The bison box computer busy output came on whenever an "a" or "b" event interrupt signal was received; it was not turned off until the read out cycle was completed and the computer was ready to accept the next trigger. The interrupt invoked the execution of the CAMAC "list", a list of computer instructions for data retrevial.

In parallel to the bison interrupt initializtions, the MGU gated on the CAMAC coincidence latches, ADC's, and scalars. The CAMAC interface units were enabled, allowing data to be transferred into the CAMAC buffer memories.

The CAMAC "list" was executed in sequence. When each device signaled that it had completed its data transfer into CAMAC area it was read out. The data was transferred to an event buffer and written to magnetic tape. At the end of execution of the CAMAC read out cycle all memories were cleared.

CHAPTER 3

Data Analysis

A. Muon Trigger Analysis

The subset of triggers containing muons that could be traced through the full trigger arm were extracted in the first pass over the data. Pattern recognition for this analysis involved the identification a charged particle track exiting the upper yoke of the spectrometer magnet and linking it to a track formed from the target interaction point and an M1-hodoscope coordinate. From the bend of the particle's trajectory in the polarized iron of the spectrometer magnet the charge and momentum of each fully reconstructed muon track was determined.

Tracking

Eight planes of multiwire proportional chambers (MWPC's) were used to track muons as they emerged from the spectrometer magnet. Figure 24 gives a view of the muon trigger arm including the muon hodoscopes and multiwire proportional chambers. Three horizontal planes (MUX1,MUX2,MUX3) and three vertical planes (MUY1,MUY2,MUY4) were used to define line segments in those views. Track segments were defined as a set of two or three hits fitting a straight line within estimated errors. After these horizontal (X) and vertical (Y) segments were determined, two planes of rotated wires, MUU3 and MUV4, were used to match the line segments from the X and Y views into three dimensional tracks. The transformation from the (x,y) grid into the rotated (u,v) system is,

$$u = x\cos(\theta) + y\sin(\theta)$$
$$v = x\cos(\theta) - y\sin(\theta)$$

where $\theta=15^{\circ}$, and the (x,y) values are the extrapolated positions at the rotated plane of interest. All X and Y segments were combined into trial three dimensional tracks, and extrapolated into the two rotated planes. If at least one rotated hit was recorded within predicted errors of the extrapolated position, the corresponding X,Y segments were recorded as a valid three dimensional track (3-D track).

Roading

All tracks were required to intersect the M2 and M3 hodoscope paddles that were latched in the event. These M2 and M3 hodoscope paddles defined an effective road that suppressed false tracks coming from delta-rays, bogus two point tracks, and charged particles scattering upwards from the forward spectrometer arm.

Multiple coulomb scattering in the material that resided between the M2 and M3 trigger paddles, and MWPC resolution caused ambiquities in defining the real intersection of a track with a trigger counter. A disagreement of one centimeter between a track paddle edge was allowed before rejecting a track. This value was determined by considering the track-counter displacement residuals for 2 and 3 point tracks extrapolated into the hodoscope planes, and estimating the maximum tolerable mismatch.

Upstream track

The M1 hodoscope provided the means for establishing the muon trajectory before entering the magnet. All x and y coordinate hits reported by the hodoscope were paired to form candidate (x,y) positions at M1. By connecting these coordinates with a point at the target center a set of trial upstream trajectories was formed. One candidate existed 70% of the time, with the balance coming from events recording multiple hits in the hodoscope. The higher multiplicity events were believed to be hadronic cascades ranging through the 1 meter absorber, or low momentum charged particles entering the hodoscope from below the hadron absorber.

Midplane match

Each 3-D track passing the tracking and roading phase was required to match at least one of the upstream target-M1 segments. The match was accomplished by extrapolating the upstream (target-M1) and downstream (MWPC) tracks to the spectrometer magnet midplane and using the displacement residual to define a chisquare.

$$\chi^2 = (\Delta X/\sigma_x)^2 + (\Delta Y/\sigma_y)^2$$

the quantities ΔX and ΔY indicate the midplane deviations for x and y extrapolations respectively and the errors, σ_x and σ_y, are the observed widths ($\sigma \simeq .05$m) of the residual distributions shown in Figure 25.

The upstream track that minimized this value of chisquare was picked as the best match to the downstream track in question. The r.m.s. width of the distributions is attributed to multiple coulomb scattering, MWPC resolution, and M1-hodoscope resolution. The x midplane matchup acquires an additional spread from the bending of the tracks in the x-z plane of the magnetic field. The resulting error was shown to be small (1-5 mm) for tracks accepted into the muon trigger arm.

Charge and Momentum Analysis

The charge and momentum of the matched tracks were determined by calculating the bend angle of the track in the polarized field of the spectrometer magnet return yoke. A first approximation to the momentum was given by,

$$P = \frac{q\ B_o\ L}{2\ \sin(\Theta/2)} + dE/dx \quad ,$$

where B_o is the average magnetic field strength in the yoke, L is distance traveled in the field, Θ is the bend angle, and dE/dx represents the average energy loss by ionization in the absorber (≃3.5 Gev).

The momentum determination was improved by using a least square fitting technique that took into account field variations in the magnetized yoke, multiple scattering, and energy loss in the hadron absorber. The MWPC track was projected into the magnet yoke and a numerical integration of the field equations (iterative swim) performed, using the first order momentum value given above as a starting value, and updating after each integration. The fit converged within 2 iterations, producing an optimized value of the momentum; only bounded by multiple coulomb scattering errors , $\sigma_\theta/\theta \simeq .17/P(\mathrm{GeV})$, and spectrometer angular resolution (≃15 mrdn.). A Monte Carlo simulation in which muons were propagated through the trigger arm at a known momentum, showed that the fractional momentum resolution upon reconstruction could be fit to the expression,

$$\sigma_P/P = .24 + .0015\ P\ , \quad 5\ \mathrm{GeV} < P < 50\ \mathrm{GeV}\ .$$

The particle charge was determined by its deflection in the magnetic field. Due to uncertainties in the bend angle this determination was less reliable at high momentum, where the angular resolution of the trigger arm dominates the error. Plotted in Figure 26 is a calculation of the charge determination efficiency versus muon momentum. The efficiency is very good over the range of muon momenta triggering the experiment. The momentum and transverse momentum spectra for triggering muons is shown in Figure 27.

Trigger Efficiency

The trigger efficiency for various processes was determined through Monte Carlo integration. The crucial ingredients of the muon trigger arm included in the simulation were: (1) multiple coulomb scattering through hadron filter, (2) ionization energy losses, (3) path integration through the spectrometer magnet return yoke, (4) trigger telescope and roading requirements, (5) MWPC tracking efficiencies, (6) wire position granularity, and (7) the muon reconstruction algorithm. The calculations assumed the muon trigger counters were 100% efficient in detecting charged particles. The simulations indicated that the trigger efficiency was essentially independent of muon production model and that the trigger efficiency could be factorized into an MWPC tracking efficiency and reconstruction efficiency. The three dimensional tracking efficiency for the muon arm MWPC's was about 92%, and the pattern recognition reconstruction efficiency for the Monte Carlo generated direct muon events was above 90% depending on the final pattern recognition cuts enforced. These will be specified in the next section.

Final Trigger Muon Cuts

After the first pass analysis was completed, additional cuts were applied to the exiting data sample alleviating known problems. (1) The magnet center residual cut was expected to be momentum dependent (multiple scattering 1/P influence) getting larger at lower momentum values. Figure 28 shows a scatter plot of the magnet center residual, $\Delta R = \Delta X^2 + \Delta Y^2$, versus measured muon momentum. Superimposed are functions, α/P, representing possible cut boundaries. The enforced value of $\alpha = 2.5$ was considered an upper bound on the cut. The estimated reconstruction efficiencies for the each value of α are indicated on the plot. (2) A few percent of all triggers were caused by halo muons. This halo component had a distinct signature: it entered the muon trigger arm from the beam right side or the top of the veto wall (at small angles with respect to the beamline). They were efficiently rejected by placing an X intercept cut on the MWPC track in conjunction with a vertical track slope cut. These distributions and cuts are indicated in Figure 29a and b. The results are shown in Figures 29c and d. (3) Finally, all muon tracks were required to have at least one MWPC hit behind the final segment of hadron absorber, as a final precautionary measure against triggers involving delta rays and hadron contamination. This cut introduced a 4% inefficiency into the reconstruction efficiency based soley on the efficiencies of the required MWPC's, MUY4 and MUV4. The data reduction up to this phase in the analysis is recorded in Table 11.

B. Forward Spectrometer

Hadron Tracking Pass

Charged particles emerging from the 40D48 magnet aperture were tracked by the multiwire proportional chambers and drift planes located in the forward spectrometer arm (Figure 1). The tracking of horizontal segments proceeded in a similar manner to the trigger muon tracking phase. A minimum of 4 of 6 hits were required on an X segment, 3 of 5 hits for a Y segment, and 1 of 3 rotated hits were required for a 3-dimensional match. The momentum and charge of each track was determined by its deflection in the 40D48 analyzing magnet. A momentum function, whose inputs were the slope and intercept of the deflected track and the interaction vertex point was developed for this purpose. The charged particle multipicity was approximately 7 tracks/event with a reconstruction efficiency of .70 for each 3-dimensional track. Figure 30 displays the momentum and transverse momentum distributions of the hadron arm tracks.

Cerenkov Analysis

The charged particle tracks were extrapolated into the Cerenkov counter for particle identification based upon light levels observed in the photomultiplier tube array. The pion, kaon, and proton thresholds for emitting Cerenkov light were at 6, 21, 40 GeV/c respectively. Between 6 and 21 GeV/c pions were identified as charged tracks giving light in one of the phototubes. Tracks showing no light were identified as kaons or protons. In a similar manner pions and kaons could be distinquished from protons in the momentum interval 21 to 40 GeV/c. For tracks whose Cerenkov light was expected to be shared by a phototube, a pion or kaon hypothesis was generated for each track. The observed light yield that best fit the particle assignment prescription was chosen as the best estimate of the particle identities. Approximately 15% of all reconstructed tracks were identifed as kaons.

C. Electromagnetic Shower and Electron Identification

Electrons traversing the forward spectrometer arm were identified in the Pb-LAr electromagnetic calorimeter shown in Figure 1. The detector was longitudinally divided into two halves each containing 14 radiation lengths and .6 interaction lengths of material. Both the horizontal (X) and vertical (Y) views were segmented into 96 X and 96 Y separate readout channels allowing a precise location of electron and photon positions in the detector. A description of the readout and of the detector construction is given in Chapter 2.

Electron Detection

A high energy electron entering the Pb-LAr lattice will induce an electromagnetic cascade within the first few radiation lengths of material encountered in its path. Bremsstrahlung for energetic electrons feeding pair production for energetic photons propagates the shower, until at low energies electron ionization processes dominate and quench the cascade. Electrons with energies below 50 GeV will deposit most of their energy in the first 14 radation lengths of the detector lattice (front half).

Hadrons interact in matter primarily through low energy electromagnetic ionization processes. The energy collected by the calorimeter in such a process is well below detector threshold, and goes unnoticed. But, hadrons undergoing strong interactions in the detector lattice can initiate an electromagnetic shower cascade, and be misidentified as electrons. With each detector half constituting .6 interaction lengths of material, an interaction will occur with 70% probability for each track entering the detector. The interaction will occur with nearly equal probability in depth. Some fraction of these interactions will produce energetic electrons or photons, and hence an electromagnetic shower. The major component of hadronically induced showers comes from neutral pion (π^o) production, and then the subsequent decay of the π^o into two energetic gamma rays,

$$\begin{array}{l} \pi + N \rightarrow \pi^o + X \\ \qquad\qquad\; \rightarrow \gamma + \gamma \end{array}$$

The energy deposition of an interacting particle covers the full momentum range of the primary, and is strongly dependent on the interacton location.

Hadrons showering in this manner provided an accidental background to the identification of electrons. By utilizing characteristic properties of electron/hadron showers and detector design the electron to hadron rejection can be increased by several orders of magnitude. Some properties are listed below:

Electron showers:

1. Electron showers begin in the first few radiation lengths of the detector and are more likely to be identified by the electromagnetic shower reconstruction programs.

2. Most of the electron energy is deposited in the front detector half, with slight leakage into the rear. The front to total energy collection fraction will approach unity. In addition, the total energy collection will approximate the electron momentum measured by the spectrometer.

3. The lateral shower profile for electrons is highly predictable and can be used extensively in identifying real electron induced cascades.

4. The shower propagates nearly along the electron direction and thus the shower centroid and electron intercept at the detector are highly correlated.

5. Showers are sampled in both the horizontal and vertical views, thus making two independent measurements of the electron energy. These energies should be nearly equal.

Hadronic showers:

6. Hadronic showers start with equal probability in depth, making pattern recognition difficult to impossible if the cascade begins longitudinally too far into the detector front half.

7. The longitudinal energy deposition is not expected to favor either the front or back detector lattice because of 6.

8. Characteristics of hadronic particle production will make the lateral shower profiles, centroids, and energy measurements more erratic on an event by event basis, opposing points 3-5 above.

Shower Shapes and Energy Calibration

The lateral shower profiles were established for electron showers by directing a 10, 20, and 30 Gev beam into the detector. The fraction of electrons at these beam momenta were in excess of 90%. A shower energy and centroid,

$$E = \sum_i (e_i) \quad , \quad i= 1, \text{no. strips in shower}$$

$$\langle x \rangle = \sum_i (x_i e_i) / E \quad ,$$

was found for each shower using the pulse heights, e_i, measured in the electronic channels containing the shower(s). A profile density function was generated by plotting the energy fraction in a strip versus displacement of the strip center from the shower centroid location. This shower shape density was fit to a functional form,

$$D(x,y) = \frac{a\ b}{a + B\ b} \left(e^{-a\ (x - y)} + B\ e^{-b\ (x - y)} \right)$$

x = position for shower amplitude evaluation
y = shower centroid location
a,b,B = fitted parameters

The above fitted parameters showed little energy dependence, with slight exceptions observed in the shower tail regions. Figure 31 shows the shower shape profiles for the X and Y views where the 10, 20, and 30 GeV data are combined. The X-view and Y-view shower shapes slightly differed and separate parameters were used for each.

The electron calibration data was also used to estimate the fraction of energy expected to be measured in the back detector half as a function of primary energy. The following parameterization of $F=E/E_{back}$ was extracted:

$$F^{u.b.} = 1.13 - .014\ E \qquad (1\ \text{GeV} < E < 5\ \text{GeV})$$

$$= .918 + .089\ \text{Log}(\ E\ ) \qquad (\ E > 5\ \text{GeV}\ ),$$

where the function gives the estimated upper bound (u.b.) to the ratio, $F=E/E_{back}$, and E is the total measured shower energy.

The shower energies used thus far have been been calculated by scaling the integrated pulse height in a shower to the known electron beam momentum. This corresponded to approximately 40 MeV per ADC count.

The shower calibration procedure was an iterative technique since many of the final results depended on initial approximations. The shower shape functions, back half energy parameterization and energy calibration were repeated after initial values were determined. A detailed explanation of these procedures is given by Sakumoto [52].

Shower Analysis

A search was made for electromagnetic (EM) showers in each detector view (X and Y) with a "peak and valley" algorithm [52]. Groups of adjacent channels exhibiting significant ADC counts over background were recorded as X or Y showers. Centroids and energies were determined for each identified shower. An X-Y energy matching algorithm next mated showers from each view, allowing for 1-1, 1-2, 1-3 matchups. Unmatched showers were dropped. The energies and centroids of the X-Y mated showers were refined by a chisquare optimization procedure, based upon the EM shower shapes. Such a minimization of observed shower shape to predicted shower shape reduced the effect of strip by strip statistical fluctuations, resulting in a better centroid and energy measurement. An average of 3 showers were reconstructed on each event with a typical energy of 6-10 GeV.

The shower analysis identified electromagnetic showers based upon matching their X and Y view energies, with some optimization relying on the lateral shower profile information. Hadron induced showers were naturally rejected at some level by the matching criteria, but further rejection was accomplished enforcing a series of EM shower cuts on the showers. The set of variables used to increase the electron identification efficiency are defined below. The distributions are plotted in Figure 32 for a data sample of muon triggered events with the placement of cuts indicated.

1. X-Y energy matchup chisquare before optimization:

$$\mathrm{CHISHWR} = (E_x - E_y)^2 / (\delta E_x^2 + \delta E_y^2)$$

2. X,Y shower shape chisquare:

$$\mathrm{XCHI,YCHI} = \mathrm{SUM}_i (E_i - E(x_i))^2 / (\delta E)^2$$

i summed over shower strips

E_i = energy in strip i

$E(x_i)$ = energy predicted in strip i by the shower shape density function.

3. X-Y energy asymmetry after optimization:

$$\mathrm{RMNT} = | E_x - E_y | / (1/2)(E_x + E_y)$$

4. Back half energy estimation:

$$\mathrm{FESHWR} = E / E_{back} < F^{u.b.}$$

Electron Identification

The electron identification involved two additional tests involving information from the charged particle tracks intersecting the calorimeter.

5. Associating EM showers with charged tracks by determining the distance of closest intersection, RADIUS ,between the shower centroid and charge track extrapolation. The distribution and cut are shown in Figure 32.

$$\mathrm{RADIUS} = [(x_{tk} - \langle x_{sh} \rangle)^2 + (y_{tk} - \langle y_{sh} \rangle)^2]^{1/2}$$

x_{tk}, y_{tk} = position of extrapolated tracks at shower detector

$\langle x_{sh} \rangle, \langle y_{sh} \rangle$ = shower centroids

6. Comparing the shower energy measured in the calorimeter with the momentum determined from the spectrometer analysis. The energy divided by momentum ratio, E/P, is shown in Figure 33 for electrons and positrons. The RADIUS cut and EM shower cuts have been applied.

   E/P = (calorimeter energy) / (track momentum)

The distributions show a peak at mean E/P values of about one, corresponding to electrons or positrons depositing all of their energy in the calorimeter. The spread of the peak about the mean is attributed to the energy resolution of the calorimeter, given by, $\sigma_E/E \simeq .22/E$. Also seen is the hadron background component falling from small E/P values and providing a background under the electron/positron signal. The response of the signal to background ratio in the E/P spectra is also demonstrated in Figure 33. Here RADIUS cuts of 1-3 centimeters are tried with and without the EM shower cuts. On an event by event basis electrons/positrons could be identified with charged tracks having an E/P within 2 standard deviations about E/P≃1.; with a hadron contamination of about 15% in the case of the 1cm RADIUS+EM cuts.

Fits to Signal and Background

Since the identification of an opposite signed μ-e excess involved a bulk analysis of the data, the background could be removed more reliably by fitting the E/P spectra to signal and background functions. Upon considering that the hadron background might enter the problem in an asymmetric manner, contributing differently to each sign of muon trigger, this procedure was felt to be the safest approach.

The number of electrons/positrons under the E/P peaks were determined by fitting the signal and background to a Gaussian and a polynomial function, respectively. These choices are motivated below. After the signal to background was determined for a 2 standard deviation window (2 σ) about the peak centroid, the ratio was scaled to the actual number of entries within the 2 sigma window for proper normalization; the chisquare fitting procedure not conserving the number of fitted entries.

The shape of the electron signal fit well to a Gaussian form,

$$S(E/P) = N\, e^{-.5(E/P-\langle E/P\rangle)^2 / \sigma^2}$$

The use of a simple Gaussian function was motivated by noting the E/P shape of a clear sample of electrons existing in the data, in the form of low mass e^+e^- pairs. Electron-positron pairs originating from gamma conversions and Dalitz decays were tagged by their characteristic low pair mass. Upon identifying an electron/positron in the shower detector, a search was made for an oppositely charged track forming a low invariant mass. No shower detector requirements were placed upon the second track. An additional opening angle cut was placed upon the pair, requiring that the tracks show a very small vertical separation after exiting the magnet; decay kinematics required that the opening angle be small and very little magnetic bending of the electron-positron trajectories occurred in the vertical plane. A plot of the e^+e^- invariant mass spectrum is shown in Figure 34, with the low mass cut was indicated at 25 MeV. The E/P spectra for low mass electron/positron pairs identified in the data sample are shown in Figure 35. These pairs were removed from the full E/P spectra before the least squares fitting was performed.

The E/P spectra for all positives and negatives depositing energy in the shower detector displayed different background shapes in the neighborhood of the electron/positron signal. This originated from a number of sources: (1) positive and negatives particles almost exclusively intercepted the west and east detector halves repectively; two virtually independent detectors,introducing systematic biases, (2) the species of secondary particles from $\pi^- N$ reactions is charge and momentum dependent, introducing further asymmetries in the accidental background. The only assumption made about the shape of the background was that it be a monotonically decreasing function of E/P, and decrease sharply for large values of E/P. A polynomial,

$$B(E/P) = a + b\, E/P + c\, (E/P)^2 + d\, (E/P)^{-1} ,$$

consistently gave good fits to the background based upon a chisquare per degree of freedom (CHI/DOF) assessment.

In order to further understand the systematic errors introduced in using the Gaussian and polynomial fit a test simulation was performed. E/P spectra were generated from known signal and background functions; and fit in a similar manner as the data. The fits indicated that the electron/positron signal could be extracted from the test spectra with fractional error (r.m.s.) of about 5%, and that this error could be reliably obtained from the correlated error matrix of the least squares fit. The above polynomial gave the best fits (CHI/DOF) to a variety of background functions tested.

D. Forward Muon Identification

Muons were identified by two banks of hodoscopes placed at the rear of a hadron absorber, shown in Figure 22. Secondary hadrons produced in each event were stopped in the 2.5 meters of steel upon initiating a hadronic shower. Muons and the high energy hadronic cascades penetrated. The horizontal muon position (X) was determined by an eighteen cell (.145 meter paddle width) hodoscope, M5, nine cells positioned on each side of the beam. The vertical positions (Y) were determined by a proportional tube array, M4, with .0254 meter cell size.

All charged particle tracks were extrapolated into the the M4 and M5 hodoscopes, and a displacement residual found for each track and the nearest paddle or tube center that registered a hit. On the condition that this deviation did not exceed predicted errors, the track was tagged as a muon. The track-counter residual distributions did not display a clear value at which to place the cuts. This was expected for the following reasons: (1) the large number of hadron tracks extrapolated into the muon hodoscopes obscured the real muon signal, (2) multiple coulomb scattering and its momentum dependence complicated the issue further.

A Monte Carlo simulation of the process was developed to study the window cuts. Muons of varying momentum were propagated through the spectrometer, scattering in the electromagnetic calorimeter and the rear dump. The residual between the extrapolated track position and actual particle position at the hodoscope was determined for a sample of events at each momentum. The r.m.s. deviation of the sample at each momentum was fit to a quadratic function of inverse momentum,

$$\sigma_x(P) = .0032 + .2858/P + 1.990/P^2 , \quad 5 \text{ GeV} < P < 50 \text{ GeV}$$

The window limit on the track-counter residuals in the data was taken to be the above modeled multiple scattering error added in quadrature to the hodoscope cell halfwidth. The Monte Carlo simulation indicated that this window was 90% efficient in identifying muons in each view. The residual test was made for both the horizontal and vertical hodoscope positions independently, with an identified muon requiring a confirmation from both searches windows (X AND Y).

A large source of accidental background mimicked real muons in the data. Strong focusing at the target caused the pion beam to diverge as it approached the rear of the spectrometer. A beam exit port was provided in the rear hadron dump for expelling the noninteracting beam and high momentum secondaries. Due to a readjustment of the beamline for the 1981 running period, the exit port was not properly aligned and scraping occurred. The hodoscope elements in the central region, near the beam port, recorded hits at abnormally high rates, indicating a beam particle or a fast secondary hadron interacting near the exit. In this central region the above mentioned muon algorithm was inefficient in distinguishing real muon tracks from track extrapolations that accidentally intersected uncorrelated hodoscope hits. The problem of accidental track-counter matchups occurred at some level in all hodoscope regions owing to the large number of forward arm tracks per interaction, the coarse resolution of the M5 hodoscope paddles, and some highly active proportionl tube counters.

The most direct way of assessing this accidental muon identification background was to make the assumption that the spectrometer tracks and muon hodoscope hits were uncorrelated if they occurred in different events. By using the hodoscope hits to identify muons whose tracks came from an uncorrelated event, the level of accidental identifications was determined. Table 12 gives the fraction of accidental muons identified in each M5 paddle. The problem becomes serious in the central region, and the center paddles were dropped from the analysis.

E. Muon-Lepton Charge Correlations

A double semileptonic decay of a charmed particle pair produces two leptons of opposite charge. In some fraction of these events a muon will trigger the apparatus and the second lepton will be detected in the forward spectrometer arm. The muon-electron events are a signature of charmed particle production. Dimuon events, detected in the same manner, will contain contributions from charmed particle decays and electromagnetic dimuon production. The following analysis involves two phases; (1) extraction of the prompt muon-electron excess from charmed particle decays, and (2) a similar extraction of the prompt dimuon signal. From (1) an estimate of the hadronic charmed particle production cross section times double branching ratio is made. The result from (2) is compared with a previous measurement of the dimuon yield in π-Be interactions at 150 GeV [41].

Determination of the Prompt Muon-electron Coincidence

The observed muon-electron (μ-e) yield can be expressed as a sum of individual contributions. In the following expression, the (T) indicates the muon is detected in the trigger arm, and the (F) indicates the electron is detected in the forward spectrometer arm.

$$N^{\mu e}_{obs} = \Sigma_{i,j} \; T^{\mu}_{i} \; F^{e}_{j} + N^{\mu e}_{accidentals} \qquad \text{(eq. 3-1)}$$

i : summed over all muon trigger processes
j : summed over all electron production processes

Four such expressions exist when the two charge states of the muon and two charge states of the electron are considered. The prompt and decay sources of trigger muons were discussed in Chapter 1 and are summarized in Tables 1,2, and 3.

Table 13 lists the major sources of prompt and nonprompt electrons. The dominant background to electrons from charmed particle decays comes from π^{o} and η Dalitz decays; and gamma conversions in the target. The target represents approximately .09 radiation lengths of material, converting a photon from π^{o} decays or other sources about 7% of the time. This provided the major electron background signal when compared to all other sources.

The detection of electrons from neutral and charged kaons, decaying in transit through the spectrometer, is suppressed by MWPC tracking constraints (vertical tracks must extrapolate into the target) and electron identification cuts (RADIUS and E/P cuts). The major sources of suppression for K_{e3} decays derives from decay kinematics; namely, a nontrivial electron decay angle with respect to the kaon direction and an energy degradation upon decay. A Monte Carlo evaluation of the pattern recognition efficiency for detecting K_{e3} decays in flight showed an electron reconstruction probability of .03% and .09% for $K^o \rightarrow e\pi\nu$ and $K^+ \rightarrow e\pi\nu$ per kaon, respectively. This number includes factors of (1) geometrical acceptance into the spectrometer and shower detector, (2) a MWPC tracking requirements (target point on the track in the Y view), and (3) RADIUS and E/P electron identification criteria in the shower detector. A similar evaluation for π^o's converting into e^+e^- pairs in the target gave a reconstruction probability per track of 8.5%. The ratio of K_{e3} to π^o conversions is estimated to be:

$$\frac{e_{K\rightarrow\pi\mu e}}{e_{\pi^\circ\rightarrow e\pm\gamma}} = \frac{\varepsilon_{rec}\ n_K(\text{no. kaons})\ B_e}{\varepsilon_{rec}\ n_{\pi^\circ}(\text{no. }\pi^o\text{'s})\ P_{conv}}$$

$$= \frac{.0009 \times 1/\text{event} \times .048}{.085 \times 3/\text{event} \times .15} \simeq .001$$

The average ratios of $\pi^o:\pi^\pm:K^\pm$ was chosen as 3:6:1 appealing to the identified charged particle ratios in the data set and assuming the number of neutral pions to be half the sum of charged pions on average. Based on this estimate and a similar background estimate for the neutral kaon, K_{e3} decays were not regarded as a serious background source.

The final term in eq. 3-1 is the observed accidental (acc) background from hadrons being misidentified as electrons in the shower detector. The contribution is removed by the E/P fitting procedure previously discussed. This term will include any systematic errors introduced at that point.

All electron sources, but weak decays of charm, will contribute symmetrically (production of an electron-positron pair) to the observed electron signal. Equation 3-1 can be separated into three component categories based upon electron origin: (1) prompt (p) μe's from charm, (2) electromagnetic sources (ee) of electrons detected in coincidence with a muon trigger, and (3) accidental (acc) sources.

$$N_{obs}^{\mu^{\mp},e^{\pm}} = f_{p}^{\mp\pm} n_{p}^{\mp\pm} + f_{ee}^{\mp\pm} n_{ee}^{\mp\pm} + N_{acc}^{\mp\pm} \qquad \text{(eq. 3-2)}$$

$$N_{obs}^{\mu^{\pm},e^{\pm}} = f_{ee}^{\pm\pm} n_{ee}^{\pm\pm} + N_{acc}^{\pm\pm} \qquad \text{(eq. 3-3)}$$

The variable (n) represents the number of mu-e events of a particular sign combination and type produced; and (f) represents the fraction of these detected. Note that the charm particle contribution to the same signed term is dropped, disregarding D^o-$\overline{D^o}$ mixing [53]. In order to isolate the double charm decay portion, the following equality is used:

$$n_{ee}^{++} = n_{ee}^{+-} = n_{ee}^{-+} = n_{ee}^{--}$$

These relations express the fact that the electromagnetic part of the prompt electron signal always leads to the production of a pair. (Implicitly assumed is that the trigger process is independent of the e^+e^- production mechanism, so that the equality extends over both trigger muon signs.) The opposite sign μ-e yield from charmed particle decays can then be isolated by subtracting a properly scaled same signed yield:

$$n_p^{+-} = [(N_{obs}^{+-} - N_{acc}^{+-}) - \alpha_{ee}^{+-}(N_{obs}^{--} - N_{acc}^{--})] \frac{1}{f_p^{+-}} \quad \text{(eq. 3-4)}$$

$$n_{p}^{-+} = [(N_{obs}^{-+} - N_{acc}^{-+}) - \alpha_{ee}^{-+}(N_{obs}^{++} - N_{acc}^{++})] \frac{1}{f_{p}^{-+}} \qquad \text{(eq. 3-5)}$$

$$\alpha_{ee}^{+-} = f_{ee}^{+-} / f_{ee}^{--} \qquad \alpha_{ee}^{-+} = f_{ee}^{-+} / f_{ee}^{++}$$

The constants (f), which represent the overall detection efficiency, include the factors of geometrical acceptance and detector efficiencies. Dropping references to sign combination and electromagnetic (ee) or prompt (p) category, the detected fraction (f) is given by:

$$f = \varepsilon_{trig} \, a_{mu} \, \varepsilon_{tk} \, \varepsilon_{lac} \, a_{el}$$

ε_{trig} = trigger efficiency

a_{mu} = trigger muon geometrical acceptance

ε_{tk} = forward spectrometer tracking efficiency

ε_{lac} = electron identification efficiency in the LAr calorimeter

a_{el} = electron geometrical acceptance

The constants α_{ee} represent any charge asymmetry introduced by the muon trigger in the detection of electrons or positrons (electromagnetic sources) by the forward spectrometer arm. If the above assumption, that $e^{\pm}$ pair production processes are independent of the trigger, equal numbers of low mass pairs should be found with each sign of muon trigger. As shown in the final chapter, the ratio of μ+/μ- triggers associated with low mass pair identifications is close to unity, but can only be tested to about 5% accuracy (due to the limited statistics). With that in mind, we assume that the constants are equal to unity, and discuss the consequences in the error analysis.

The final factors in eqs. 3-3 and 3-4 are the detection efficiencies for prompt μ-e events.

$$f_p^{+-} \quad \text{and} \quad f_p^{-+}$$

Acceptances were calculated in a Monte Carlo simulation of the spectrometer, using different models of charmed particle production. The factors of detector efficiencies also enters at this point in the calculation.

Electron/Positron Detection Efficiency

The shower detector's electron identification efficiency was determined from the sample of low mass elecron-positron pairs found in the data. Once a charged particle track was determined to be the second member of a low mass pair (Section C.) and accepted into the fiducial volume of the shower detector, the electron/positron identification was tested. The ratio of successful identifications to trials gave the efficiency for identifying positrons or electrons. Figure 36 shows the integrated efficiency as a function of the horizontal position (X) in the shower detector. In order to facilitate Monte Carlo simulations in the spectrometer an (X,Y) efficiency map was made for electron reconstruction, giving the electron reconstruction efficiency and associated error for each position in question.

A clear drop in detection efficiency is noted in the central region of the detector (Figure 36). A viable explanation was the high rate of neutral and charged particle intercepting the the calorimeter near the beam hole, introducing detection inefficiency. The calorimeter was positioned, not on the beam center line, but approximately 5 centimeters to the beam right. This allowed the charged beam, after receiving a .004 radian kick by the spectrometer magnet, to exit freely. The secondary neutrals produced in the target, not bending, intersected the calorimeter over a few strip region at center-left. The high momentum charged secondaries (beam fragments) concentrated to a lesser extent over the readout strips just beam-right. Rate effects, giving unreliable charge measurements for the X and Y collection strips in these regions, interfered with shower reconstruction, not only near the beam hole, but over the full shower detector. (Precise energy measurements were critical in the pattern recognition phase, matching X-Y shower energies.) This resulted in an overall loss in efficiency, and in particular, near the neutral beam region.

Muon-Electron Acceptance Calculations

The detector acceptance for triggering on a prompt muon from a charmed particle decay and detecting the forward electron from the associated state was estimated in a Monte Carlo simulation of the spectrometer.* Two central models of charmed particle production were tested. They are referred to as Model-A and Model-B.

In Model-A an associated charmed particle pair is produced from a phase space decay of a parent mass, M. The mass of the parent is generated in an exponential distribution function, e^{-5M}, with the mass threshold set above the generated two charmed particle masses($M > 2M_c$). The parent mass, M, is generated with a Feynman-X and transverse momentum (Pt) distribution in the pion-Be rest frame of,

$$\frac{d^2N}{dX_F\, dPt^2} = (1-X_F)^A\, e^{-B\, Pt}$$

The mass, M, is boosted into the lab frame and undergoes a two-body phase space decay into the two charmed particle state. The two charmed particles promptly decay by three body phase space criteria into $Ke\nu$ and $K\mu\nu$ systems. Although the model is not a standard approach, it is motivated by the need to include a dynamical correlation between the associated charmed particle pair being produced; dictated by our triggering and forward detection scheme. A similar, but more sophisticated, model is presented by [42] for the associated production of strange and charmed particles.

Model-B assumes the associated state is produced with statistical independence, so that an inclusive charmed particle model can be used for the muon decay and electron decay independently. The Feynman-X and Pt distribution of the charmed state is chosen from a factorized form,

$$E\,\frac{d^2N}{dX_F\, dPt^2} = (1-X_F)^A\, e^{-B\, Pt}$$

The results of the detector Monte Carlo simulations are given in Table 14. Various choices of the parameters A and B were used.

Determination of the Prompt Dimuon Signal

The determination of the prompt dimuon signal followed an analysis approach analogous to the method described earlier for the extraction of the prompt μ-e signal. Equations 3-1, 3-2, and 3-3 are directly applicable to the situation in which a muon triggers the apparatus and a second muon is detected in the forward spectrometer arm. The difference manifests itself in the different nature of the background to the dimuon signal; now from nonprompt decays of hadrons produced in the pion-Be interaction. The nonprompt background sources of muons are listed in Table 3. A difficulty arises in that no symmetry arguments can be made about the decay background, since the spectrum of produced hadrons will exhibit charge asymmetries on average. The equations are recast in the form:

$$N_{obs}^{\mu^{\mp}\mu^{\pm}} = f_{p}^{\mp\pm} n_{p}^{\mp\pm} + P_{d} f_{had}^{\mp\pm} n_{had}^{\mp\pm} + N_{acc}^{\mp\pm} \qquad \text{(eq. 3-6)}$$

$$N_{obs}^{\mu^{\pm}\mu^{\pm}} = f_{p}^{\pm\pm} n_{p}^{\pm\pm} + P_{d} f_{had}^{\pm\pm} n_{had}^{\pm\pm} + N_{acc}^{\pm\pm} \qquad \text{(eq. 3-7)}$$

The first term in the sum gives the number of prompt (p) muon coincidences detected; either from associated decays of charmed particles into a muon pair (Table 1) or an electromagnetic source of muon pairs (Table 2). The second term represents the contribution of nonprompt muons from hadron (h) decays into the forward spectrometer accompanied by a muon trigger. The term is weighted by the hadron decay probability, $P_d=1-e^{-x/\gamma c\tau}$; x being the available decay path. The final contribution comes from accidental (acc) track-counter matches discussed in Section **D.** of this chapter. The prompt term in eq. 3.5 (not occurring in eq. 3.2 for the muon-electron analysis) is included to indicate the possibility of a trigger muon from a charmed particle detected in coincidence with a muon from a dimuon source detected in the forward spectrometer. This occurence would be rare and is naturally taken care of in the background subtraction, contributing symmetrically to the forward muon yield, as in the muon-electron case. The term is dropped in the following analysis procedure.

As before, eqs. 4 and 5 are scaled and subtracted to isolate the prompt yields:

$$f_p^{\mp\pm}\, n_p^{\mp\pm} = (N_{obs}^{\mp\pm} - N_{acc}^{\mp\pm}) - r^{\mp}(N_{obs}^{\pm\pm} - N_{acc}^{\pm\pm}) - A^{\mp\pm} \qquad \text{(eq. 3-8)}$$

with the following definitions,

$$r^{\mp} = f^{\mp\pm}_{had} / f^{\pm\pm}_{had}, \qquad A^{\mp\pm} = P_d \, f^{\mp\pm}_{had} \, (n^{\mp\pm}_{had} - n^{\pm\pm}_{had})$$

The last term in the expression had a zero value in the muon-electron analysis from symmetry arguments, but here represents the hadron asymmetry (A) part of the calculation, as mentioned above. The last term is written out explicitly as,

$$A^{\mp\pm} = [\, a^{\mu\mp}_{trig} \, e^{\mu\mp}_{trig} \, a^{\mu\pm}_{H} \, e^{\mu\pm}_{tk} \, (n^{\mp\pm}_{had} - n^{\pm\pm}_{had}) \,] \, e^{\mu\pm}_{H} \, P_d$$

$$= [\, N^{\mu\mp h\pm}_{obs} - r^{\mp} \, N^{\mu\pm h\pm}_{obs} \,] \, e^{\mu\pm}_{H} \, P_d$$

The terms in the above equation are from left to right; trigger acceptance, trigger efficiency, forward muon hodoscope (H) detection efficiency, muon hodoscope acceptance, tracking efficiency, production asymmetry, and decay probability. The term in the brackets is reduced to a scaled difference in the indicated observed "trigger muon-forward hadron" yields observed in the data set.

The implied ratios r^{+} and r^{-} are correction factors for asymmetries introduced by the muon trigger arm with respect to the hadron background components. This ratio was taken from the data as being the observed muon-hadron ratio from the data set.

$$r^{\mp} = N_{OBS}^{\mu\mp h\pm} / N_{OBS}^{\mu\pm h\pm}$$

This choice of the scale factor forces the asymmetry term to zero.

The only missing quantities, (not addressed by Monte Carlo calculations), are the muon hodoscope detection efficiencies. These were determined from the data sample by predicting the muon flux incident upon the hodoscope from the hadron decay component of the background (like signed yields) and comparing this to observed yields of like signed μ-μ's.

$$e_{H}^{\mu\mp} = (N_{obs}^{\mu\mp\mu\mp} - N_{obs}^{\mu\mp\mu\mp}) / P_{d} N_{obs}^{\mu\mp h\mp}$$

An efficiency correction factor needed to be applied for hadrons which are tracked by the MWPC system, but decay in transit to the rear muon dump. This will introduce an inefficiency in the muon reconstruction algorithm due to possible nontrivial hadron-muon decay angles.

Approximately 90% of pions undergoing decays in this region are still reconstructed, but only 5% of kaon decays are still identified. The results are listed in Table 15.

A Monte Carlo evaluation of the spectrometer acceptance was performed, modeling the the dimuon production spectra from the Chicago-Princton results of reference [41]. The spectrometer acceptance for double charmed particle decays into muons was also tested with Model A, for double semileptonic charm particle decays. The results are listed in Table 16.

In order to take into account any variation of the above parameters with momentum, the calcultion of eq. 3-8 was performed as an integration over momentum bins, but in general the bulk analysis proved to agree with the momentum integration to within a few percent.

CHAPTER 4

Results and Conclusions

A. Results of the Dimuon Analysis

First we report the results of the dimuon analysis in which one of the muons is detected in the trigger arm (trigger muon) and the second is detected in the forward spectrometer arm (forward muon). This split has introduced an opening angle cut on the two muon system, and forced the acceptance of asymmetric dimuons pairs. These effects can be seen in the acceptance calculations of Table 16; resulting in a biased efficiency for higher mass states. It is for this reason that one could expect the dimuon yield to contain a large fraction of double semileptonic charmed particle decays. The mass resolution for dimuon pairs is poor, due to the multiple scattering limitations imposed by the muon trigger arm on momentum and angle measurements. The invariant mass spectrum for opposite signed and same signed pairs is shown in Figure 37.

Excess Dimuon Yield

The results of the momentum integration of eq. 3-8 are listed in Table 17 and Figure 38. The excess dimuon yield is sliced into bins of forward muon momentum. The yields in the table are corrected for efficiency factors in the forward spectrometer arm. A clear five standard deviation excess signal is measured, corresponding to a total dimuon production cross section (see Appendix 1) of,

$$\sigma_{\mu\mu} = 30.4(\pm 5.5)\ \mu b/\ \mathrm{Be\ Nucleus}\ ,$$

for π-Be interactions at $\sqrt{s}=19.4$ GeV. Anderson et al. [41] have measured dimuon production in π^{+}-Be interactions at $\sqrt{s}=16.8$GeV and report an integrated dimuon production cross section of, $\sigma_{\mu\mu}=10.0(\pm 1.1)\mu b$/Be Nucleus, for dimuon $X_F>0$. Assuming a symmetry about $X_F=0.$, thus doubling the Anderson result to attain a total cross section of about 20.0 μb/Be Nucleus; the two results are in reasonable agreement. Upon scaling the Anderson result to $\sqrt{s}=19.4$GeV, the two results may be brought into closer agreement.

J/ψ Cross Section

Table 18 and Figure 39 shows the excess yield sliced into bins of invariant mass. A slight excess of events is noted in the two mass bins covering the ψ particle mass (3.1GeV). This can also be seen in in Figure 37. In order to test for the possibility of a fluctuation, successive cuts were placed on the momentum of the forward muon. The results are listed in Table 19. The events in the ψ mass bins are stable to the momentum cuts, with most of the lower mass background diminishing, at the P_μ>22GeV level. Taking the events in the 2.5-3.5 GeV mass range to be 205±48 ψ particles (corrected yield), the resulting cross section times branching ratio into muons (details in Appendix 1) is,

$$\sigma_\psi \cdot B_{\mu\mu} = 156(\pm 39) \text{ nb/Be Nucleus}$$

Table 20 lists measured cross sections times branching ratios for ψ into muons at various $\surd s$ and nuclear targets. The references were chosen for compatibility with our experiment in both center of mass energy and nucleons in the targets (A). Extrapolating the cross sections into $\surd s$=19.4 GeV gives an estimated $\sigma_\psi \cdot B_{\mu\mu}$ of approximately 85.6±9.2 (x_F>0.) nb/Be Nucleus, with an $A^{.93}$ nuclear scaling approximation. The total cross section is expected to be less than twice the extrapolated result; ψ's being produced forward in the π-N center of mass system ($X_F \approx .2$ [55]). (Approximately 75% of the ψ production reported by [55] occurs in the forward hemisphere, implying an extrapolated total cross section of about 115 nb/Be Nucleus) The measured ψ yield thus agrees, within statistical accuracy and stated assumptions, to the expected production levels.

Dimuon Yield versus Trigger Muon Cuts

Although the dimuon signal potentially originates from both charmed particle and electromagnetic sources, it is interesting to investigate its dependence on the trigger muon kinematic variables, in the context of rejecting triggered events from hadron decays. The excess dimuon signal was binned as a function of trigger muon variables thought to hold rejection potential. These are listed below with explanation:

(1) Decay Probability. The decay probability for trigger muon was defined on page 27 of Chapter 1. It is the best estimate for assigning a track a pion decay weight. The gamma factor of the Lorentz boost was determined from the measured trigger muon momentum, and the free flight distance to the W-Fe absorber was estimated from the measured trajectory into the filter. One absorption length of W/Fe was added to the free flight path depending on the predicted muon entry point.

(2) Trigger Muon Momentum. Muon triggers from hadron decays are expected to diminish at higher values of momentum.

(3) Trigger Muon Transverse Momentum. Mean hadronic Pt's are lower than expected from charmed particle decays; thus lower Pt triggers have higher chance of originating from pion decays.

(4) Trigger Muon Vertical Angle. The vertical muon angle in the laboratory might favor decays of massive states.

(5) X-midplane Residual. Decay-in-flight triggers could potentially have poorer midplane matchups.

The results of the cuts are listed in Table 21. The most striking feature is the dependence of all cuts on the trigger muon momentum. (1) The yield versus "Decay Probability" decreases smoothly with higher decay probabilities. (2) The "Momentum" cut is most striking in that very little excess dimuon yield exists below trigger muon momenta of 6 GeV; the trigger region being dominated by hadron decays. (3) The excess yield versus "Pt" has the property of a gradual increase with higher trigger muon Pt's; the trigger bias for higher mass dimuon states (charm or electromagnetic) correlates directly with higher Pt triggers. (4) Little sensitivity is noted with the "Vertical Angle" cut. (5) Finally, the excess favors smaller "Midplane Residuals"; which can be construed to be an inverse momentum cut (considering the inverse momentum dependence of multiple scattering errors.)

B. Results of the Muon-Electron Analysis

Although an excess dimuon signal was seen in the previous analysis, it did not provide a measurement of the charmed particle decay yields. This issue is directly addressed by measuring the excess opposite signed yield of muon-electron coincidences in the data sample. The results are presented below.

Excess Muon-Electron Yields from E/P Fits

The results of the least squares fit to the total data sample is shown in Figure 40 and listed in Table 22. A calculation of the raw opposite sign μ-e excesses are shown at the bottom of the table. They follow directly from eqs. 3-4 and 3-5 of Chapter 3. The α_{ee} muon asymmetry parameters were calculated from the identified pairs in the data sample as previously discussed. As recognized in the table, it was only possible to establish the trigger arm asymmetry ratio to about 5% accuracy; statistics bound. The error to the Gaussian signal function was determined by standard error propagation techniques, utilizing the correlation error matrix of the resulting fit. The identified electron/positron pairs were removed from the E/P spectra before fitting.

The raw yields were each corrected for acceptance and detector efficiencies (Table 14) before being combined into a total corrected yield. Care was taken in the Monte Carlo calculations of Table 14 to account for asymmetries in acceptance and detector efficiencies with both positive and negative triggers. The efficiencies recorded in the table were derived from efficiency maps made for the MWPC's and shower detector, and represent mean efficiencies averaged over the ensemble of accepted tracks.

Even though the trigger arm, and to a lesser extent, the forward spectrometer were sensitive to the charmed particle production models tried; the integrated μ-e acceptances remained relatively insensitive to changes in the X_F and Pt distributions (Table 14). Model A (a=3. b=1.) was chosen as the test model for calculating a total charmed particle production cross section, bearing in mind the 10%-20% variations listed in the table for other choices. The calculaton (Appendix 1) results in the following μ-e total cross sections.

$$\sigma^{\mu+e-} = 1.25(\pm.36)\ \mu b/\mathrm{Be\ Nucleus}$$

$$\sigma^{\mu-e+} = .41(\pm.39)\ \mu b/\mathrm{Be\ Nucleus}$$

They are listed separately, in order to reflect on the possibility that the two yields may originate from different fundamental processes. Bodek et al. [36] have reported a 2:1 $\mu-/\mu+$ direct muon ratio in π^-Fe interactions for $X_F>.2$. They propose that a beam fragmentation process, preferentially forming a $D^- \bar{D}^o$system, results in a negative muon dominance (due to the favored charged D-meson semileptonic branching ratio). It would be difficult to extend these target fragmentation ideas to lower Feynman X regions, which dominate our electron sample. A more plausible explanation might be found in asymmetric detector efficiencies, and other sources of systematic errors, that are not recoverable in the efficiency correction procedure of the raw yields.

Table 23 lists the results of the E/P fitting analysis conditioned on a sample of cuts placed upon the trigger muon and forward electron. The cuts on the trigger muon momentum and decay probability, which seemed to work well in dimuon analysis, produced slight effect. The response to the RADIUS cut (electron track-shower centroid residual) was also ineffective in enhancing the signal to background ratios. These responses are understandable upon considering that conversion electrons are the major source background, and the above mentioned cuts are basically hadron effective. The final entries into the table give the raw excess yields sliced into electron momentum and Pt bins. The statistical significance assigned to each bin is poor, hampering any real understanding of the kinematic distributions, in terms of Monte Carlo models used.

An estimate of the total charmed particle production cross section follows from the relation,

$$\sigma_{cc} \cdot B_{\mu} \cdot B_{e} = 1/2(\sigma^{\mu+e-} + \sigma^{\mu-e+})$$

We further assume that the excess signal is dominated by associated D-$\bar{D}$ production, and take the mean semileptonic branching ratio of 8(±1.3)% from $e^{+}e^{-}$ annihilations [24]. Under these assumptions the total charmed particle production cross section was measured to be:

$$\begin{aligned} \sigma_{cc} &= 123.(\pm 35.)\ \mu b/\text{Be Nucleus} \\ &= 13.7(\pm 4.0)\ \mu b/\text{Nucleon} \quad (A^{1.}\ \text{dependence}) \end{aligned}$$

The quoted error is purely statistical.

C. Discussion of Errors

The stated errors in the calculations, thus far, have been totally statistical in nature, and propagated with standard error analysis techniques. The statistical significance of the excess opposite signed μ-e events is not only limited by the total number of events in the data sample, but by our ability to reject electrons/positrons from conversions and Dalitz decays in the sample. Electrons from kaon decays were estimated to contribute at the .1% level (pg. 90) relative to conversion electrons, and corrections were not considered in the above calculations. The serious problem of charge correlations between the trigger muon and forward misidentified hadrons, did not materialize; attributed to the good hadron background rejection in the electron identification procedure. In addition the polynomial fits to the background generally estimated approximately equal numbers of accidental hadrons under the electron and positron signals, regardless of trigger muon sign.

Although attempts were made to keep sources of systematic errors at a minimum, they enter into all measurements in complicated ways. We estimate the major systematic errors and report them separately. The three major sources come from, (1) an approximate 10% inaccuracy in the beam normalization as discussed on page 34, (2) measured errors in the mean semileptonic branching ratio used (19%), and (3) the modeled acceptance of the spectrometer, estimated to contribute at the 10-20% level. Added in quadrature, they are contributing at the 30% level to our measurement of the total charmed particle production cross section.

D. Conclusions

We have measured the total charmed particle production cross section in 200 GeV/c pion-Beryllium collisions. The measured production cross section of 14(±4±5) μb/nucleon is in reasonable agreement with previous estimates discussed in Chapter 1; although all measurements to date are plagued by large errors. If high mass particle searches in hadronic interactions are to result in a fundamental test of the underlying physical processes, experiments with higher sensitivity will have to be carefully planned and performed. The problems plaguing, even second generation hadronic charm searches, are expected to multiply in the coming high energy accelerator regime, creating a great challenge to future experimenters.

REFERENCES

[1] J.J. Aubert et al., Phys. Rev. Lett. 33 , 1404 (1974).

[2] J.E. Augustin et al., Phys. Rev. Lett. 33 , 1406 (1974).

[3] G.Goldhaber et al., Phys. Rev. Lett. 33 , 255 (1976).

[4] E.Burhop et al., Phys. Lett. 65B , 299(1976).

[5] P.Bloch, Proceedings International Symposium on Lepton and Photon Interactions at High Energies, Hamburg, ed. F.Gutbrod, Aug.25-31,1977, 293(1977).

[6] D.Aston et al., Phys. Lett. 94B , 113 (1980).

[7] B.J.Bjorken, S.Glashow, Phys. Lett. 11 , 225 (1964).

[8] Y.Hara, Phys. Rev. B134 , 701 (1964).

[9] S.Glashow, J. Iliopoulos, L.Maiani, Phys. Rev. D2 , 1285 (1970).

[10] N.Cabibbo, Phys. Rev. Lett. 10 , 531 (1963).

[11] D.C.Cundy, 1974 Proc XVII Int Conf on HEP London,July 1974 (Didcot,Berks:Science Research Counsel) IV-131 - IV-148.

[12] S.Weinberg, Phys. Rev. Lett., 19 , 1264 (1967).

[13] A.Salam, in Elementary Particle Theory, ed. N.Svartholm (Almquist and Wiksell,Stockholm,1965) p367

[14] S.Herb et al., Phys. Rev. Lett. 39, 212 (1977).

[15] M.L.,Perl, et al., Phys. Rev. Lett. 35 , 1489 (1975).

[16] G.Feldman, M.Perl, Phys. Rep. 33C , 286 (1977).

[17] M.K.Gaillard, B.W.Lee, J.L.Rosner, Rev. Mod. Phys. 47 , 277 (1975).

[18] N.Cabibbo, L.Maiani, Phys. Lett. 79B , 109 (1978).

[19] N.Cabibbo, G.Corbo, L.Maiani, Nucl. Phys. B155 , 93 (1979).

[20] J.Ellis, M.Gaillard, D.Nanopoulos, Nucl. Phys. B100, 313 (1975).

[21] A.Pais, S.B.Treiman, Phys. Rev. D15 , 2529 (1977).

[22] J.Brau, Proceeding of the Summer Institute on Particle Physics, SLAC Report 245, 441 (1982).

[23] R.H.Schindler, et al., Phys. Rev. D24 , 78 (1981).

[24] W.Bacino, et al., Phys. Rev. Lett. 43 , 1073 (1979); W.Bacino, et al., Phys. Rev. Lett. 45 , 329 (1980).

[25] H.Fritzsch, P.Minkowki, Phys Lett 90B , 455 (1980).

[26] M.Bander, D.Silverman, A.Soni, Phys. Rev. Lett. 44, 7 (1980).

[27] B.Guberina, S.Nussinov, R.D.Peccei, R.Ruckl, Phys. Lett. 89B , 111 (1979).

[28] W.Marciano, H.Pagels, Phys. Rep. 36C , 137 (1978).

[29] B.L.Combridge, XVIIth Rencontre de Moriond, Les Aves, France, January 24-30, 1982.

[30] M.Gluck, J.F.Owens, E.Reya, Phys. Rev. D17 , 2324 (1978).

[31] C.A.Heusch, SLAC Pub. 2876 , 195 (1981).

[32] C.E.Carlson, R.Suaya, Phys. Rev. D18 , 760 (1978).

[33] B.L.Combridge, Nucl. Phys. B151 , 59 (1978).

[34] S.Brodsky, et al, Phys. Lett. 93B , 451 (1980), talk given at the Moriond Workshop on New Flavors.

[35] V.Barger, F.Halzen, W.Y.Keung, Phys. Rev. D25 , 112 (1982).

[36] A. Bodek et al., Univ. of Rochester Report-830, (1982). C00-3065-338(1982)

[38] V.L.Fitch et al., Phys. Rev. Lett. 46 , 761 (1981).

[39] C.Daum et el., Conf. on High Energy Physics, Paris (1982), talk presented by the ACCMOR collaboration.

[40] "Review of Particle Properties", Particle Data Group, LBL-100 Revised, UC-34d, April 1982.

[41] Anderson et al., Phys. Rev. Lett. 37 , 799 (1976).

[42] M.Bourguin, J.M.Gaillard, Nucl. Phys. B114, 334 (1976).

[43] W.F.Baker et. al., Fermilab 78/79-EXP.

[44] see "Fermilab Experimental Areas Control System Computer User's Manual", (1974).

[45] C.R. Kerns, A High Rate Phototube Base, TM-640 2100.00.

[46] F.Sauli, "Principles of Operation of Multiwire Proportional and Drift Chambers", CERN 77-09 (1977).

[47] D.R.Green, Nucl. Instr. and Meth. 158 , 249 (1979).

[48] W.J. Willis, V. Radeka, Nucl. Instr. and Meth. 120 , 221 (1974).

[49] J. Engler, et al., Nucl. Instr. and Meth. 120 , 157 (1974).

[50] T.F.Droege, F.Lobkowicz, Y.Fukushima, IEEE Trans. on Nucl. Sci. 25 , 687 (1978).

[51] L.Taff, D.Ritchie, T.Lagerlund, RTMULTI Data Aquisition System, PN-110.1K.

[52] Northwestern University, Ph.D. Thesis of Willis K. Sakumoto, in preparation.

[53] A.Bodek et al., University of Rochester report C00-3065-315.

[54] J.G.Branson et al., Phys. Rev. Lett. 38 , 1331 (1977).

[55] M.A.Abolins et al., Phys. Lett. 82B , 145 (1979).

[56] E.Anassontzis et al., Fermilab-Conf-82/49-EXP 7550.537.

[57] A.S.Carroll et al., Phys. Lett. 80B, 319 (1979).

Appendix 1

A. Determination of Cross Sections

The total cross sections for the various processes considered in our work were calculated from the following thin target approximation:

$$\begin{aligned}\Delta I/I_o &= (\rho N_A \sigma/A)\ \Delta x_{tgt}\ \varepsilon \\ &= (\rho N_A \sigma_{inel}/A)\ \Delta x_{tgt}\ (\sigma/\sigma_{inel})\ \varepsilon \\ &= (\%\ tgt)\ (\sigma/\sigma_{inel})\ \varepsilon\end{aligned}$$

ρ = Be target density = 1.85 g/cm^3

N_A = Avogadro's number = 6.02 x10^{23} mole^{-1}

A = atomic weight of Be = 9.01

ΔI = measured yield of events from the process in question.

I_o = integrated beam on target, corrected for spectrometer deadtime (Table 10, scalar 7) and corrected for double beam occupancy, (pg. 33).
= 1.2 x (1.75 x10^{11})

σ_{inel} = inelastic cross section for 200 GeV π-Be interactions [57].
= 139 mb/ Be Nucleus

ε = detection efficiency for the measured process.
=(detector efficiencies) x (integrated acceptance)

Solving for the measured cross section, σ, we have:

$$\sigma = (I_o \ \%tgt)^{-1} \times (\Delta I/\varepsilon) \times \sigma_{inel}$$
$$= 9.24 \times 10^{-11} (\Delta I/\varepsilon) \sigma_{inel}$$

Total Dimuon Cross Section

The total measured cross section for the production of dimuons was derived from the values of measured yields listed in Table 17. This total yield was corrected for detector efficiencies in the forward spectrometer arm, previously. Table 18 gives the integrated acceptances and efficiencies in the muon trigger arm. An additional 95% muon pattern recognition efficiency (pg. 67-68) was imposed. Errors contributing to the calculation at a level of less than 1% are not included.

$$\sigma_{\mu\mu} = 9.24 \times 10^{-11} (\Delta I_{\mu\mu} / \varepsilon) \sigma_{inel}$$
$$= 9.24\times 10^{-11} [(3892 \pm 703)/(.95 \ .92 \ .0019)] \sigma_{inel}$$
$$= 2.16(\pm .39) \times 10^{-4} \sigma_{inel}$$
$$= 30.0(\pm 5.4) \ \mu b/\text{Be Nucleus}$$

$$\varepsilon = \varepsilon_{\mu rec} \ \varepsilon_{\mu pwc} \ a_{\mu\mu}$$

J/ψ Cross Section

The measured yield of ψ particles in the mass range from 2.5-3.5 GeV was converted to a cross section times branching ratio in a similar manner (Tables 16 and 18) used.

$$\begin{aligned}\sigma_{\psi}\cdot B_{\mu\mu} &= 9.24\ \mathrm{x}10^{-11}\ (\ \Delta I_{\psi\to\mu\mu}\ /\ \varepsilon\ )\ \ \sigma_{inel}\\ &= 9.24\mathrm{x}10^{-11}[(205\pm48)/(.95\ .92\ .0194)]\sigma_{inel}\\ &= 1.12(\pm.26)\ \mathrm{x}10^{-6}\ \sigma_{inel}\\ &= 154(\pm39)\ \mathrm{nb/Be\ Nucleus}\end{aligned}$$

$$\varepsilon = e_{\mu rec}\ \varepsilon_{\mu pwc}\ \alpha_{\psi\to\mu\mu}$$

Muon-Electron Cross Section

The excess opposite signed yield of μ-e events was converted to a total cross section from the information in Tables 14 and 22. The calculation is shown below:

$$\begin{aligned}\sigma^{\mu+e-} &= 9.24\mathrm{x}10^{-11}\ (\ \Delta I_{\mu+e-}\ /\ \varepsilon\ )\ \sigma_{inel}\\ &= 9.24\mathrm{x}10^{-11}\ \frac{284\pm83\quad 139\ \mathrm{mb/Be\ Nucleus}}{.95\ .94\ .68\ .56\pm.02\ .0087}\\ &= 1.24\pm.36\ \mu\mathrm{b/Be\ Nucleus}\end{aligned}$$

$$\sigma^{\mu^- e^+} = 9.24\text{x}10^{-11} \; (\, \Delta I_{\mu^- e^+} / \, \varepsilon \,) \; \sigma_{inel}$$

$$= 9.24\text{x}10^{-11} \; \frac{67 \pm 64 \quad 139 \text{ mb/Be Nucleus}}{.95 \;\; .93 \;\; .65 \;\; .45 \pm .02 \;\; .0083}$$

$$= \; .41 \pm .39 \; \mu\text{b/Be Nucleus}$$

$$\varepsilon = \varepsilon_{\mu rec} \; \varepsilon_{\mu pwc} \; \varepsilon_{epwc} \; \varepsilon_{lac} \; a_{\mu e}$$

Table 1. Prompt sources of muons from weak decays of charmed particles. The mean decay lengths for all decays are tens of microns. The lifetimes are from [40] and the branching ratios from [23,24].

Particle	Lifetime (10^{-13}sec.)	Decay Mode	Branching Ratio
$D^{\pm}$	$9.1^{+2.2}_{-1.5}$	$K(K^{*})\mu\nu$	$16.\pm6.4\%$ $22.^{+4.4}_{-2.2}\%$
D^{0}	$4.8^{+2.4}_{-1.5}$	$K(K^{*})\mu\nu$	$5.5\pm3.7\%$ $< 4.\%$
$F^{\pm}$	$2.2^{+2.5}_{-1.1}$	$X\mu\nu$	??
Λ_{c}	$1.1^{+0.9}_{-0.4}$	$X\mu\nu$	$4.5\pm1.7\%$

Table 2. Electromagnetic sources of prompt muons from vector meson decays and photon continuum. The data is from [41], for π^- Be interactions at $\sqrt{s}=16.8$ GeV. The cross section times branching ratio is given in nanobarns per nucleon. The A-dependence (atomic number) for scaling the cross section is indicated in the fourth column.

Mass(Gev) (GeV)	Particle	$\sigma \cdot B_{\mu\mu}$ (nb/N)	A^α
.21-.45	continuum	1250±500	$\alpha= .67$
.45-.65	continuum	370±130	
.65-.93	$\rho-\omega$	370±110	
	continuum	160±50	
.93-1.13	ϕ	70±21	
	continuum	21±6	
1.3-2.0	continuum	10±6	$\alpha= .85$
2.7-3.5	ψ	6.5±2.2	$\alpha=1.$

Table 3. Non-prompt sources of muons from the weak decays of hadrons. The data is from reference [40]. Hyperon sources are not included due to their small overall contribution.

Particle	cτ(cm)	Decay Mode	Branching Ratio
$\pi^{\pm}$	780.4	$\mu\nu$	100.%
$K^{\pm}$	370.9	$\mu\nu$	63.5%
		$\mu\nu\pi^{o}$	3.2%
$K^{o}{}_{l}$	1554.	$\pi\mu\nu$	26.8%

Table 4. E515 beamline elements.

Element Code	Z Position (ft.)	Description
TARGET	-5.00	MESON TARGET
QUAD 1	56.400	3Q120 1/2 QUAD
QUAD 2	67.463	3Q120 1/2 QUAD
QUAD 3	78.534	3Q120 1/2 QUAD
SEPT 1	89.979	3-2-123 SEPTUM DIPOLE
SEPT 2	101.469	3-2-123 SEPTUM DIPOLE
QUAD 4	112.919	3Q120 1/2 QUAD
QUAD 5	123.994	3Q120 1/2 QUAD
SEPT 3	135.462	3-2-123 SEPTUM DIPOLE
SEPT 4	146.920	3-2-123 SEPTUM DIPOLE
SEPT 5	158.391	3-2-123 SEPTUM DIPOLE
STOP	168.2	BEAM STOP
BEND 6	182.752	4-2-240 DIPOLE
BEND 7	204.000	4-2-240 DIPOLE
BEND 8	225.246	4-2-240 DIPOLE
COLL	239.500	HORIZONTAL COLLIMATOR
TRIM	245.000	VERTICAL VERNIER
QUAD 6A	249.936	3Q60 QUAD
QUAD 6B	256.431	3Q60 QUAD
COLL	263.200	HORIZONTAL COLLIMATOR
QUAD 8A	403.673	3Q84 QUAD
QUAD 8B	413.552	3Q84 QUAD
QUAD 8C	403.673	3Q84 QUAD
TRIM	424.000	VERTICAL VERNIER
COLL	443.000	HORIZONTAL COLLIMATOR
COLL	448.3	VERTICAL COLLIMATOR
MON	451.5	PROFILE MONITOR
QUAD 9	533.011	3Q120 QUAD
QUAD 10	564.986	3Q120 QUAD
COLL	651.9	VERTICAL COLLIMATOR
COLL	657.2	HORIZONTAL COLLIMATOR
TRIM	666.2	VERTICAL VERNIER
BEND 9	679.898	4-2-240 DIPOLE
BEND 10	701.080	4-2-240 DIPOLE
BEND 11	722.271	4-2-240 DIPOLE
BEND 12	743.499	4-2-240 DIPOLE
QUAD 11	761.415	3Q120 QUAD
QUAD 12	772.822	3Q120 QUAD
QUAD 13	790.830	3Q120 QUAD
QUAD 14	802.296	3Q120 QUAD

Table 4. E515 beamline elements (continued).

Element Code	Z Position (ft.)	Description
MON	883.4	PROFILE MONITOR
COLL	886.1	HORIZONTAL COLLIMATOR
TRIM	917.9	VERTICAL VERNIER
QUAD 15	960.45	3Q120 QUAD
QUAD 16	971.916	3Q120 QUAD
QUAD 17	989.691	3Q120 QUAD
QUAD 18	1001.157	3Q120 QUAD
MON	1050.0	PROFILE MONITOR
MON	1051.0	PROFILE MONITOR
QUAD 19	1180.236	3Q120 QUAD
QUAD 20	1194.903	3Q120 QUAD
QUAD 21	1206.307	3Q120 QUAD
QUAD 22	1220.957	3Q120 QUAD
TRIM	1229.3	VERTICAL VERNIER
TRIM	1233.2	HORIZONTAL VERNIER
MON	1437.5	SWIC
BEND 14	1495.0	5-15-120 EPB DIPOLE
QUAD 23	1563.7	4Q-120 QUAD
QUAD 24	1579.7	4Q-120 QUAD
TRIM	1583.7	VERTICAL VERNIER
MON	1613.5	SWIC
TARGET	1614.550	E515 TARGET
BEND 15	1620.630	40D48 DIPOLE

Table 5. Beam chambers.

Name	z position (m)	Active Area (m x m)	Sense Wires (no.)	Wire Spacing (m)
BMX0	-8.684	.128x.075	128	.00105
BMX1	-5.806	.128x.075	128	.00105
BMX2	-3.662	.128x.075	128	.00105
TGT	-2.45			

anode wire type:	Au-W
anode wire dia.:	.8 mil
anode-cathode spacing:	187.5 mil
cathode type:	Foil
gas mixture:	Magic gas
cathode potential:	-5 Kv

Table 6. Elements of the muon trigger telescope.

Counter	x_{mid}	y_{lo}	z	no. of cells	cell size (cm cm cm)
B1	0.	.0725	-2.50	1	(11.x.2x.16)
B2	0.	.0765	-2.50	1	(11.x.2x.16)
M0	0.	.0884	-2.23	1	(30.x4.x.32)
M00	0.	.0980	-2.00	1	(50.x10.x.32)
M1-X	0.	.1400	-1.43	14	(3.x13.x.16)
M1-Y(-)	-.076	.1400	-1.46	6	(13.x3.x.16)
M1-Y(+)	.076	.1400	-1.46	6	(13.x3.x.16)
M2	0.	.24	.66	4	(35.6x40.6x.32)
M3	0.	.34	3.55	6	(35.6x50.8x.32)

(x_{mid} = x position of hodoscope center.)
(y_{mid} = y position of hodoscope lower edge.)

Table 7. Trigger arm multiwire proportional chambers.

Name	Position (m)	Active Area (m x m)	Sense Wires (no.)	Wire Spacing (m)
MUX1	1.684	1.54 x.48	256	.006
MUY1	1.769	1.54 x.48	80	.006
MUX2	2.040	1.54 x.48	256	.006
MUY2	2.125	1.54 x.48	80	.006
MUX3	2.870	2.40 x.67	400	.006
MUU3	2.960	2.40 x.67	384	.006
MUY4	3.625	2.40 x.67	112	.006
MUV4	3.706	2.40 x.67	384	.006

anode wire type: Au-W
anode wire dia.: 1.115 mil
anode-cathode spacing: 250 mil
cathode wire type: Au-W
cathode wire dia.: 3. mil
gas mixture: Ar-ISO (7:3)
cathode potential: -(3.-3.5)Kv

Table 8. Medium aperture multiwire proportional chambers in the forward spectrometer arm.

Name	Position (m)	Active Area (m x m)	Sense Wires (no.)	Wire Spacing (m)
TGT	-2.45			
UPMY	-1.205	1.05 x.42	415	.001
UPMX	-1.151	.58 x.37	575	.001
DNMX	1.199	1.05 x.52	520	.002
DNMY	1.254	1.05 x.42	415	.001
DNMW	1.309	1.05 x.45	465	.002

anode wire type:	Au-W
anode wire dia.:	.8 mil
anode-cathode spacing:	187.5 mil
cathode type:	Al foil
gas mixture:	Magic gas
cathode potential:	-5 Kv (1mm wrsp) -3 Kv (2mm wrsp)

Table 9. Large aperture multiwire proportional chambers. located in the forward spectrometer.

Name	Position (m)	Active Area (m x m)	Sense Wires (no.)	Wire Spacing (m)
TGT	-2.45			
DNX1	2.255	2.32 x1.1	1160	.002
DNY1	2.443	2.65 x.76	380	.002
DNW1	2.606	2.65 x1.1	1065	.002
DNW2	4.263	2.65 x1.1	1070	.002
DNX2	4.394	2.65 x1.1	1060	.002
DNY2	4.842	2.65 x1.0	500	.002
DNX3	4.930	2.65 x1.1	1060	.002

anode wire type: Au-W
anode wire dia.: 1.0 mil
anode-cathode spacing: 250 mil
cathode wire type: Au-W
cathode wire dia.: 3. mil
gas mixture: $Ar-CO_2$ (9:1)
cathode potential: -(3.-4.)Kv

Table 10. List of summed scalar quantities.

Scalar Number	Inhibit (DT or UDT)	Description
1	$\mathrm{DT}=\overline{\mathrm{BEAM}}\cdot\mathrm{SUS}\cdot\mathrm{CDT}$	M
2	DT	M3
3	DT	M2
4	DT	M1
5	DT	B1
6	DT	B2
7	DT	$\mathrm{BEAM}=\mathrm{B1}\cdot\mathrm{B2}\cdot\overline{\mathrm{A6}}\cdot\overline{\mathrm{A7}}\cdot\overline{\mathrm{A}}$
8	DT	$\mathrm{A}=\sum \mathrm{A}_i$ (i=1-5 and 8,9)
9	DT	M1R
10	DT	$\mathrm{M0}\cdot\mathrm{M00}$
11	DT	$\mathrm{M}\cdot\overline{\mathrm{A}}$
12	DT	$\mathrm{B1}\cdot\mathrm{B2}$
13		E515 $\mathrm{TRIG}=\mathrm{BEAM}\cdot\mathrm{M}\cdot\overline{\mathrm{A}}$
14	DT	TRIG1
15	DT	TRIG3
16	DT	TRIG5
17	DT	A6
18	DT	A7
19	DT	$\mathrm{BEAM}\cdot 10^{-7}$
20	DT	LAC HITS
21	$\mathrm{UDT}=\overline{\mathrm{BEAM}}\cdot\mathrm{SUS}$	M
22	UDT	$\mathrm{B1}\cdot\mathrm{B2}$
23	UDT	BEAM
24	UDT	A6
25	UDT	$\mathrm{M}\cdot\overline{\mathrm{A}}$
26	UDT	E515
27	UDT	$\mathrm{B1}\cdot\mathrm{B2}$(delayed)
28	UDT	$\mathrm{BEAM}\cdot\overline{\mathrm{SUS}}$
29	UDT	A7
30	UDT	$\mathrm{BEAM}\cdot 10^{-7}$
31	UDT	$\mathrm{B1}\cdot\mathrm{B2}\cdot 10^{-7}$
32	UDT	

BEAM= Beam "on" condition.
SUS = Data aquisition suspended.
CDT = Computer "busy" conditon.

Table 11. Reduction of 1981 prompt muon triggers.

Analysis Stage	Events	Requirement
E-515 Triggers	1,175,192	muon trigger $B \cdot M \cdot \bar{A}$
Muon Tracking Pass	553,274	> 1 3-D MWPC track.
Pattern Recognition	324,481	M2-M3 roading. 3-D track linked with target.
Background Cuts	259,860	Magnet intercept cut. Halo muon cut. MWPC hit behind final absorber.

Table 12: Accidental muon identification levels are listed as a function of M5 hodoscope paddle number. These fractions are the ratio of accidental to all muons identified in the data. The accidental yield is evaluated by performing the muon analysis with MWPC tracks from an uncorrelated event.

Paddle No.	Location of center(m)	Accidental fraction(error)
1	-1.500	.390(.029)
2	-1.355	.382(.030)
3	-1.209	.340(.025)
4	-1.063	.391(.029)
5	-0.918	.512(.029)
6	-0.772	.654(.037)
7	-0.627	.799(.043)
8	-0.481	.853(.047)*
9	-0.355	.923(.051)*
10	+0.197	.747(.042)*
11	+0.342	.671(.038)
12	+0.487	.519(.037)
13	+0.632	.452(.036)
14	+0.777	.303(.029)
15	+0.923	.248(.026)
16	+1.068	.275(.028)
17	+1.213	.257(.027)
18	+1.358	.387(.037)

* removed from analysis

Table 13. Major sources of prompt and non-prompt electrons detected in the forward spectrometer arm.

Decay	Branching Ratio
$\pi^o \rightarrow \gamma\ \gamma$	98.85%
$\pi^o \rightarrow \gamma\ e^+\ e^-$	1.15%
$\eta \rightarrow \gamma\ \gamma$	38.00%
$\eta \rightarrow \gamma\ e^+\ e^-$	.50%
$K^\pm \rightarrow e^\pm\ \nu\ \pi^o$	4.82%
$K_1^o \rightarrow e^\pm\ \nu\ \pi$	38.8%

Table 14. Muon-electron Monte Carlo of spectrometer acceptance and efficiency with Model A (page 96):

$$\frac{d\sigma}{dM\, dX_F\, dPt^2} \propto e^{-5M} (1-X_F)^a e^{-bPt}$$

$$M \rightarrow D_1 \, D_2$$
$$\searrow Ke\nu$$
$$\rightarrow K\mu\nu$$

The definitions of the column heads are: (1) exponent, (2) exponent, (3) muon acceptance, (4) electron acceptance, (4) joint muon-electron acceptance,(5) muon MWPC efficiency, (6) electron MWPC efficiency, (7) shower detector efficiency, and (8) muon and electron charges. The efficiencies were derived from detection efficiency maps for the various detectors, and are averaged over the accepted events.

a	b	a_μ	a_e	$a_{\mu e}$	ε_μ	ε_e	ε_{lac}	$Q_{\mu e}$
3.	1.	.0347	.2420	.0087	.935	.679	.559	+ −
3.	1.	.0335	.2290	.0083	.929	.646	.449	− +
5.	1.	.0401	.2319	.0092	.935	.687	.549	+ −
5.	1.	.0373	.2068	.0092	.927	.657	.430	− +
3.	3.	.0338	.2511	.0098	.931	.673	.537	+ −
3.	3.	.0320	.2208	.0090	.930	.646	.430	− +
5.	3.	.0363	.2427	.0090	.938	.693	.562	+ −
5.	3.	.0347	.2092	.0091	.923	.654	.445	− +

Table 14. (cont.) Muon-electron Monte Carlo of spectrometer acceptance and efficiency with inclusive Model B:

$$\frac{E\,d\sigma}{dX_F dPt^2} \propto (1-X_F)^a e^{-bPt}$$

a	b	a_μ	a_e	$a_{\mu e}$	ε_μ	ε_e	ε_{lac}	$Q_{\mu e}$
3.	1.	.0394	.2751	.0108	.933	.689	.551	+ -
3.	1.	.0366	.2541	.0095	.933	.649	.440	- +
5.	1.	.0436	.2462	.0107	.936	.693	.519	+ -
5.	1.	.0431	.2304	.0100	.930	.659	.448	- +
3.	3.	.0206	.2785	.0057	.935	.667	.559	+ -
3.	3.	.0220	.2610	.0063	.935	.631	.443	- +
5.	3.	.0248	.2554	.0075	.935	.653	.567	+ -
5.	3.	.0251	.2341	.0057	.928	.648	.412	- +

Table 15. Muon identification algorithm reconstruction efficency, determined from Monte Carlo. The first column indicates muon momentum, the second column indicates the reconstruction efficiency for direct muons, the third and fourth columns indicate the reconstruction efficiency for pions and kaons decaying in flight after exiting the MWPC system.

P_{μ} (GeV)	Direct muons ε_{rec}	Pion Decays ε_{rec}	Kaon Decays ε_{rec}
5	.91	.42	.04
7	.89	.65	.05
9	.89	.70	.05
11	.88	.70	.05
13	.88	.70	.05
15	.90	.70	.05
17	.92	.72	.05
19	.94	.74	.05
21	.94	.78	.05
21	.95	.80	.05
25	.95	.80	.06
27	.96	.80	.06
29	.98	.84	.06
31	.98	.87	.09
33	.98	.88	.10
35	.98	.90	.10
37	.99	.91	.10
39	.99	.92	.12

Table 16. Monte Carlo calculations of the detector acceptance with the Chicago-Princeton dimuon results [41] for X_F and Pt distributions; and Model A for double semileptonic decays of charmed particles.

Dimuon Source	a_μ^{trig}	a_μ^{forw}	$a_{\mu\mu}$	ε_μ^{trig}	ε_μ^{forw}	Q_μ^{trig}	Q_μ^{forw}
total	.0079	.1400	.00084	.933	.735	+	−
total	.0074	.2197	.00090	.936	.632	−	+
ψ	.0681	.1363	.0087	.921	.724	+	−
ψ	.0646	.1536	.0107	.924	.651	−	+
ϕ	.0159	.1116	.0027	.929	.730	+	−
ϕ	.0150	.1870	.0031	.932	.628	−	+
$\rho\omega$	.0082	.1160	.0012	.938	.722	+	−
$\rho\omega$	.0075	.2031	.0012	.934	.640	−	+
$D\ \bar{D}$	.0465	.1197	.0059	.929	.725	+	−
$D\ \bar{D}$	.0437	.1393	.0061	.926	.649	−	+

Table 17. Excess dimuon yield binned as a function of forward muon momentum. The raw yields are corrected for detection efficiencies in the forward spectrometer arm; (1) muon hodoscope efficiency, (2) muon pattern recognition efficiency; (3) MWPC tracking efficiency.

Excess		Corrected Excess		Total	P_{bin}(GeV)
$\mu^+\mu^-$	$\mu^-\mu^+$	$\mu^+\mu^-$	$\mu^-\mu^+$		
177±59	84±45	653±258	320±183	973±316	4-8
223±53	135±39	826±268	526±187	1363±327	8-12
94±39	53±31	343±161	202±122	545±202	12-16
64±26	58±24	226±105	213±99	439±144	16-20
65±25	51±26	224±98	183±123	408±157	20-28
25±16	23±24	84±58	79±92	164±109	28-50
				3892±703	

$\langle \varepsilon^{\mu^+}_{H} \rangle = .458 \pm .017$ $\qquad$ $\langle \varepsilon^{\mu^-}_{H} \rangle = .410 \pm .018$

$\langle \varepsilon^{\mu^+}_{pwc} \rangle = .63$ $\qquad$ $\langle \varepsilon^{\mu^-}_{pwc} \rangle = .74$

$\langle \varepsilon^{\mu\pm}_{rec} \rangle = .91$

Table 18. Excess dimuon yield binned as a function of dimuon invariant mass. The raw yields are corrected for detection efficiencies in the forward spectrometer arm.

Excess		Corrected Excess		Total	Mass(GeV)
$\mu^+\mu^-$	$\mu^-\mu^+$	$\mu^+\mu^-$	$\mu^-\mu^+$		
160±37	13±33	593±188	49±126	641±226	.00-.750
232±52	208±43	855±226	792±229	1648±351	.75-1.00
163±49	39±40	595±221	149±155	744±270	1.00-1.25
36±37	42±30	130±138	158±117	288±181	1.25-1.50
10±25	42±22	34±88	153±88	188±124	1.50-1.75
28±17	36±15	99±62	133±61	231±87	1.75-2.00
5±12	-12±12	17±42	-45±45	-27±61	2.00-2.50
10±6	19±7	35±23	69±30	104±38	2.50-3.00
18±5	10±5	63±22	37±18	101±29	3.00-3.50
3±2	8±3	10±9	31±13	41±16	3.50-5.00

Table 19. Dimuon invariant mass with momentum cuts applied to the forward muon momentum. The maximum muon momentum considered was 50 GeV.

P_μ > 4GeV	P_μ > 10GeV	P_μ > 16GeV	P_μ > 22GeV	Mass(GeV)
641±226	175±11	54±39	18±18	.00-.750
1648±351	954±218	283±97	66±50	.75-1.00
744±270	339±181	124±113	9±70	1.00-1.25
288±181	159±140	119±99	45±70	1.25-1.50
188±124	50±102	20±81	57±62	1.50-1.75
231±87	213±78	133±66	112±53	1.75-2.00
-27±61	-33±56	15±49	30±40	2.00-2.50
104±38	103±35	92±32	61±27	2.50-3.00
101±29	94±27	88±25	67±22	3.00-3.50
41±16	45±15	45±15	38±14	3.50-5.00

Table 20. Compilation of $\sigma_\psi \cdot B_{\mu\mu}$ for π^--N (X_F>0.) interactions at various center of mass energies. Where extrapolations were necessary; a branching ratio, $B_{\psi\to\mu\mu}$, of .07, and an A-dependence of $A^{.93}$, were used. The final row gives our extrapolation of the cross section to π^-Be interactions at $\sqrt{s}$=19., from references [54] and [56].

Interaction	$\sqrt{s}$ (GeV)	$\sigma \cdot B_{\mu\mu}$/N (nb)	Reference
π^- C	20.6	14.0(±1.0)	[54]
π^+ Be	16.8	6.5(±2.2)	[41]
π^- Be	16.8	4.9(±0.5)	[55]
π^- W	15.3	4.0(±0.8)	[56]
π^- Be	19.4	11.7(±1.2)	extrapolation to E515

Table 21. Raw excess of dimuons binned as a function of the indicated cuts on the trigger muon: (1) decay probability, (2) muon momentum, (3) transverse momentum, (4) vertical lab angle, (5) midplane deviation. The percentage of total muons found in each bin is also indicated.

Excess Yield	Total Muons	%	Cut
			Decay Probability
227±47	1354.	.17	0.0-2.0 x10^{-4}
475±73	3157.	.15	2.0-3.0 x10^{-4}
148±51	1552.	.10	3.0-3.5 x10^{-4}
64±44	1166.	.06	3.5-4.0 x10^{-4}
144±59	2105.	.07	4.0-10. x10^{-4}
			Momentum
9±54	2428.	.00	0.0-6.0 GeV
270±53	1597.	.17	6.0-7.0 GeV
156±50	1465.	.11	7.0-8.0 GeV
309±56	1839.	.17	8.0-10. GeV
315±58	2042.	.15	10.-25. GeV
			Pt
245±69	2841.	.09	0.0-0.6 GeV
306±70	2933.	.10	0.6-0.8 GeV
237±54	1692.	.14	0.8-1.0 GeV
259±57	1905.	.14	1.0-5.0 GeV
			Θ_v
90±38	844.	.11	.04-.06 rdn.
746±102	6240.	.12	.06-.09 rdn.
212±62	2293.	.09	.09-.15 rdn.
			ΔX_{mid}
396±70	2864.	.14	.000-.015 meter
305±62	2237.	.14	.015-.030 meter
79±51	1563.	.05	.030-.045 meter
279±61	2232.	.13	.045-.200 meter

Table 22. Least squares fitting results for the E/P spectra used to derive the excess muon-electron yields. The error in the electron/positron signal was determined from the error matrix of the least squares fit and standard error propagation techniques. A sample calculation of the raw yield, following equations 3-4 and 3-5 of the text, is given below. The error in the trigger asymmetry ratio, α_{ee}, is included in the final error. No cuts were applied to the data. DOF=50.

Q_m	Q_e	Signal	Background	$e^{\pm}$ Pairs	χ^2
+	+	563±38	201	566	64.
+	−	1132±55	404	865	43.
−	+	625±40	210	560	39.
−	−	862±50	401	879	48.

$$\Delta I^{\mu+e-} = 1132 - (865/879)862 = 284 \pm 83$$

$$\Delta I^{\mu-e+} = 625 - (560/566)563 = 67 \pm 64$$

Table 23. Excess yields of opposite signed μ-e's following the given cuts on the trigger muon or electron.

Excess μ+e-	Excess μ-e+	Cut
		Shower-track residual
284±84	67±64	RADIUS < 3cm
266±82	55±61	RADIUS < 2cm
206±77	44±57	RADIUS < 1cm
		Muon momentum
252±74	29±59	$P_\mu > 6.$ GeV
		Muon decay probability
215±76	11±58	$P_d < 4.\times10^{-4}$
		Electron momentum
86±33	27±24	$0.0 < P_e < 8.0$ GeV
131±59	43±49	$8.0 < P_e < 16.0$ GeV
76±37	-13±27	$16.0 < P_e < 24.0$ GeV
7±27	-2±23	$24.0 < P_e < 50.0$ GeV
		Electron Pt
79±59	67±44	0.0 < Pt < .25 GeV
170±47	-11±39	.25 < Pt < .50 GeV
15±41	9±18	.50 < Pt < 1.0 GeV

Figure 1: Plan and Elevation view of the E515 spectrometer.

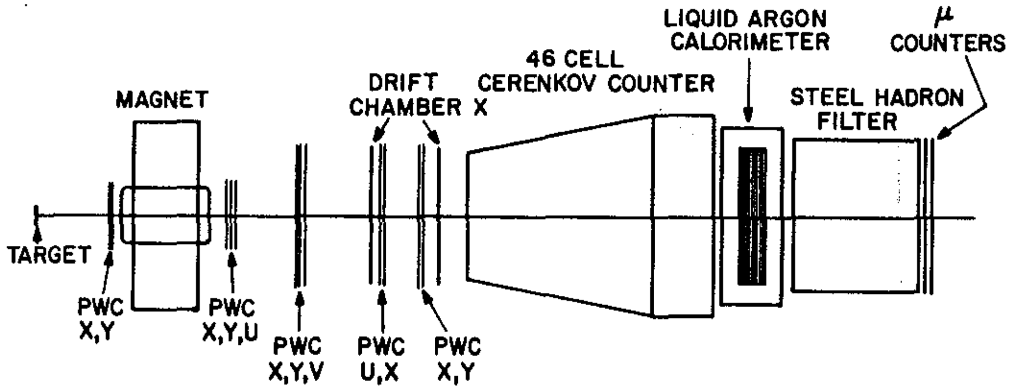

E515 PLAN VIEW

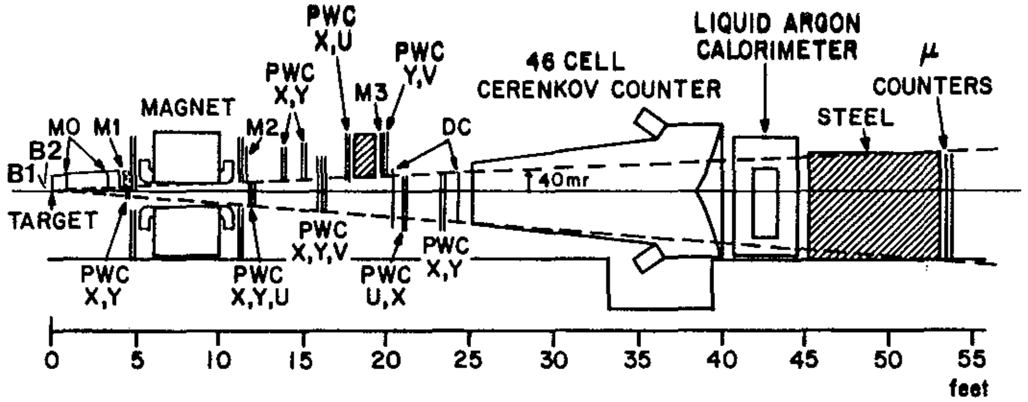

E515 ELEVATION VIEW

Figure 2: Representation of charged and neutral currents in the standard theory of electro-weak interactions [12,13].

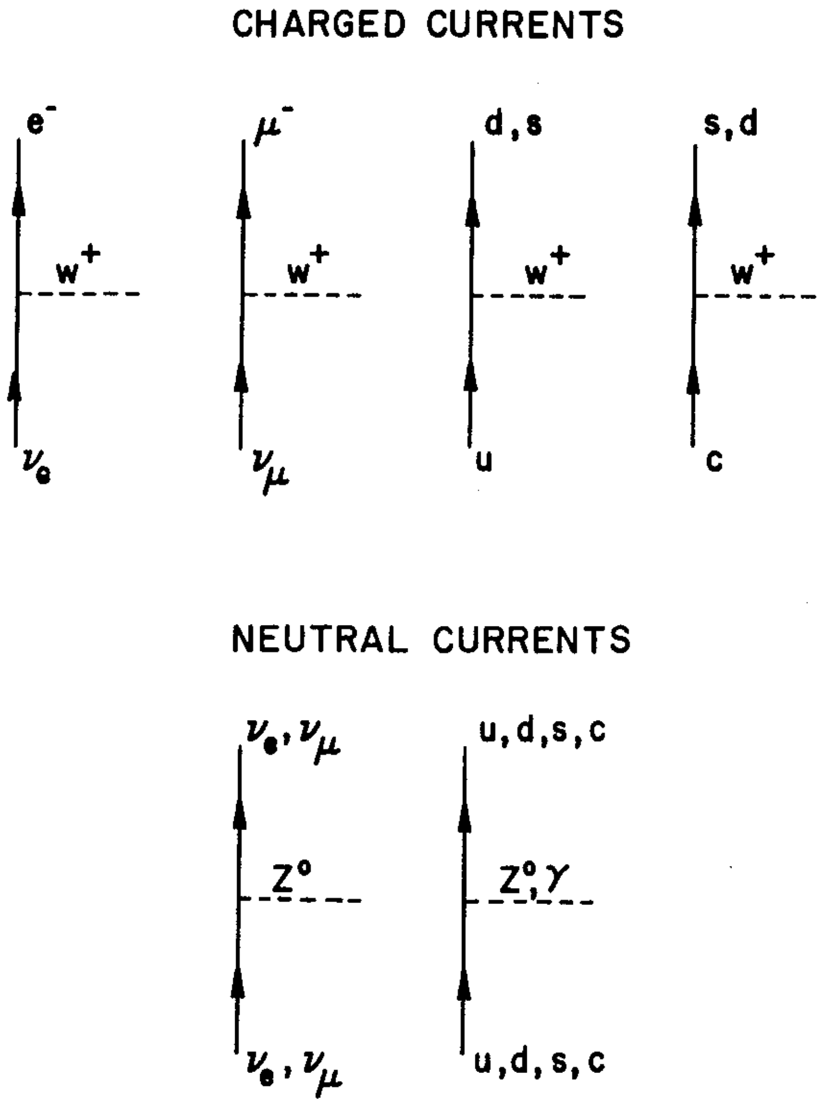

Figure 3. Annihilation diagrams contributing to charmed particle decays. The charmed quarks and light quarks both participate in the decay.

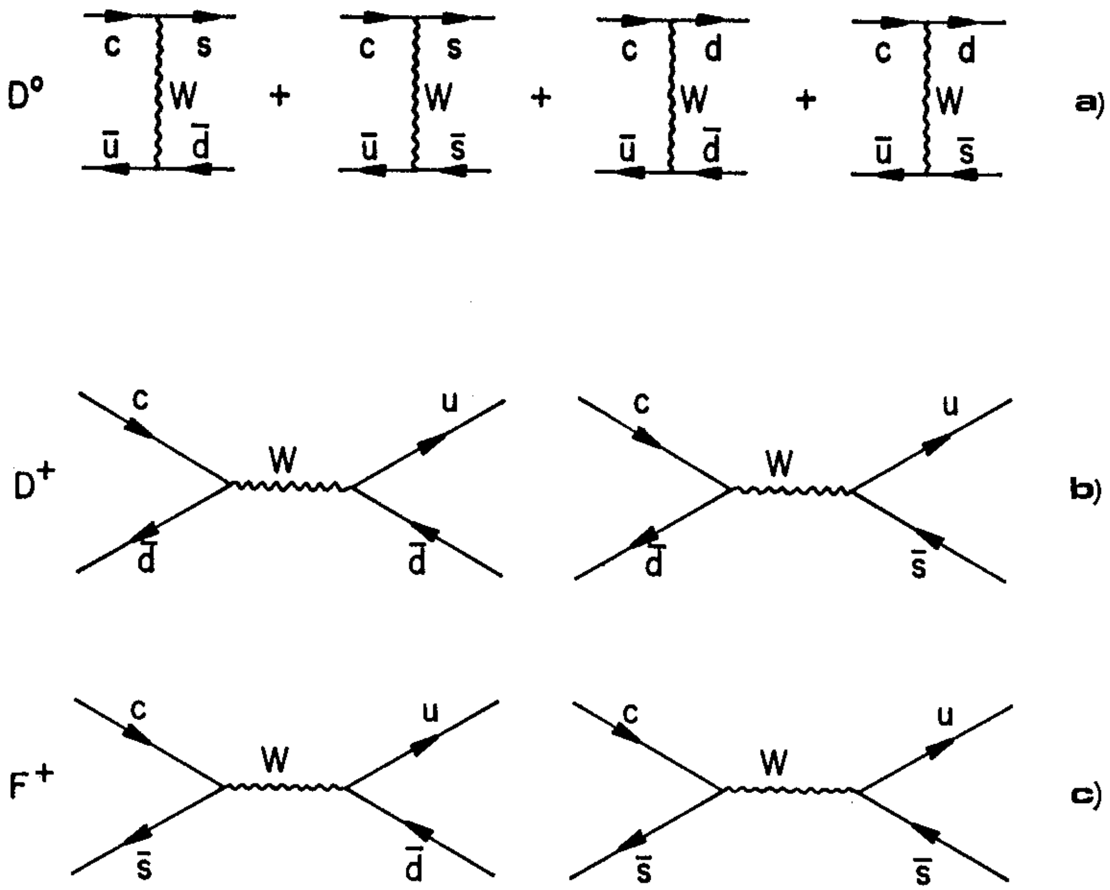

Figure 4. Spectator diagrams contributing to charmed particle decays. The light quarks do not contribute to the decay process.

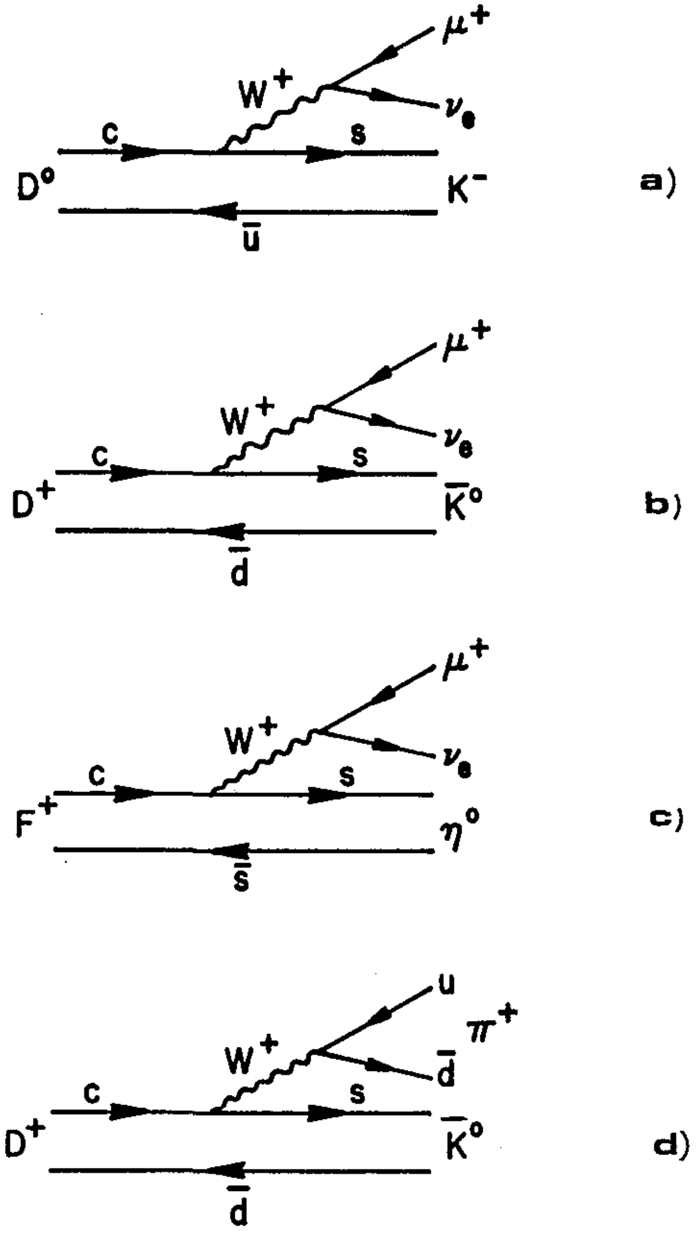

Figure 5. Lowest order QCD charm production subprocesses.

LOWEST ORDER QCD CHARM PRODUCTION PROCESSES

a) quark annihilation

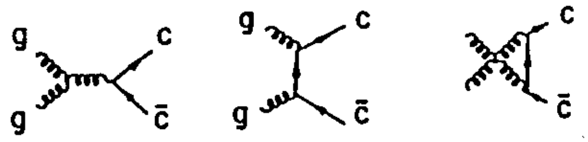

b) gluon fusion

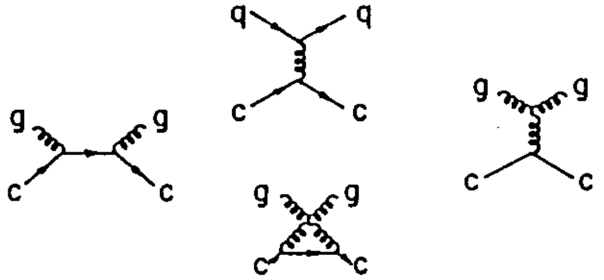

c) quark excitation

Figure 6. Monte Carlo generated momemtum spectra from prompt and non-prompt sources of muon triggers.

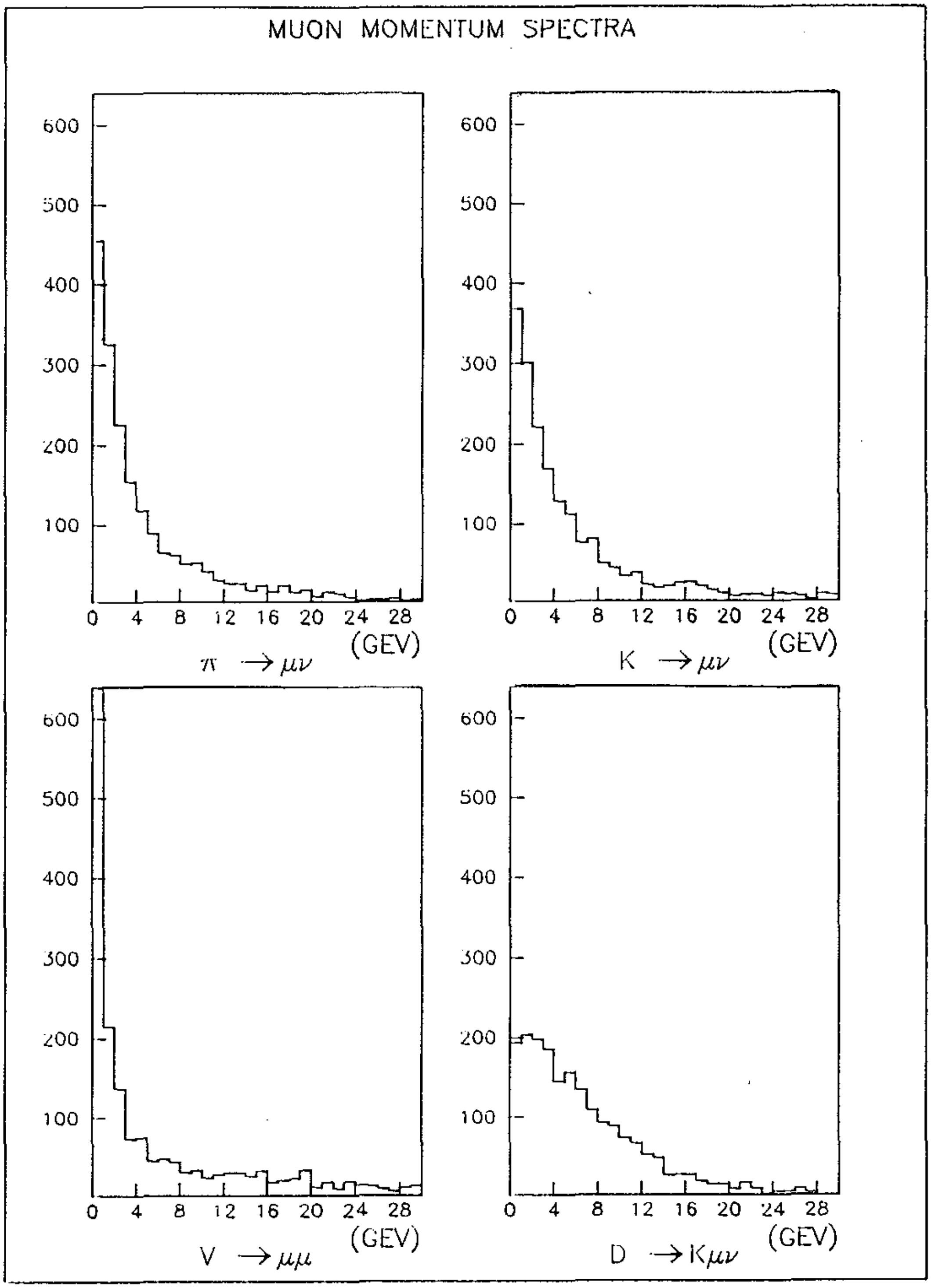

Figure 7. Monte Carlo generated transverse momentum spectra from prompt and nonprompt sources of muon triggers.

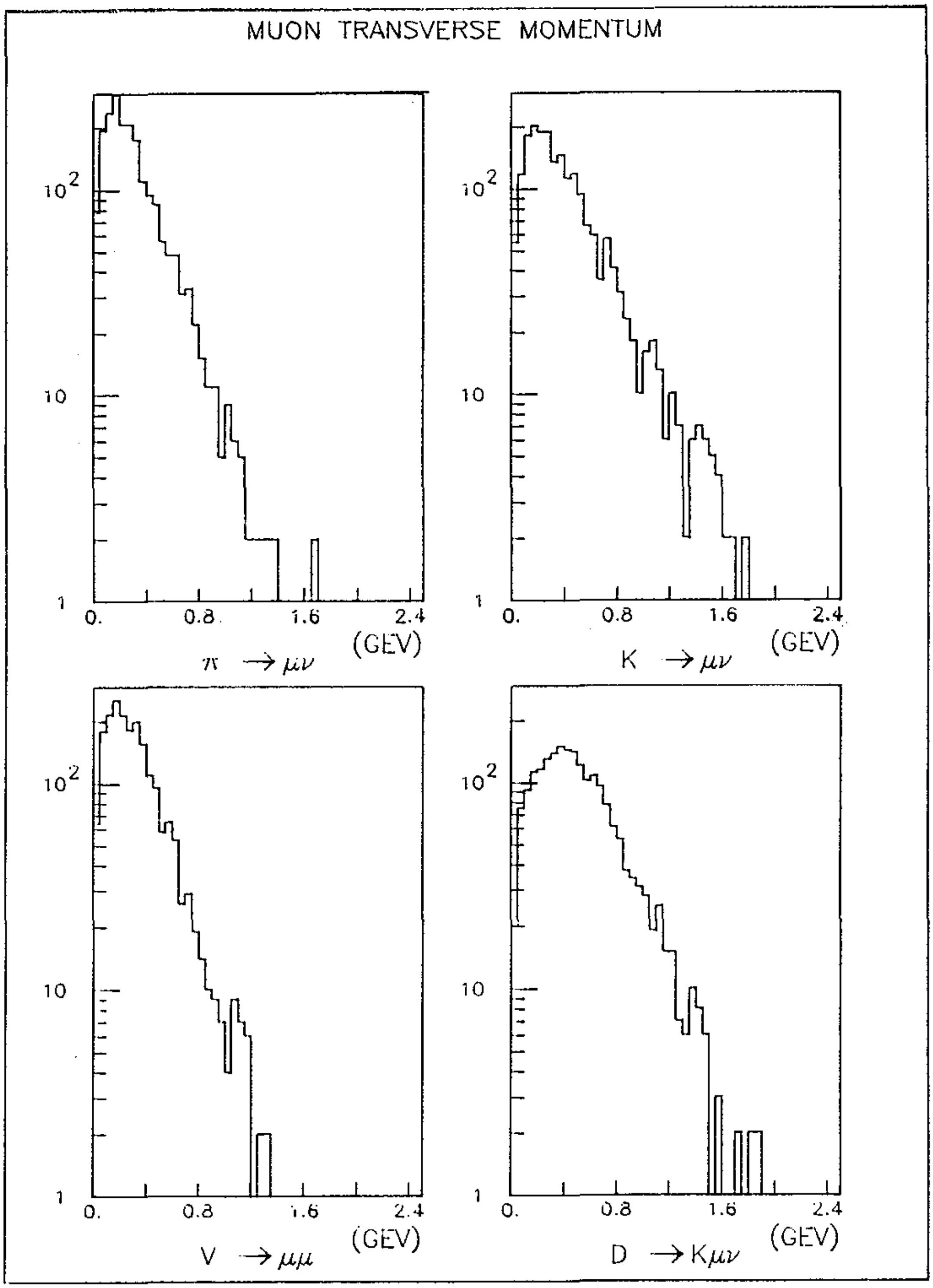

Figure 8. Momentum and transverse momentum acceptance of the muon trigger arm.

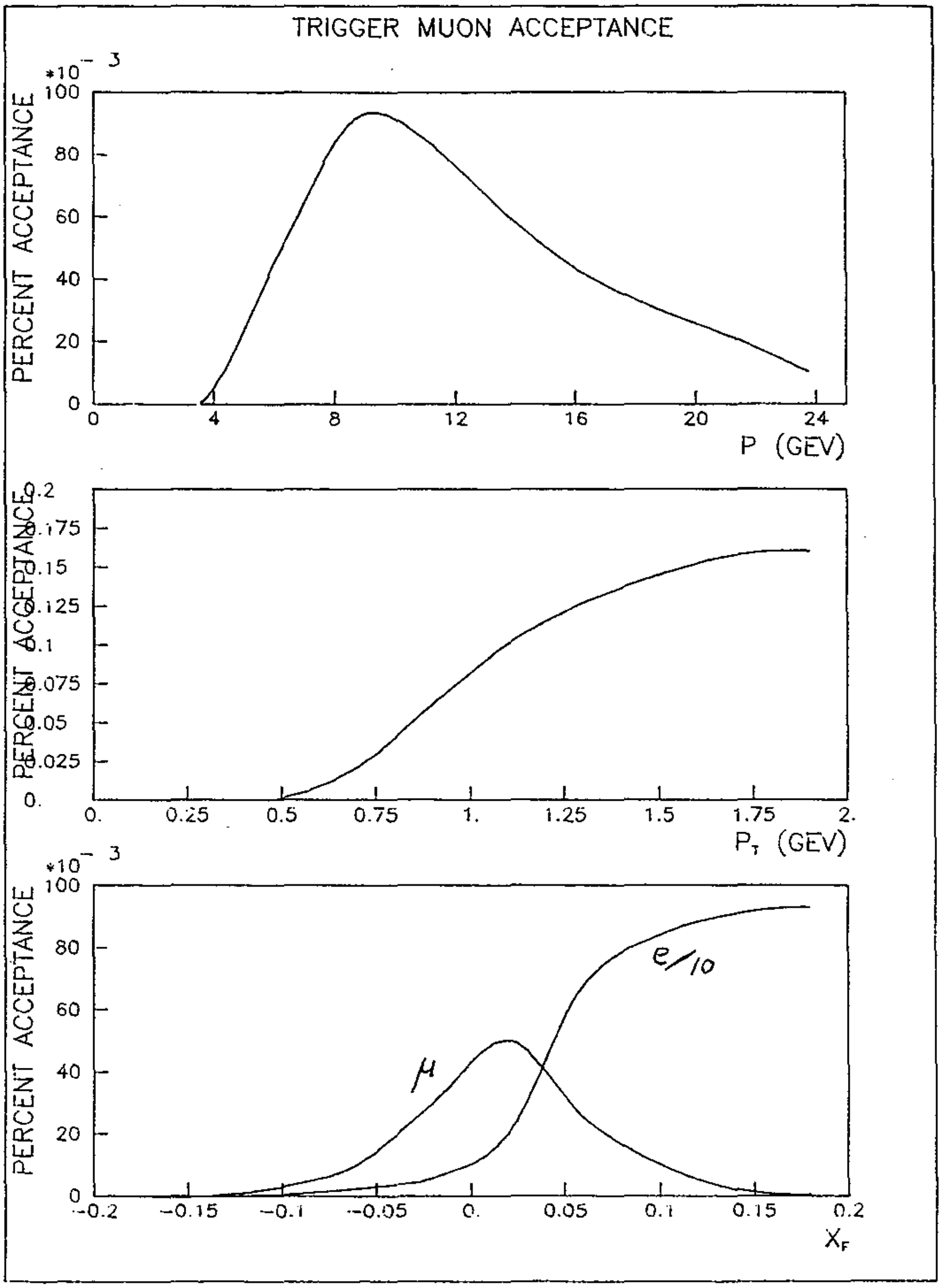

Figure 9. The E-515 beamline leading into the spectrometer.

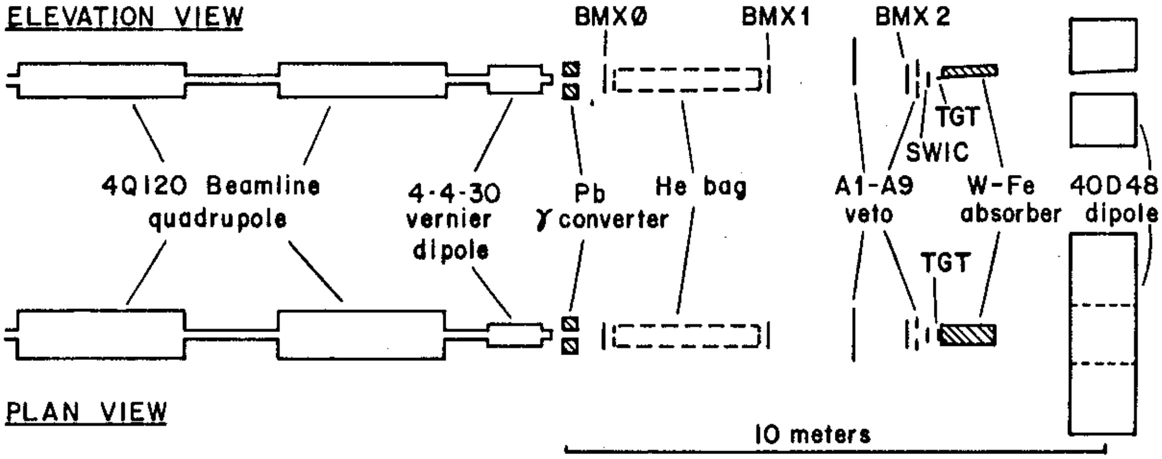

Figure 10. M1 hodoscope logic diagram.

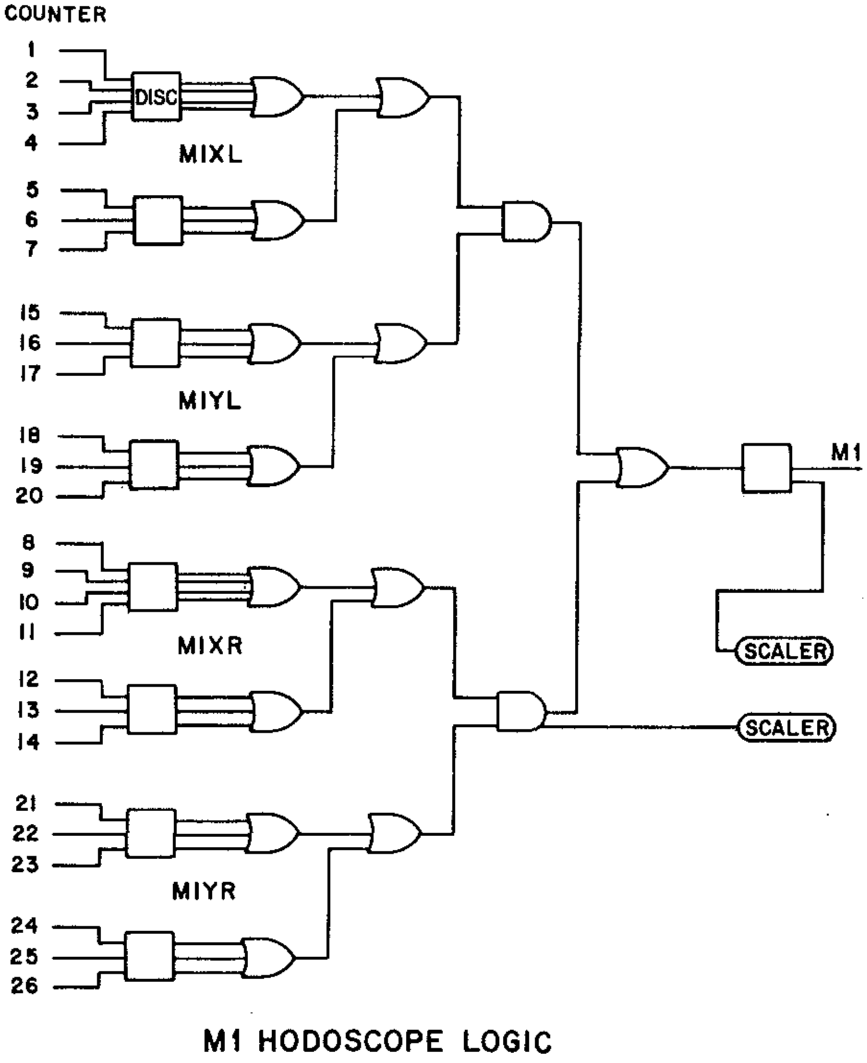

Figure 11. M2-M3 hodoscope matrix logic diagram.

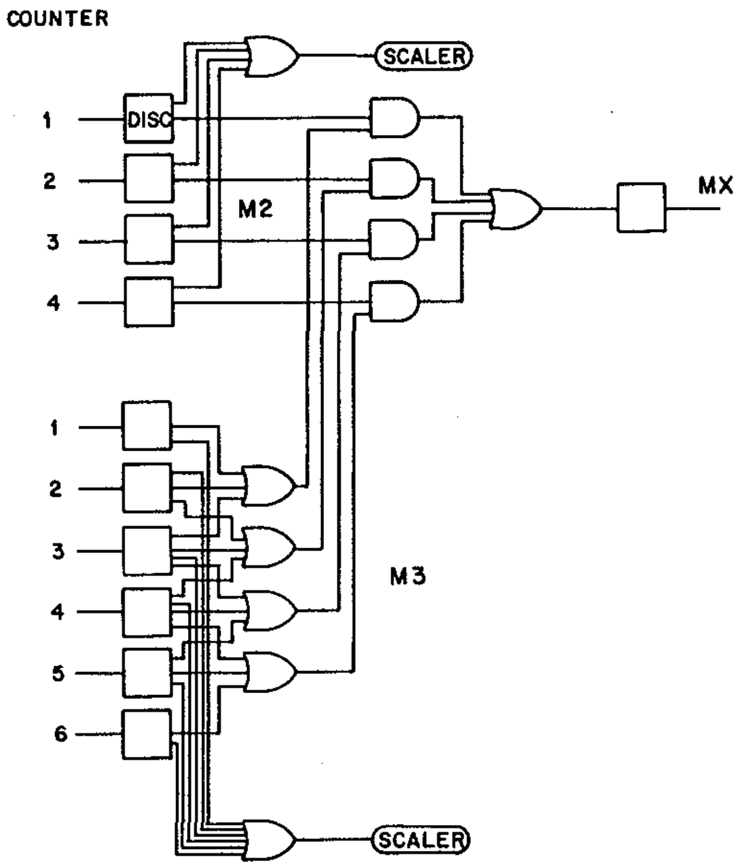

M2·M3 MATRIX LOGIC

Figure 12. M2-M3 trigger matrix. Only connected counters could contribute to the muon trigger.

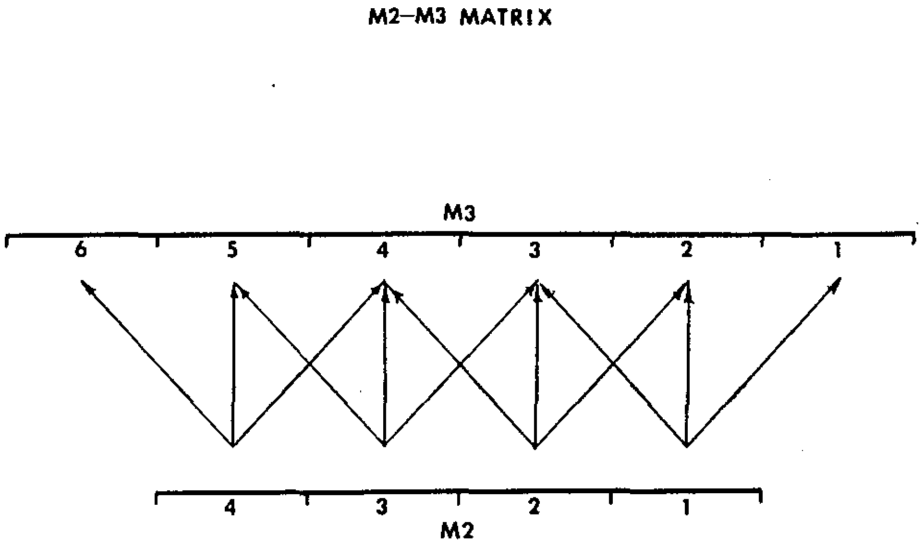

Figure 13. E-515 trigger logic.

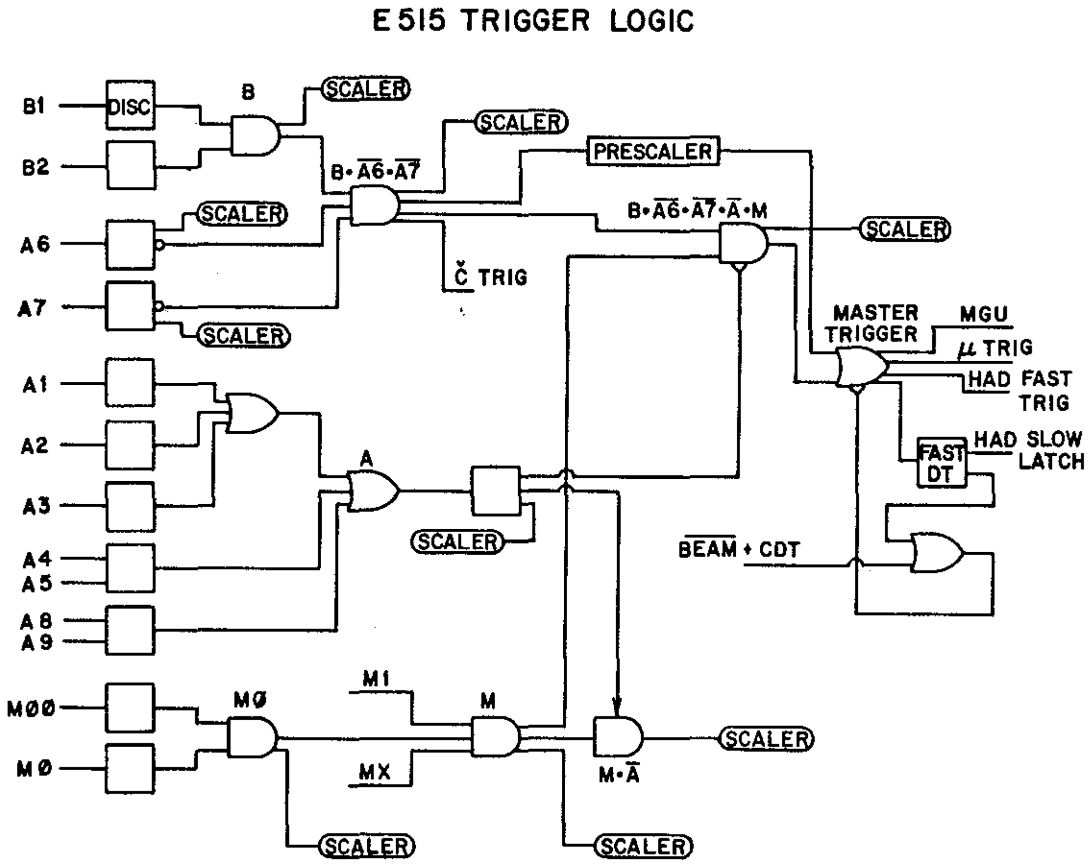

Figure 14. Target and W-Fe absorber assembly.

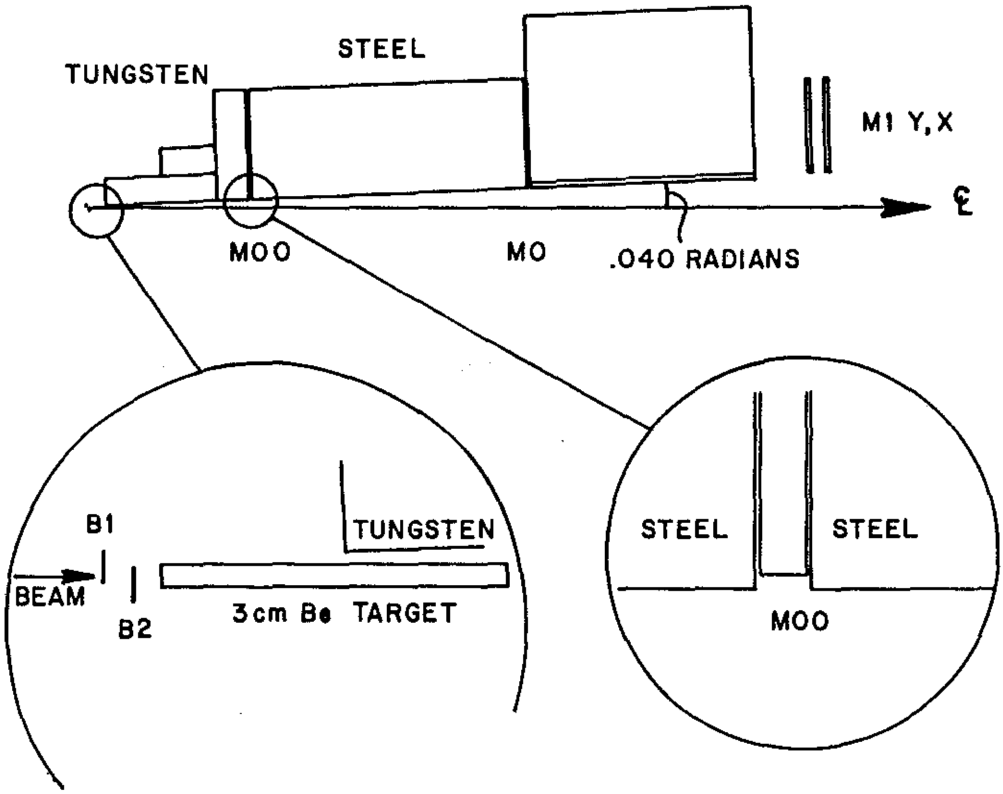

Figure 15. Perspective view of the M1 hodoscope showing the overlapping paddle arrangement.

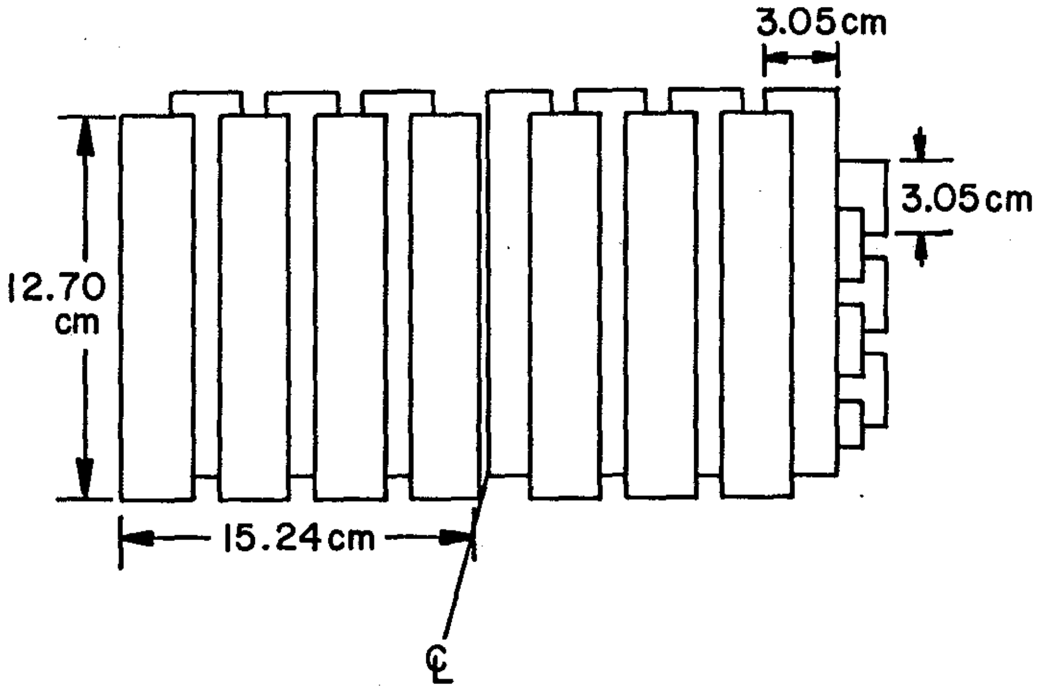

Figure 16. Electronics for reading out the MWPC's in the muon trigger arm.

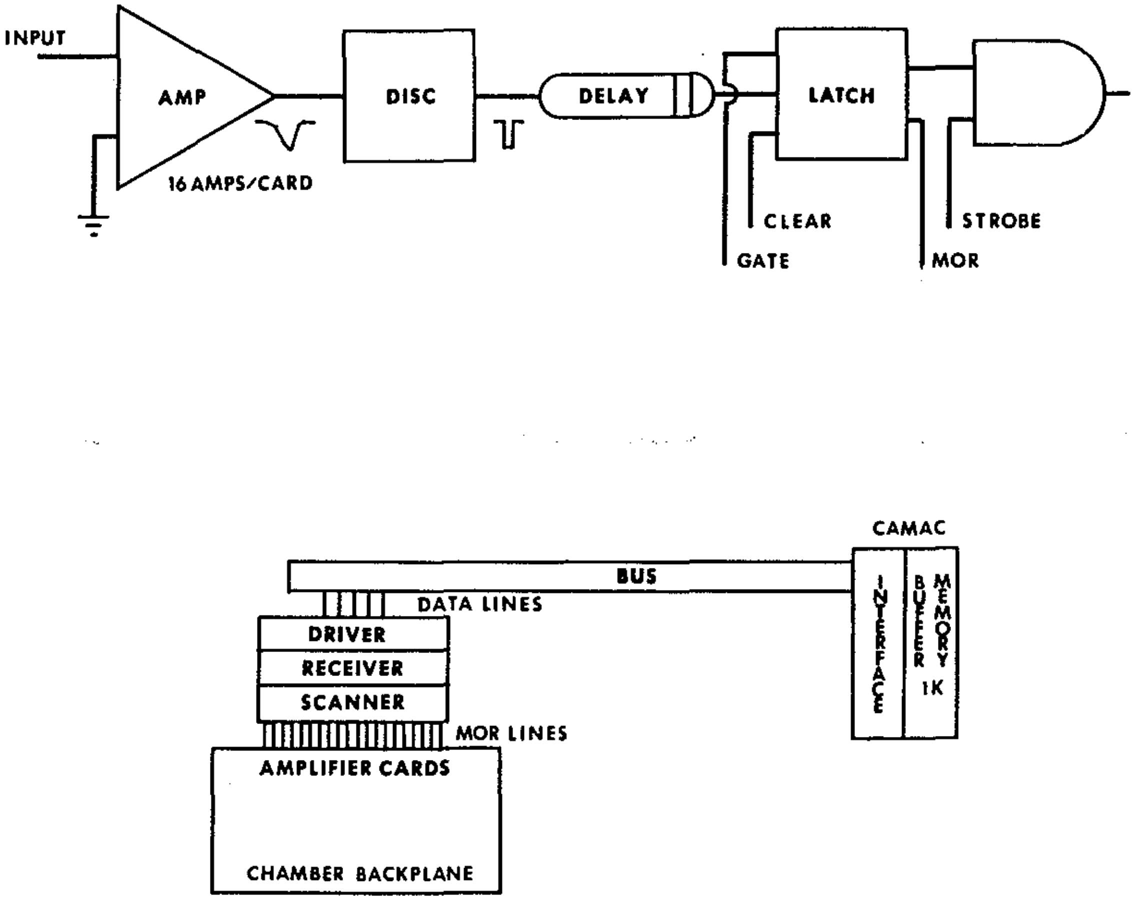

Figure 17. Multicelled Cerenkov counter.

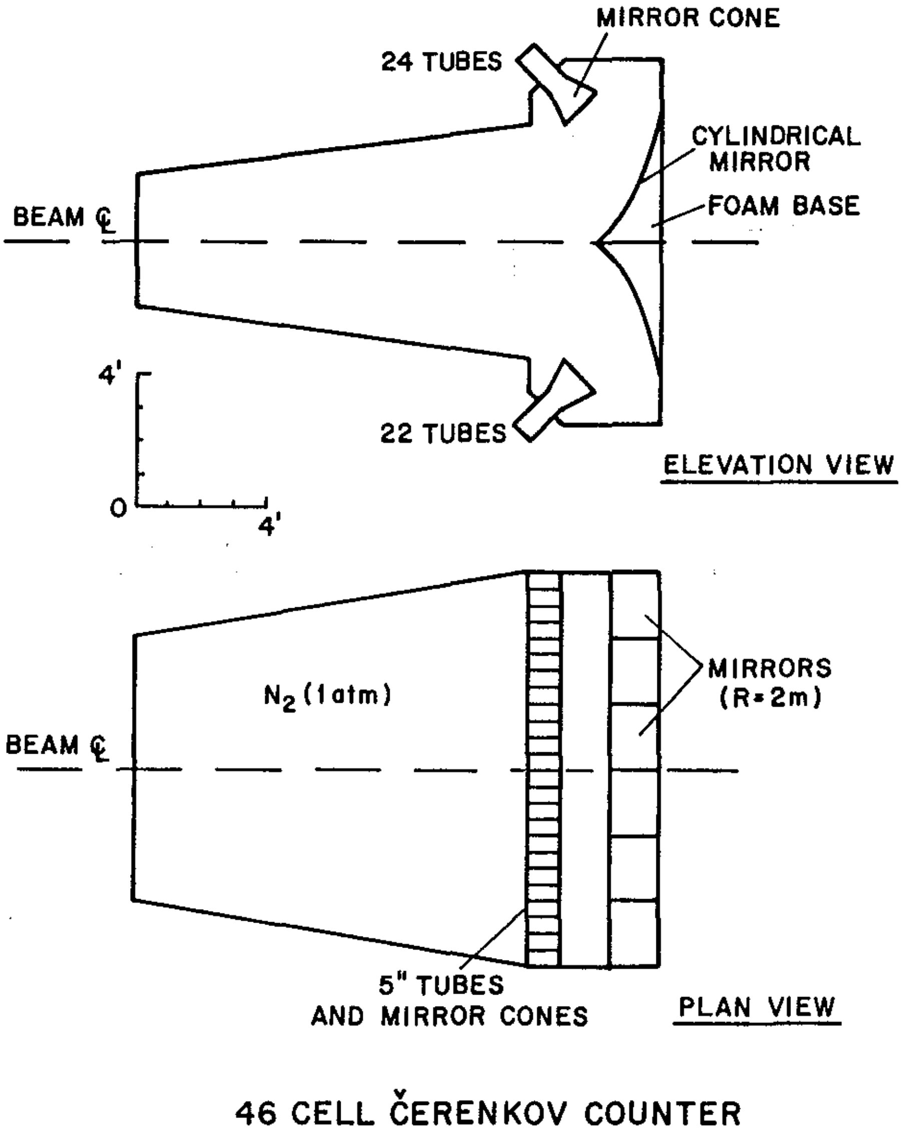

Figure 18. Front and side view of the electromagnetic shower detector assembly.

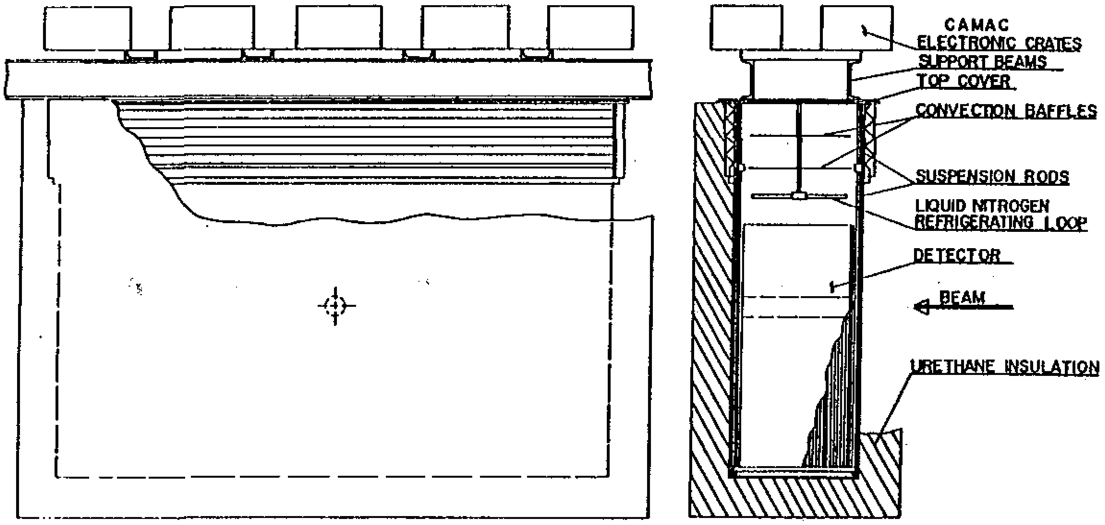

Figure 19. One cell of the shower detector lattice.

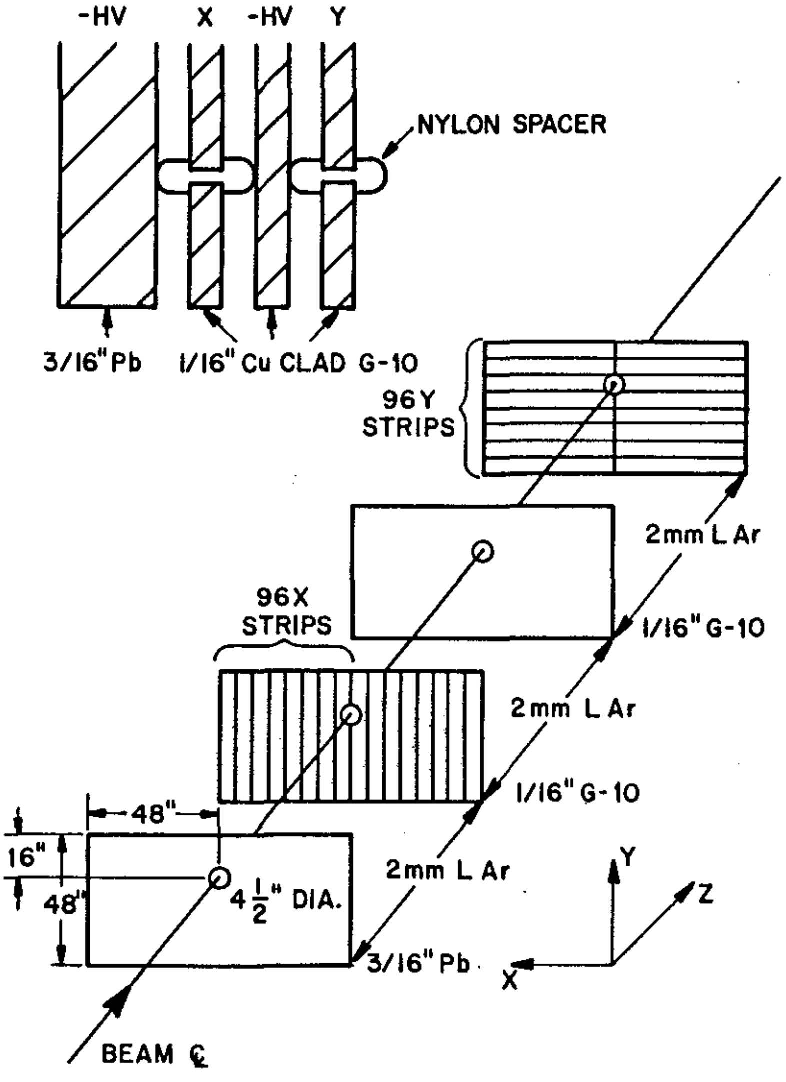

SHOWER DETECTOR CELL

Figure 20. Front view of the (Cu-clad G-10) anode read out boards used in the electromagnetic shower detector.

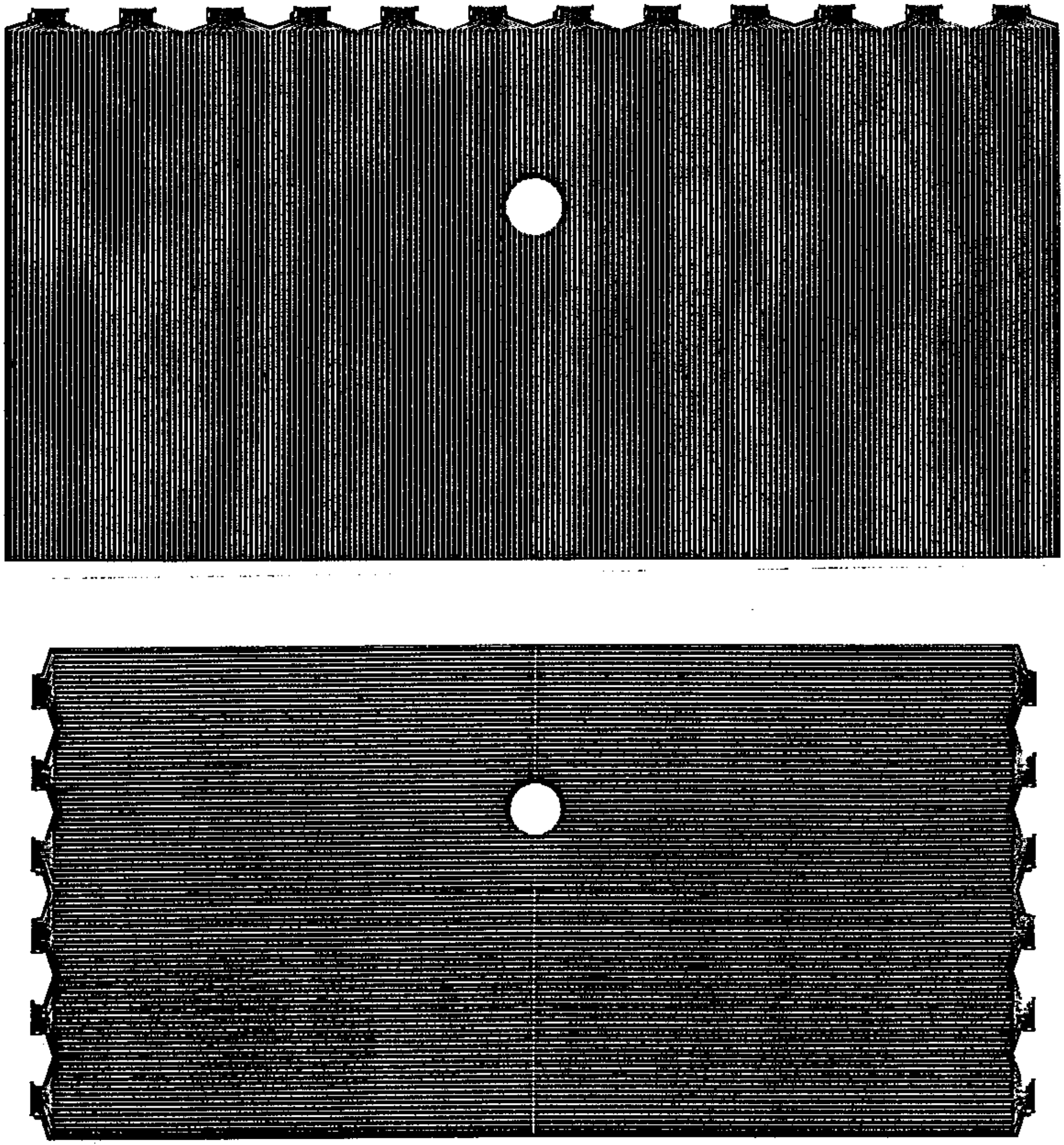

Figure 21. Shower detector read out electronics.

a) Electronics for one channel of LAC

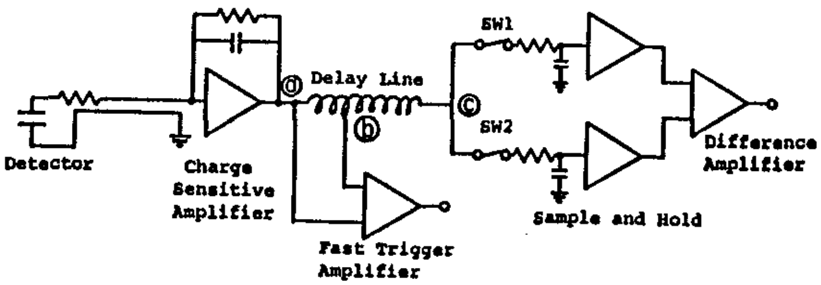

b) Signal at point ©

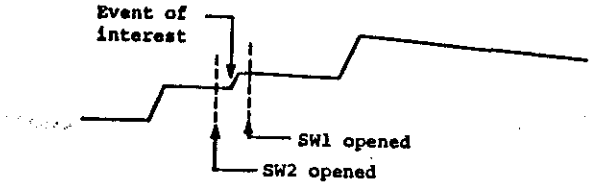

c) Read-out system

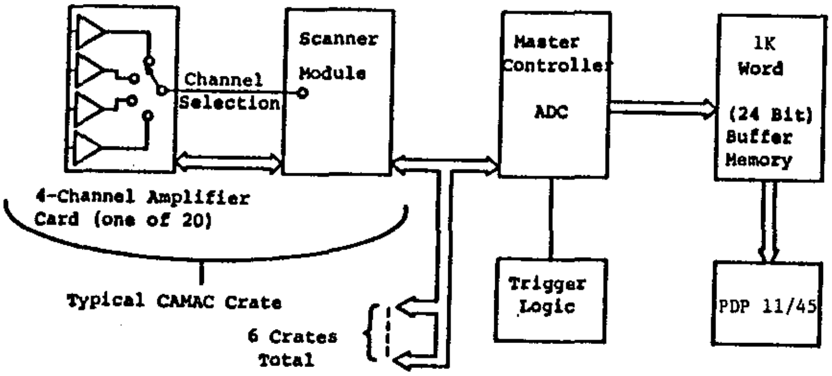

Fig. 3

Figure 22. Perspective view of the rear hadron dump and muon hodoscopes.

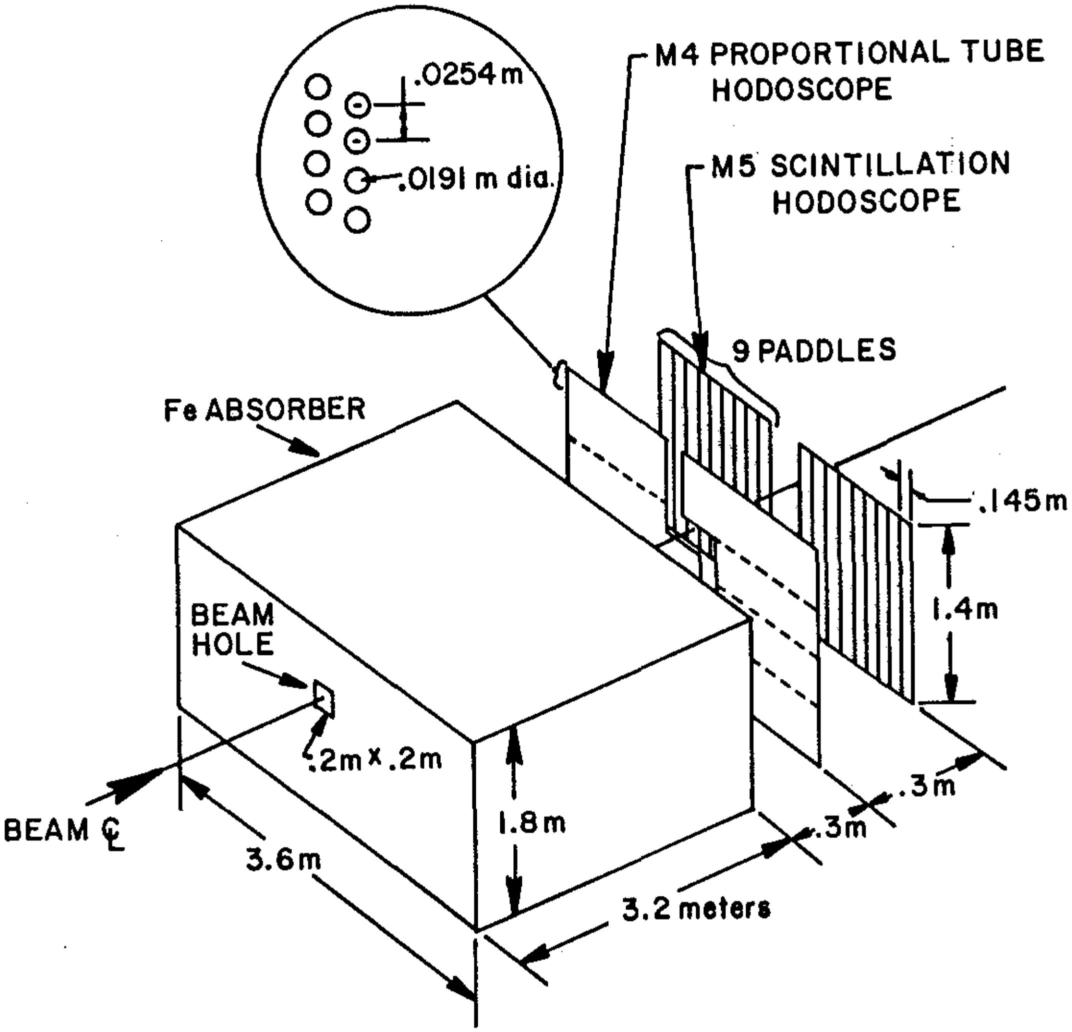

Figure 23. Schematic of the E-515 data aquisition system.

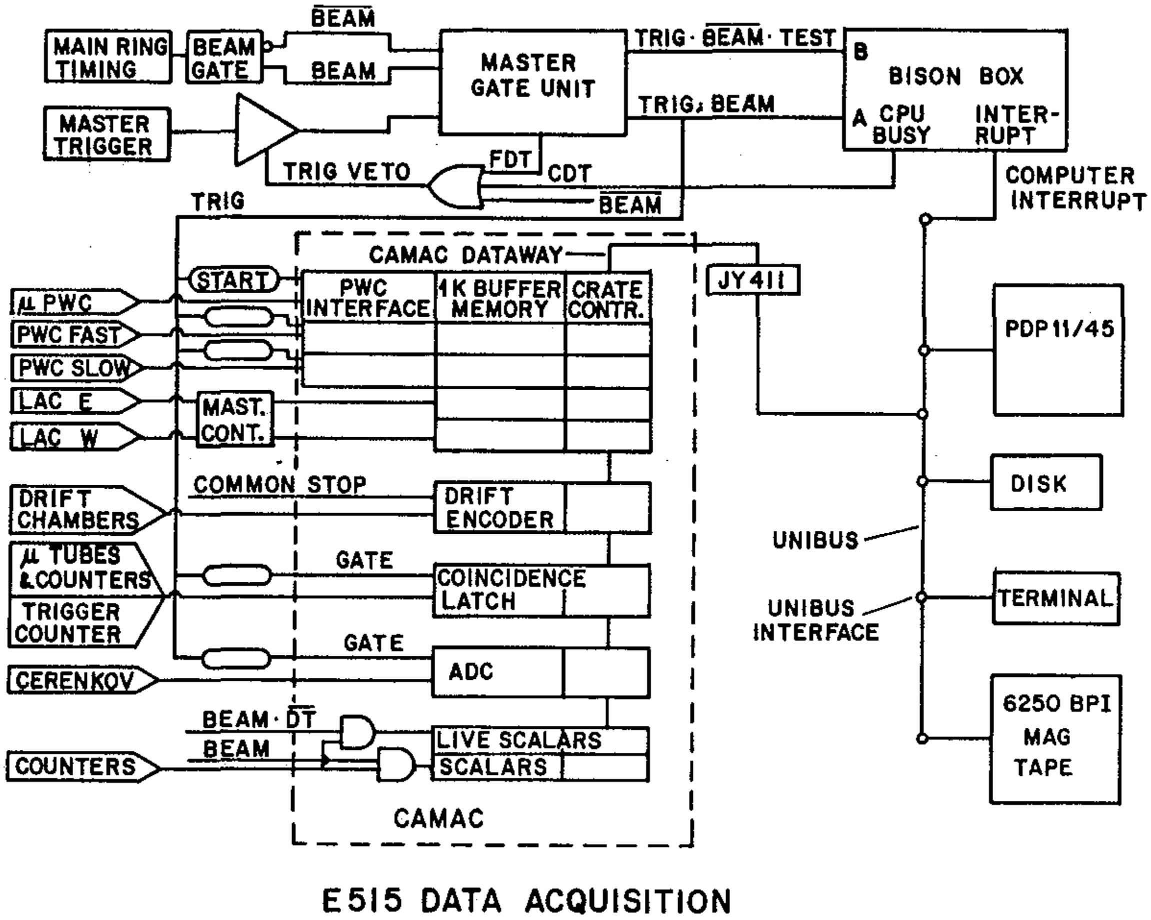

Figure 24. Muon trigger arm including muon trigger hodoscopes and multiwire proportional chambers for tracking.

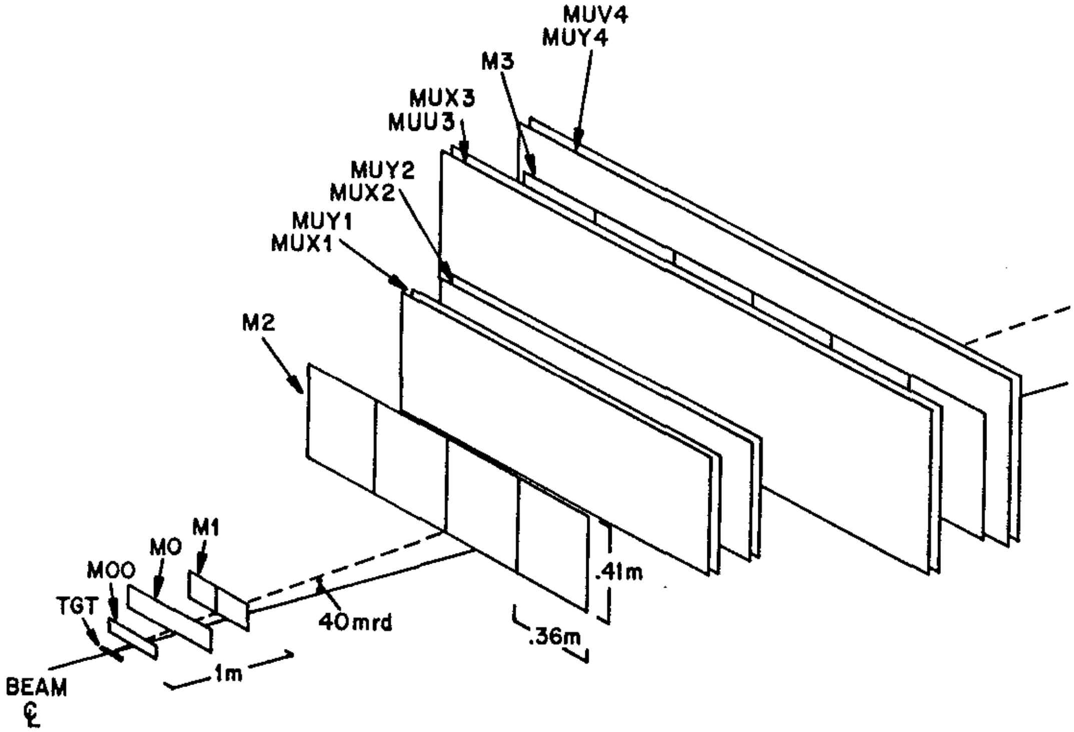

Figure 25. Magnet center deviations, used for muon track reconstruction.

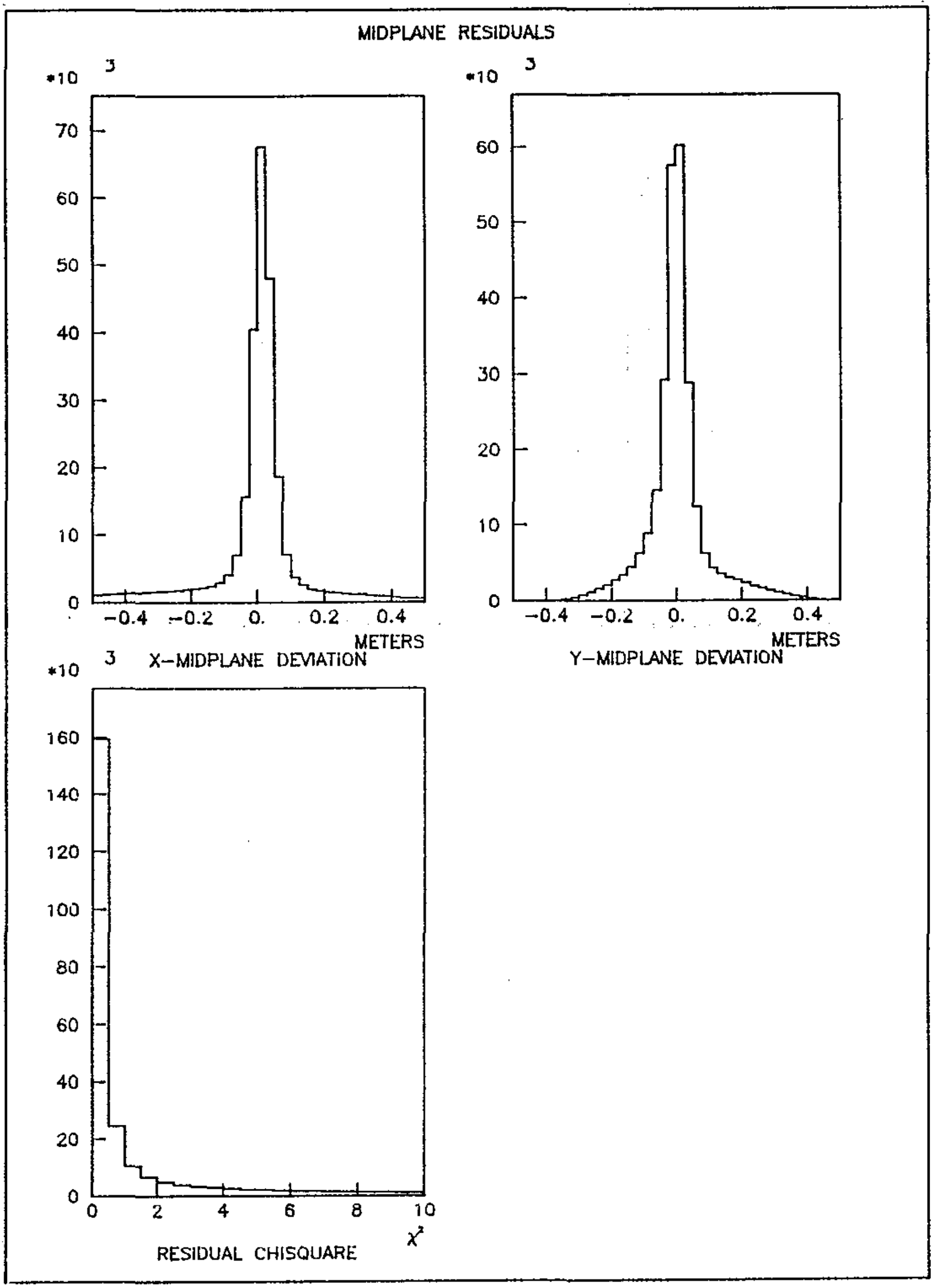

Figure 26. Charge determination reliability as a function of momentum.

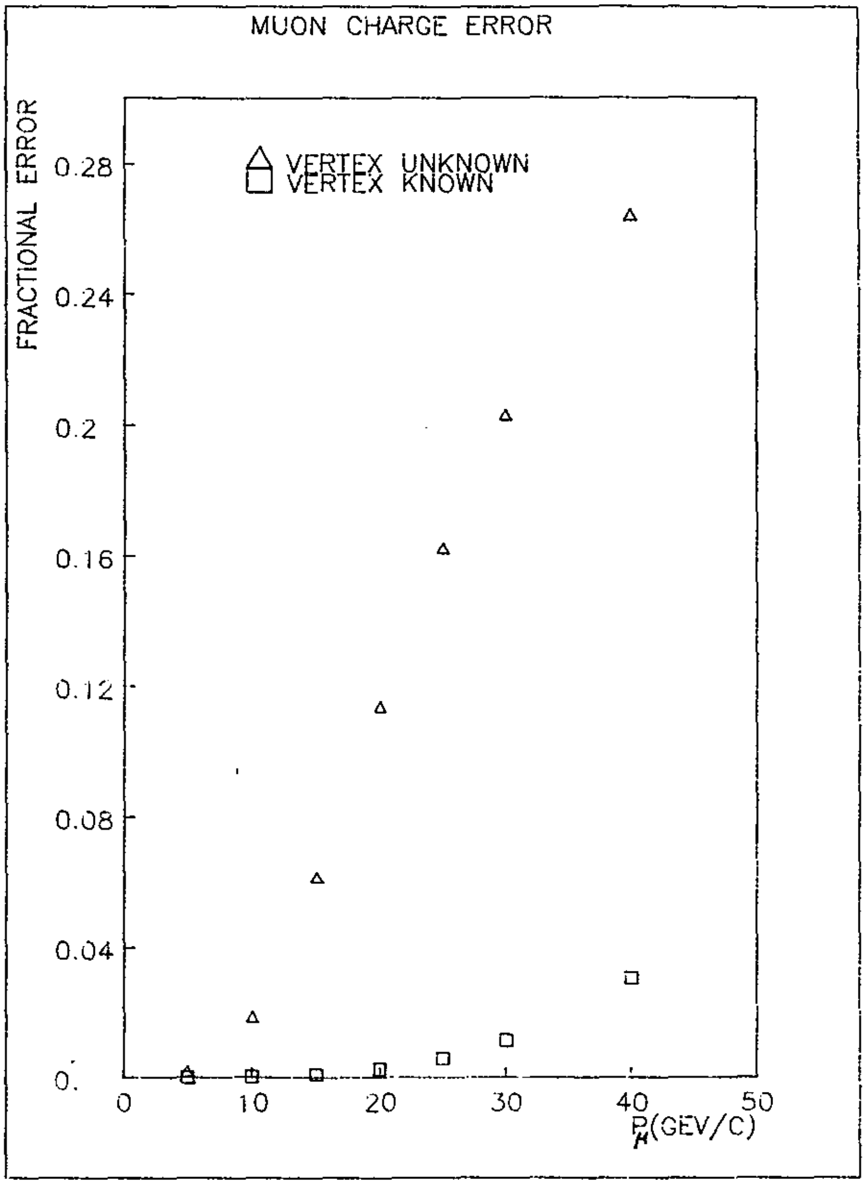

Figure 27. Reconstructed trigger muon momentum and transverse momentum spectra.

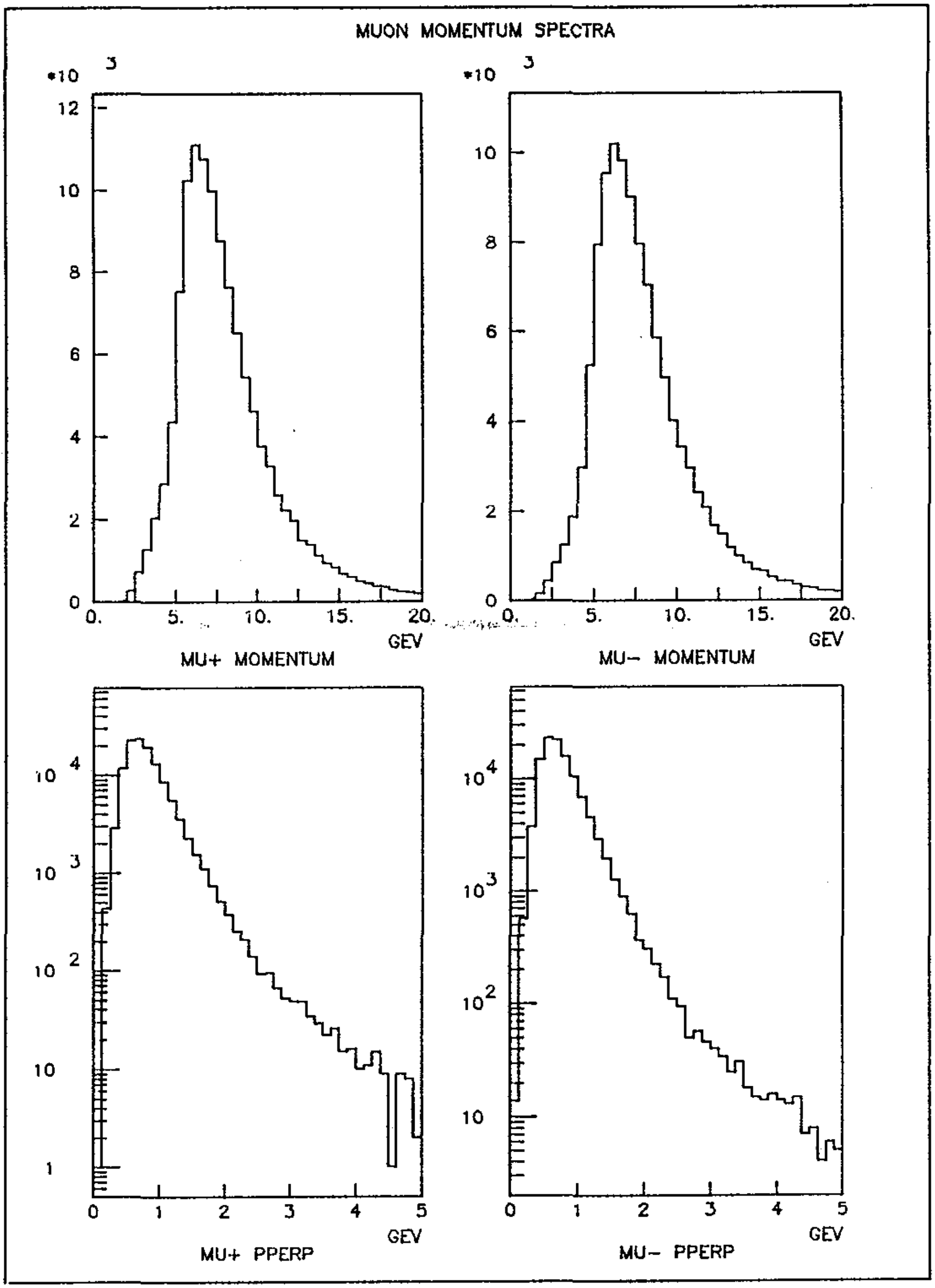

Figure 28. Magnet center residual, $\Delta R = \Delta X^2 + \Delta Y^2$, versus muon momentum. Superimposed are contour lines of the functions, $\Delta R_{cut} = \alpha / P(\mathrm{GeV})$, with the associated reconstruction efficiency for each of the cuts.

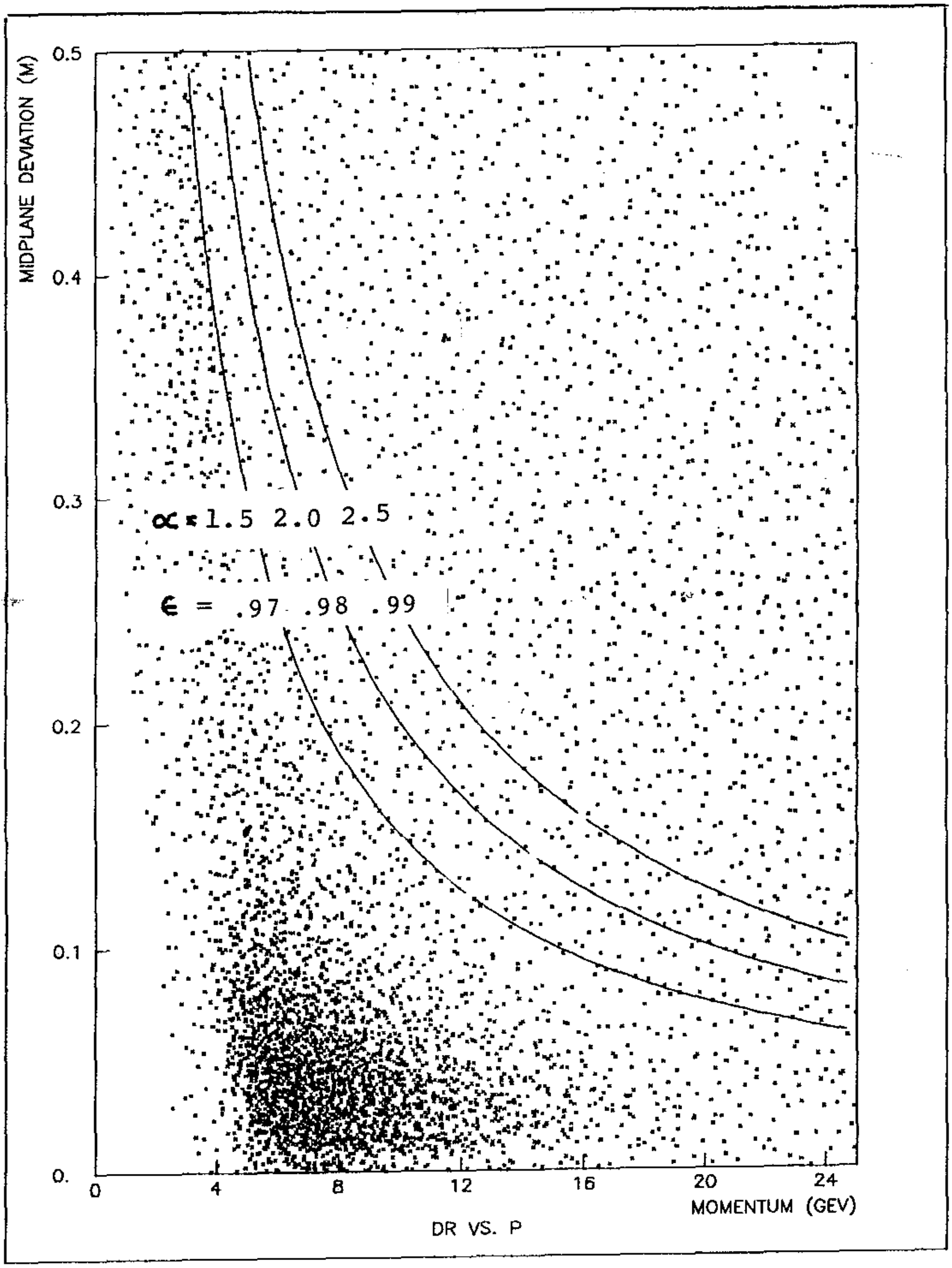

Figure 29. Halo muon cuts.

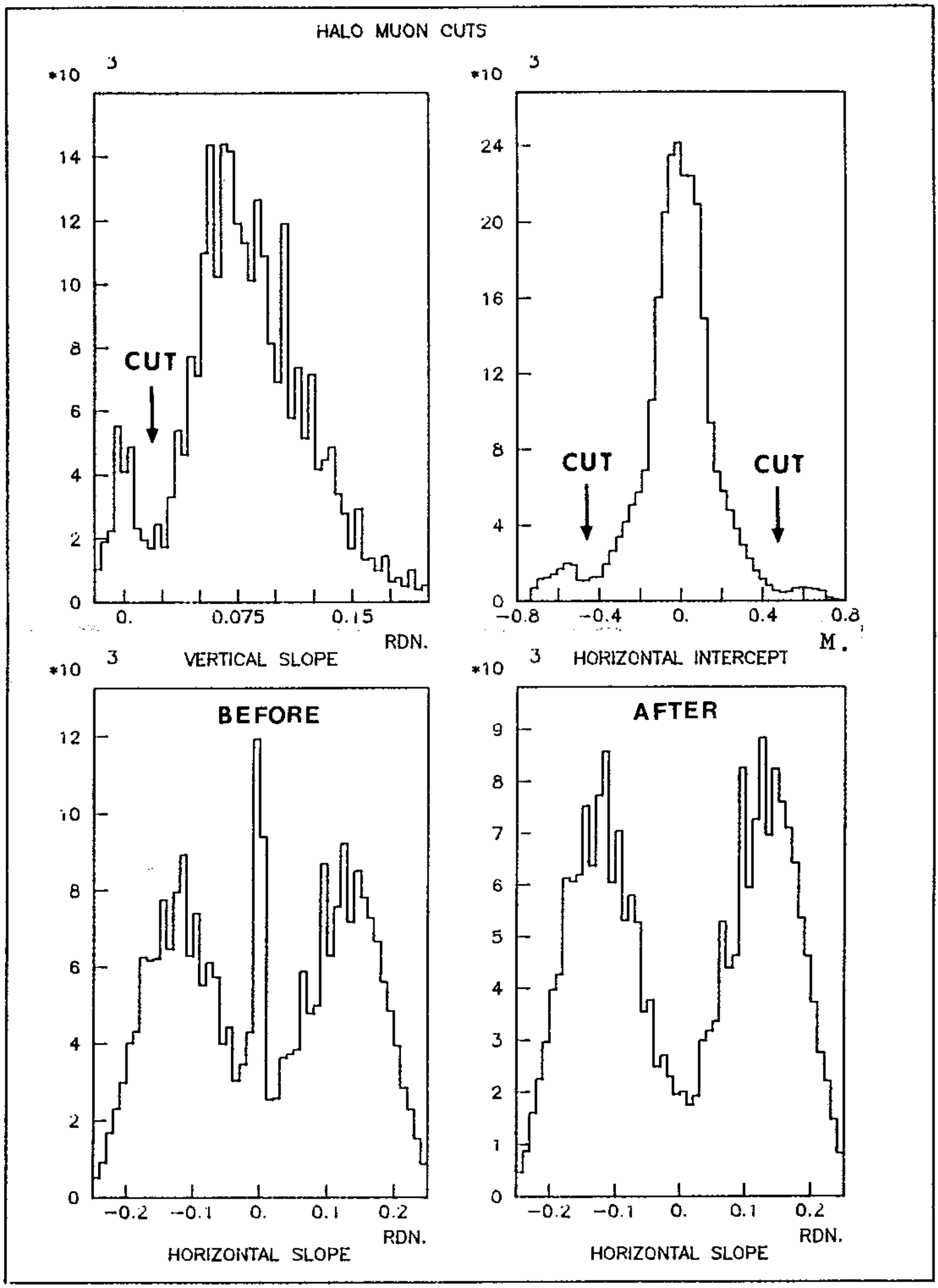

Figure 30. Momentum and transverse momentum spectra for charged tracks reconstructed in the forward spectrometer arm.

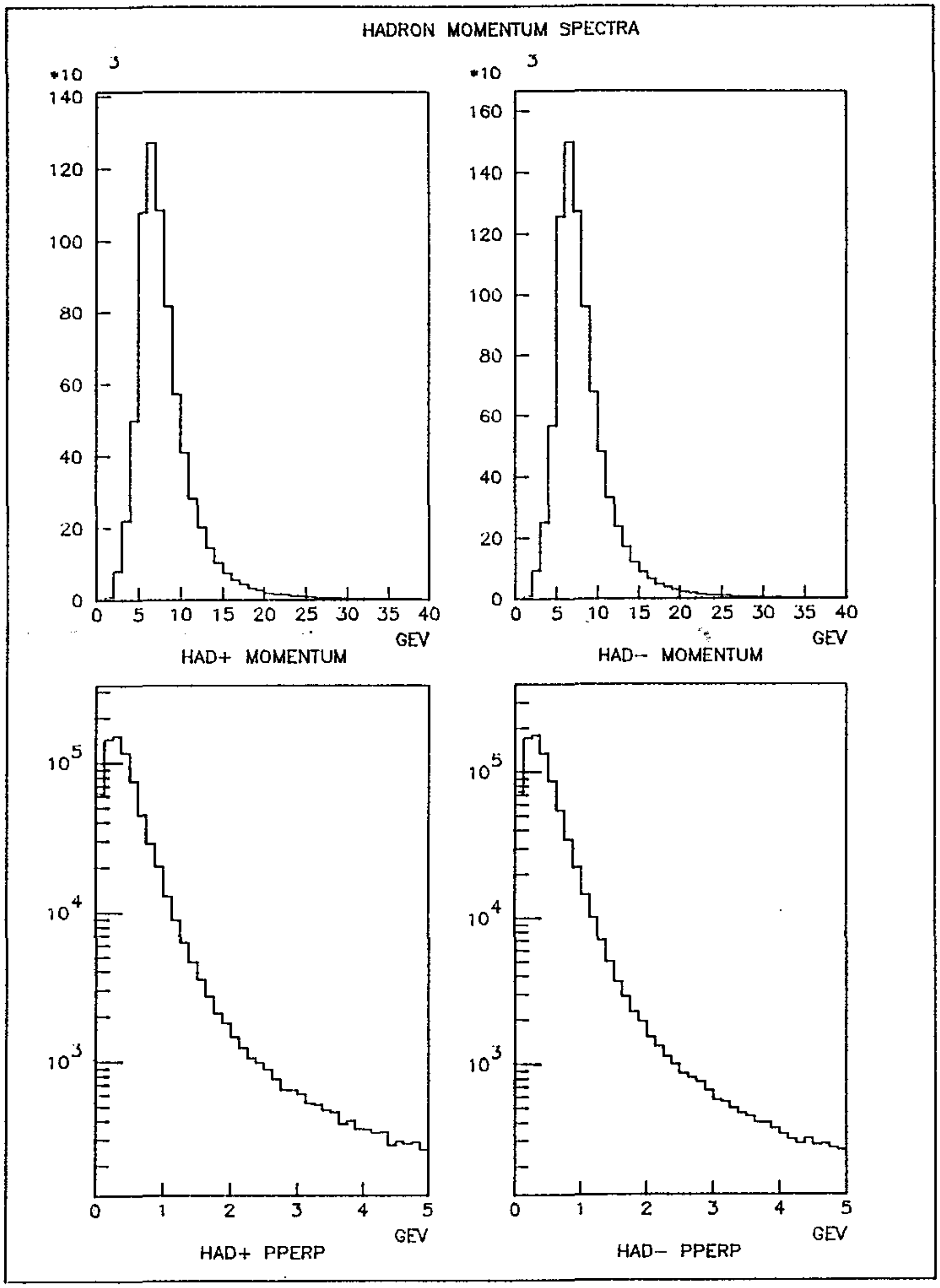

Figure 31. Electromagnetic shower shape profiles (lateral).

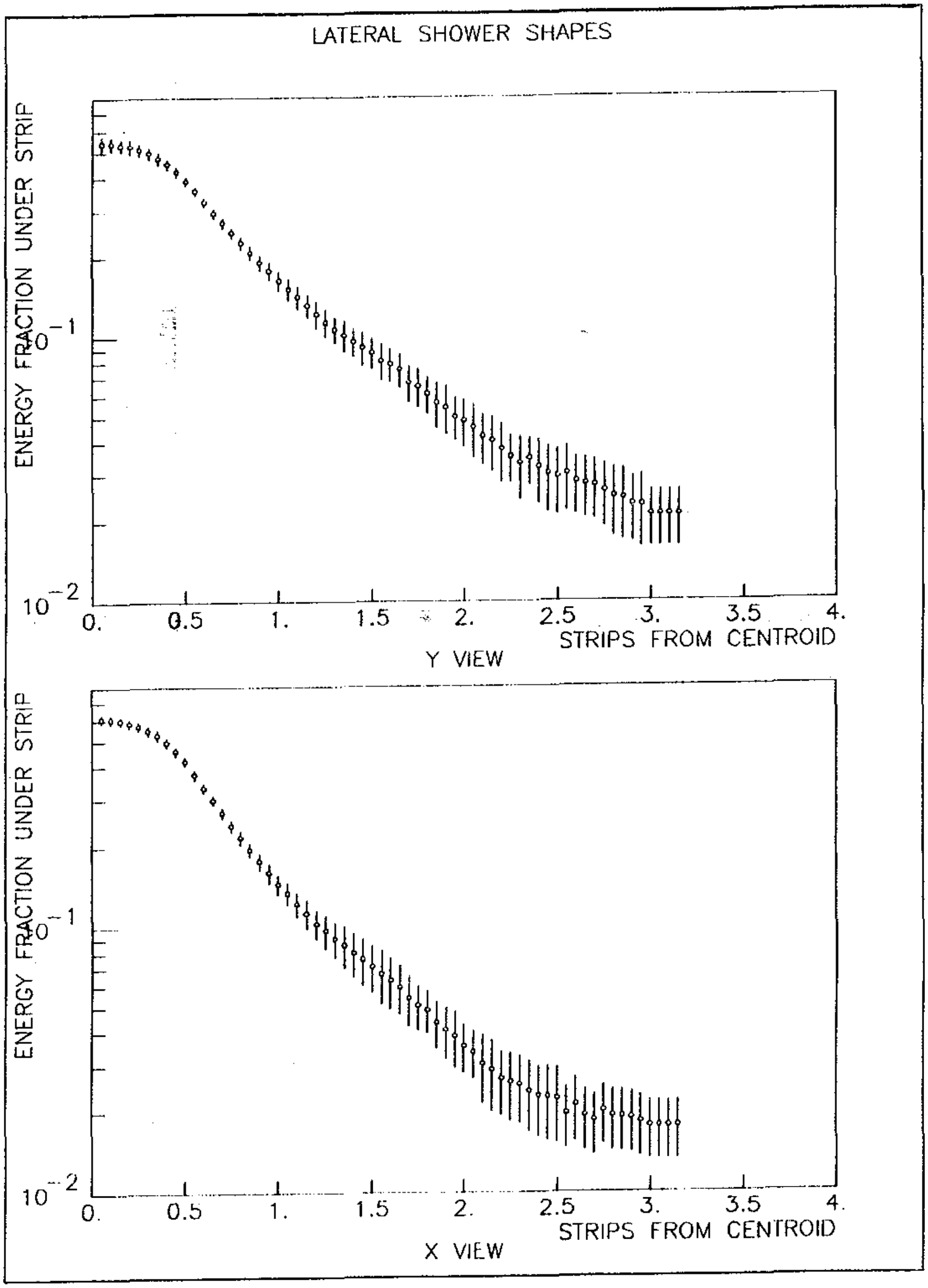

Figure 32. Electromagnetic shower cuts.

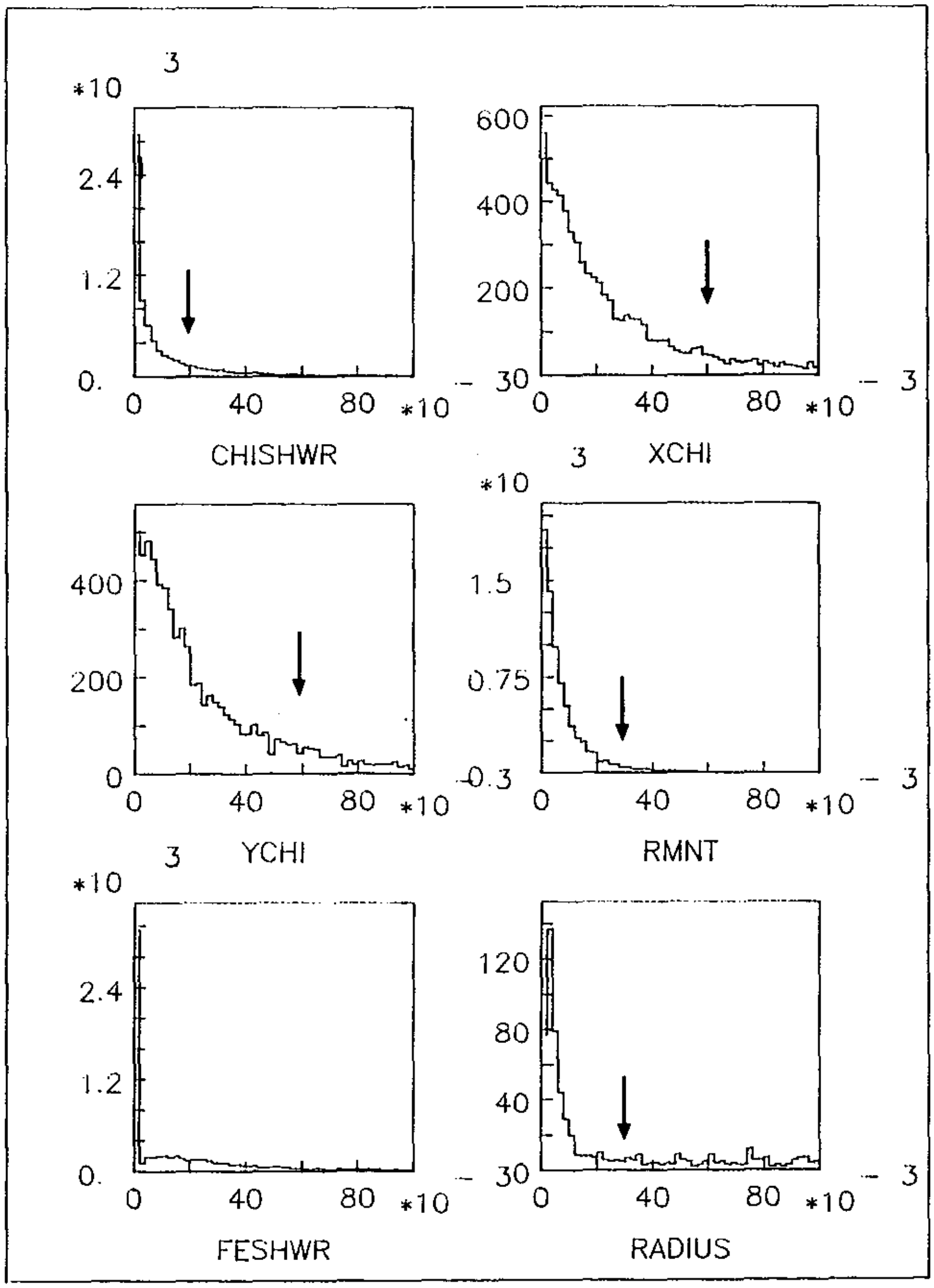

Figure 33. E/P spectra for electrons and positrons identified in the electromagnetic shower detector.

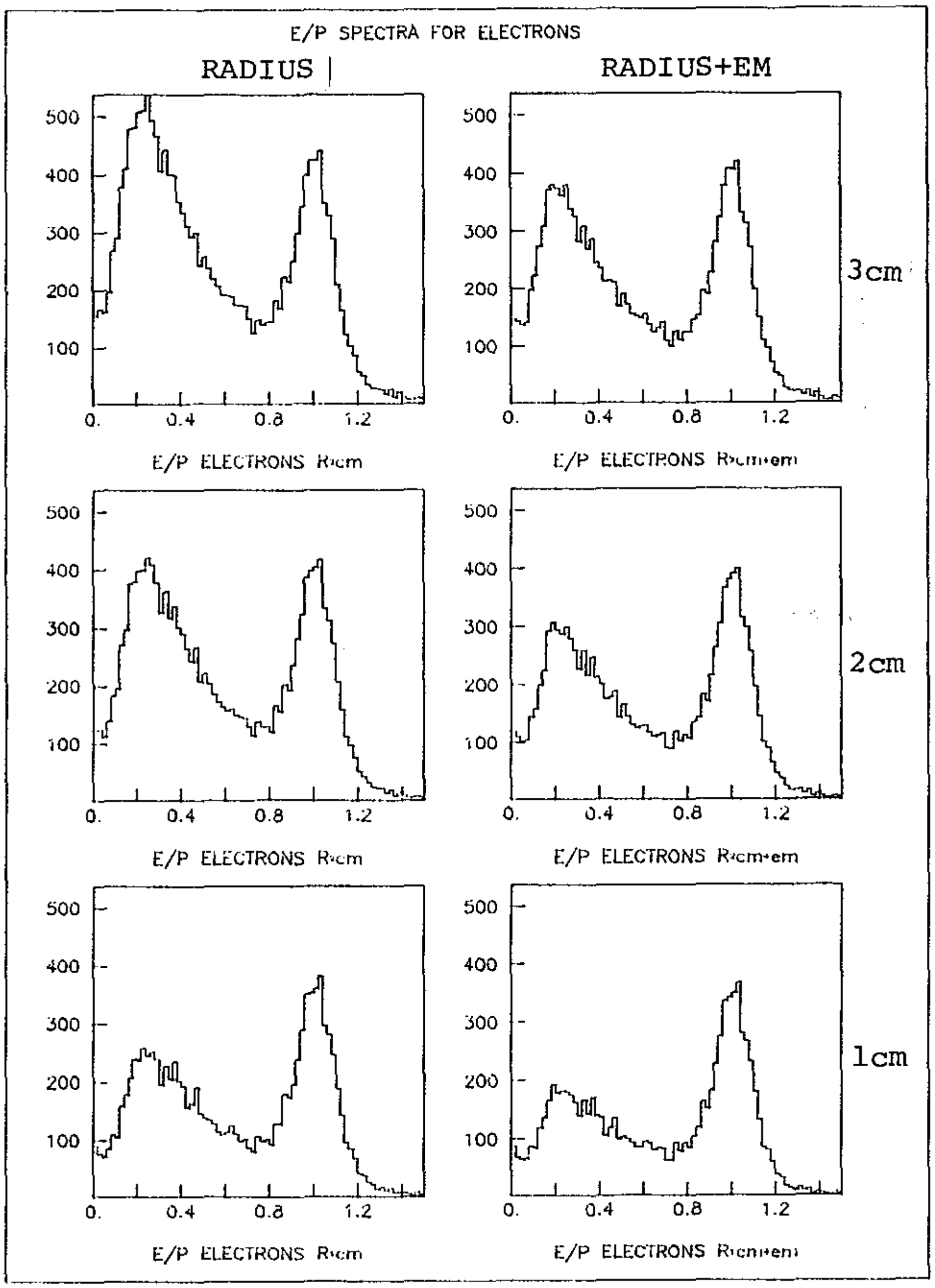

Figure 33. (continued)

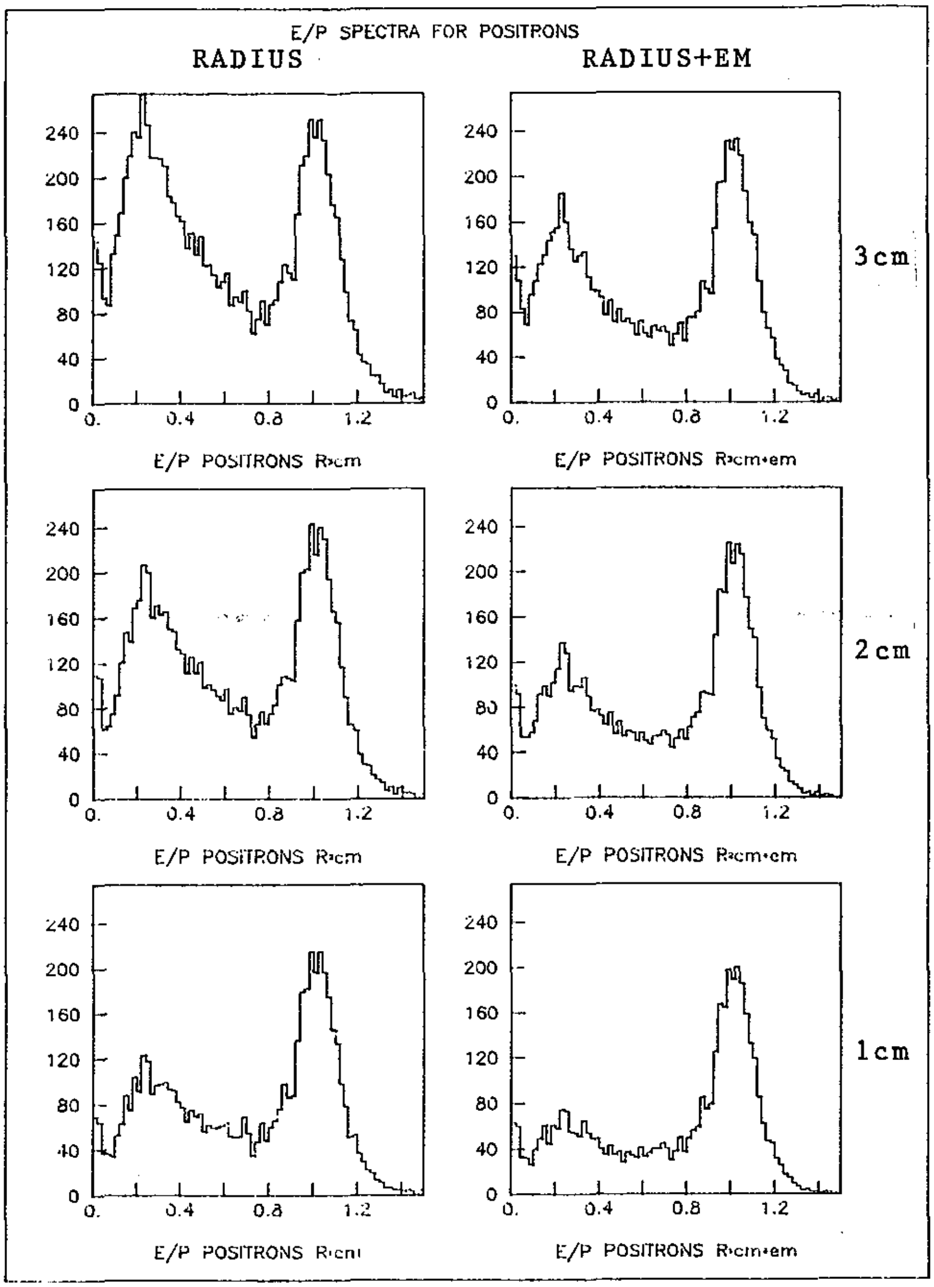

Figure 34. Invariant mass spectrum for electron-positron pairs emphasizing the low mass region. The pairs with masses below 25 MeV are produced by photon conversions and Dalitz decays.

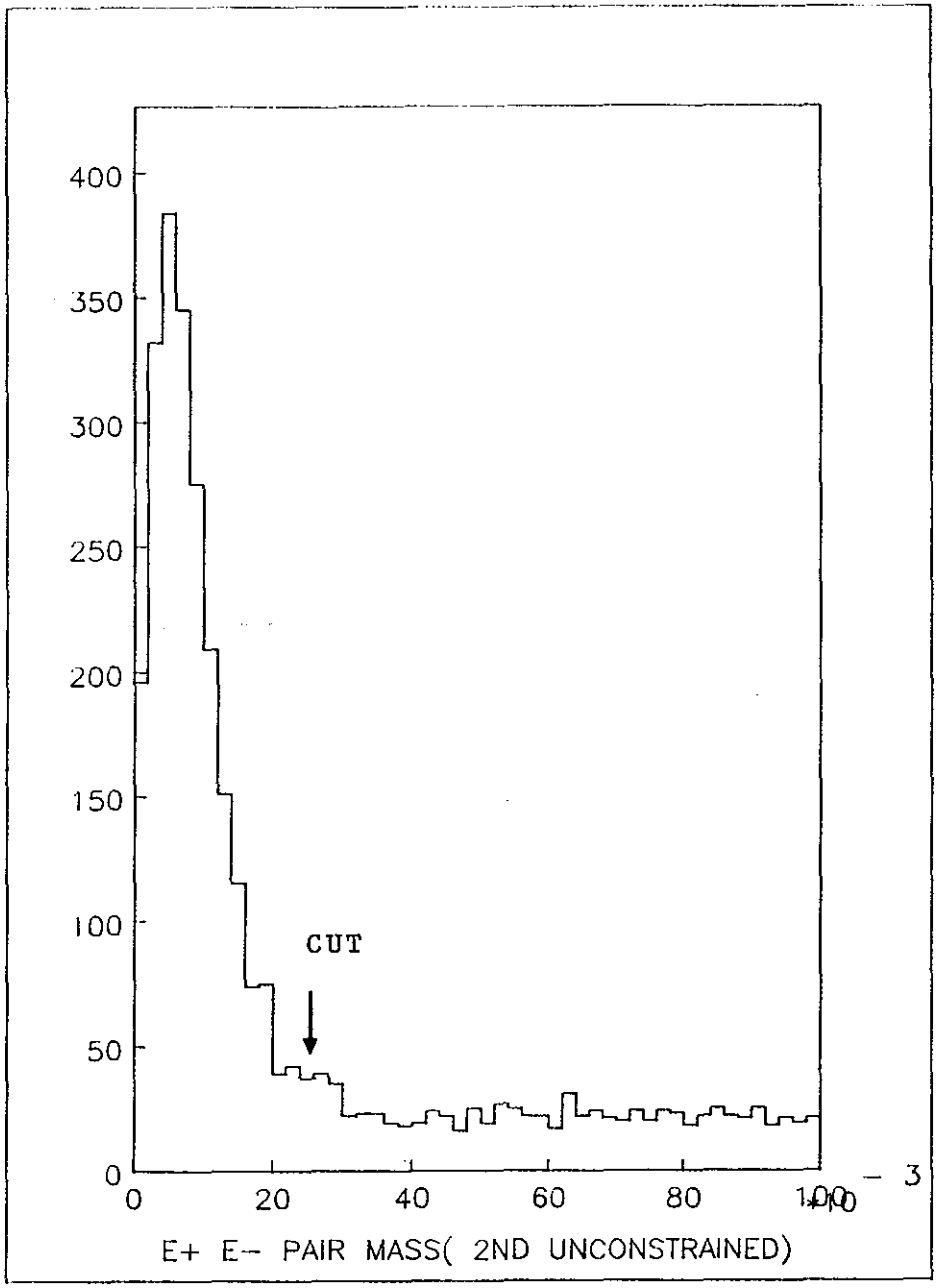

Figure 35. E/P spectra for identified low mass electron-positron pairs.

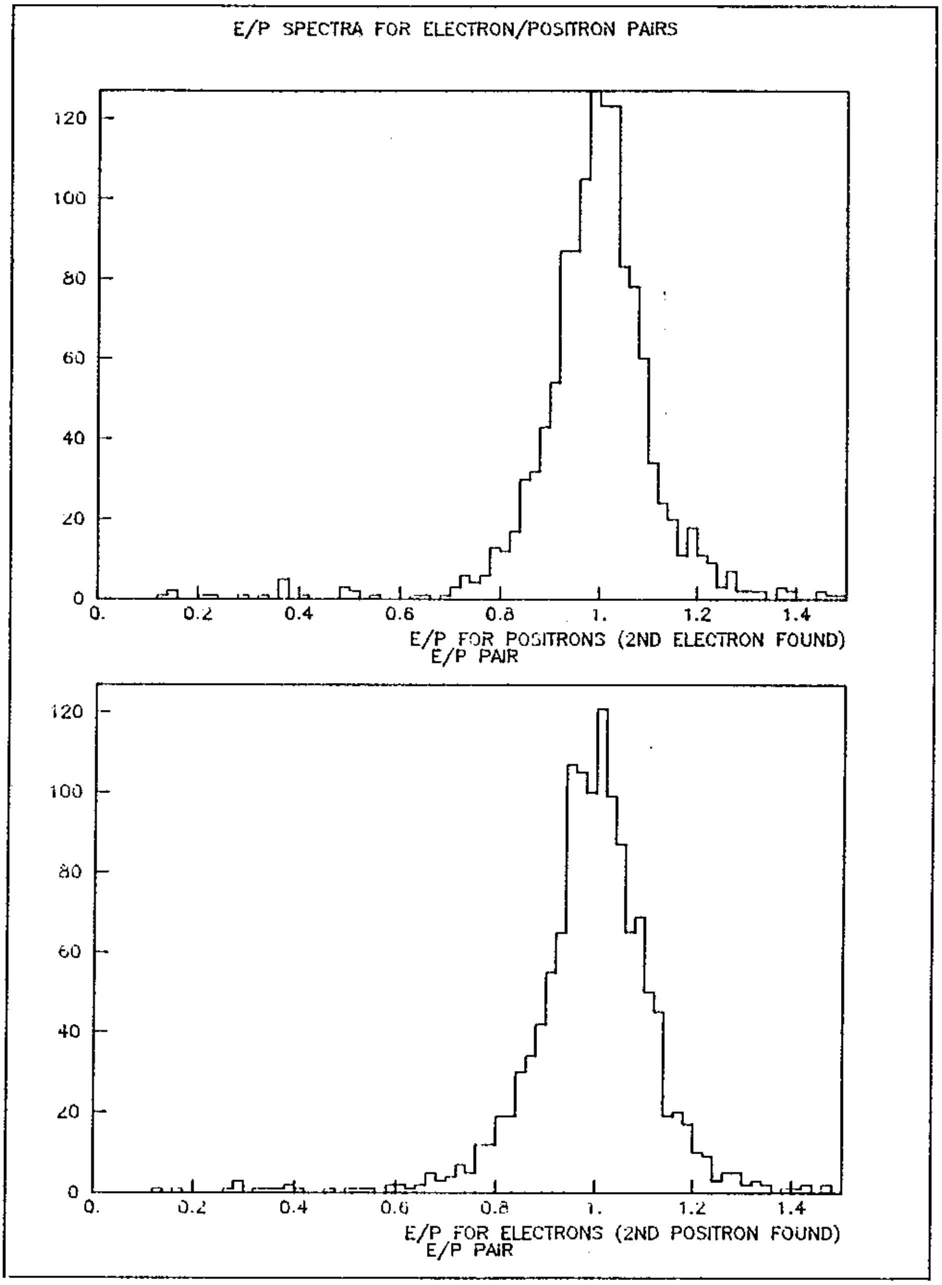

Figure 36. Electron/positron detection efficiency plotted as a function of horizontal position (X) in the electromagnetic shower detector.

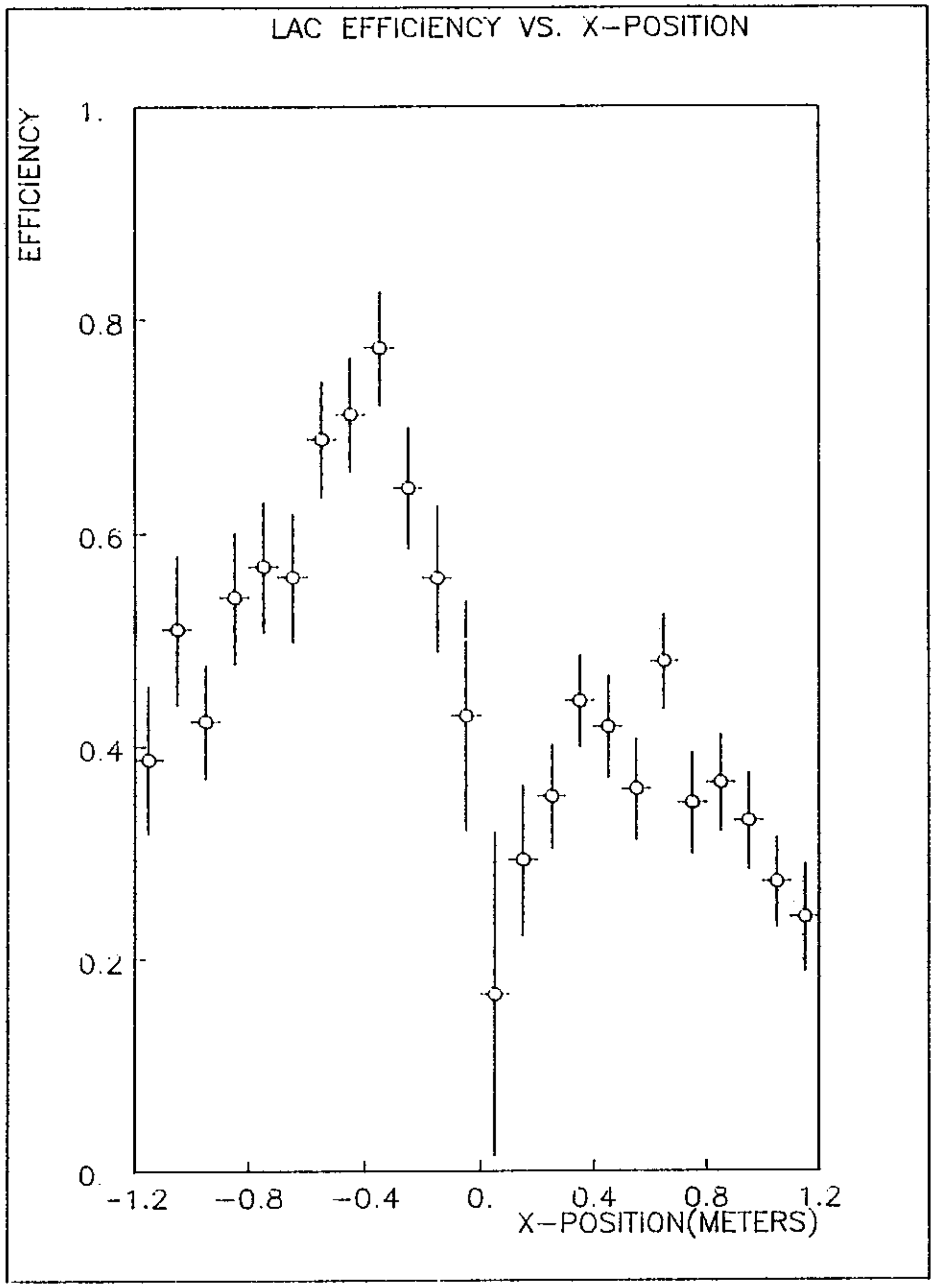

Figure 37. Dimuon invariant mass spectrum.

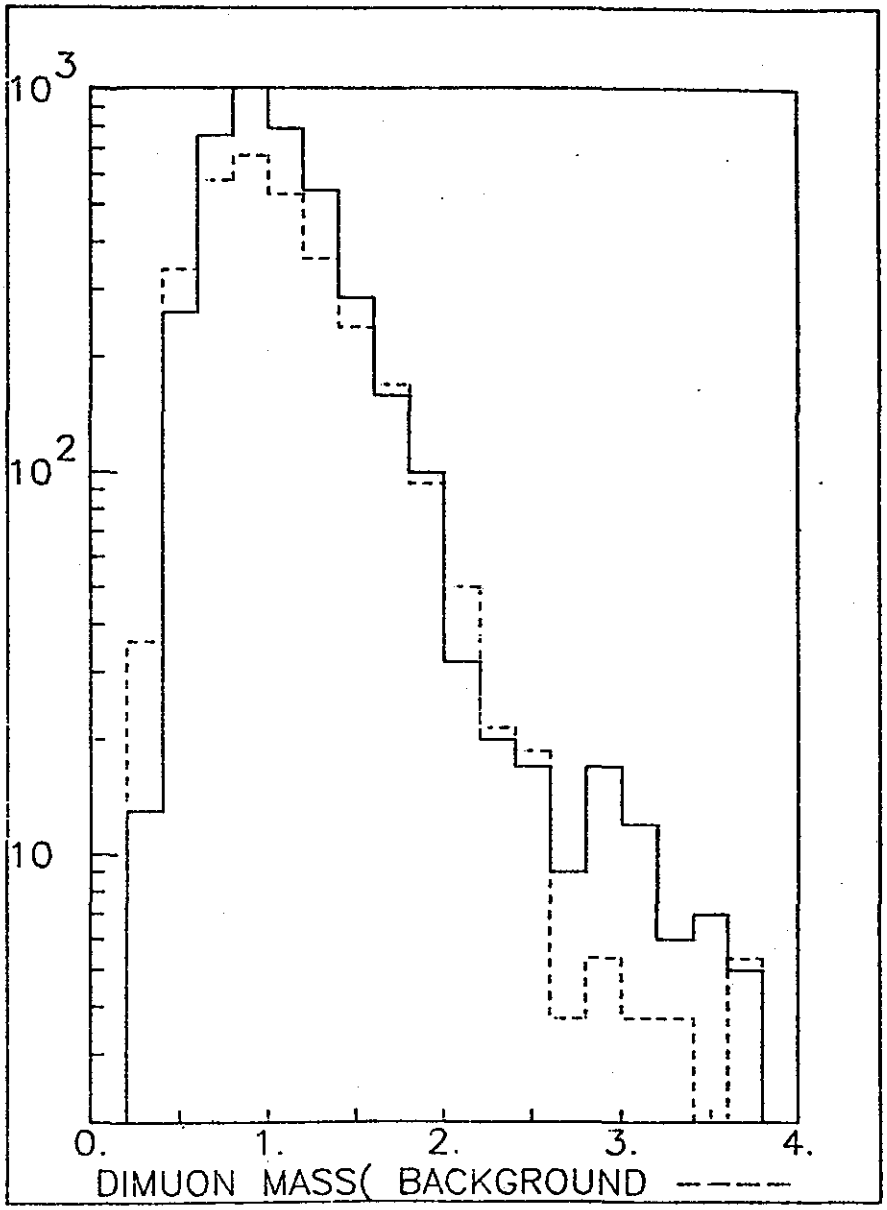

Figure 38. Excess dimuon yield sliced into forward muon momentum bins.

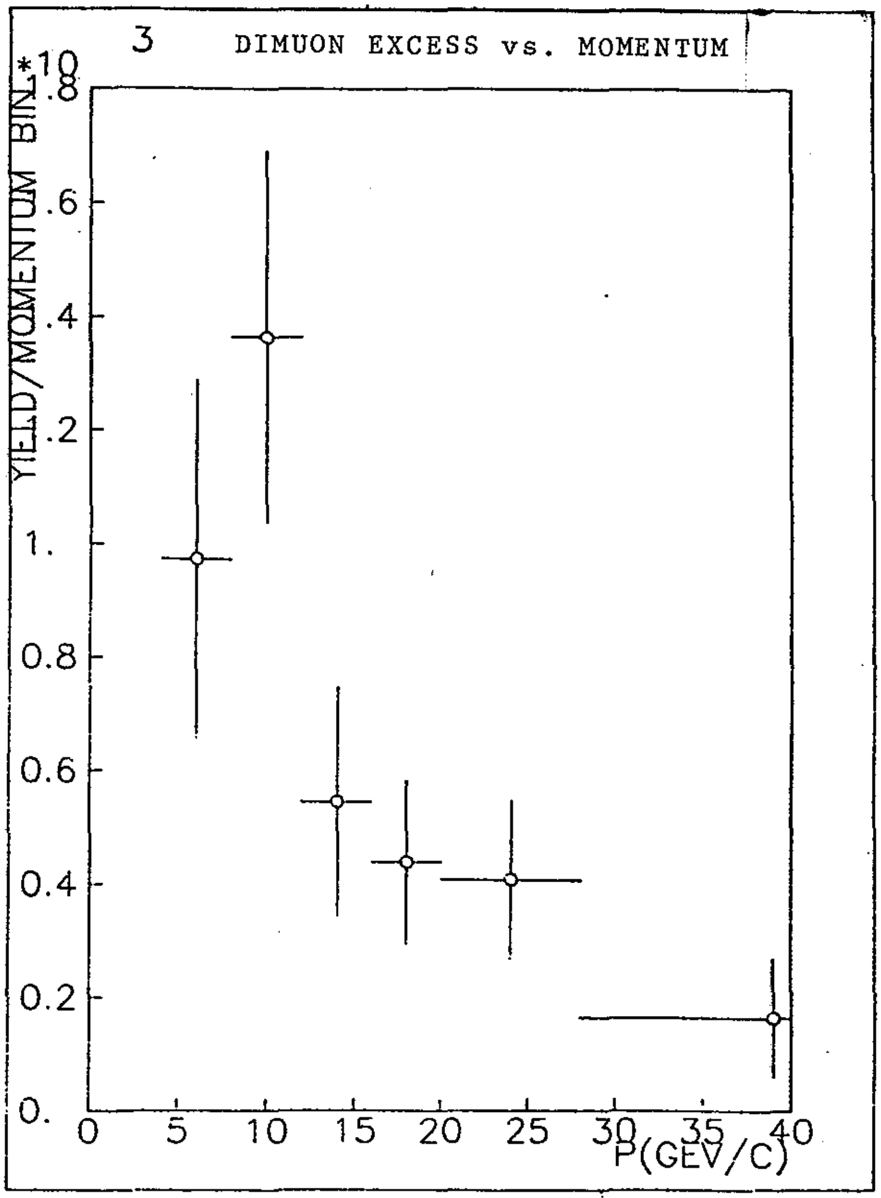

Figure 39. Excess dimuon yield sliced into invariant mass bins of the two muon system.

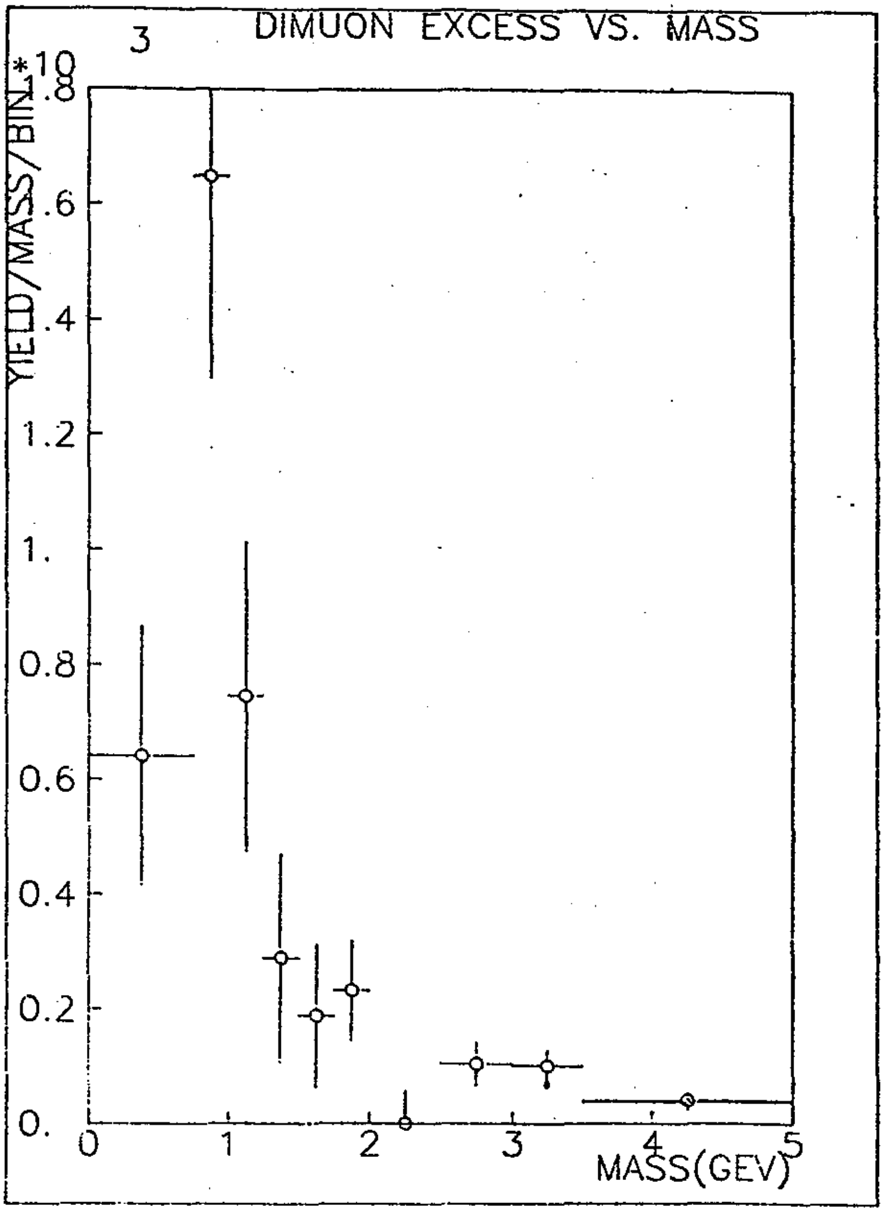

Figure 40. E/P fits to the total electron/positron sample.